

# Numerical simulations of dielectric barrier discharges

Proefschrift voorgelegd tot het behalen van de graad van Doctor in de Wetenschappen aan de Universiteit Antwerpen te verdedigen door

**Tom Martens**

PROMOTOR  
Prof. Dr. Annemie Bogaerts

Faculteit Wetenschappen  
Departement Chemie  
Antwerpen 2010

Universiteit Antwerpen



# Numerical simulations of dielectric barrier discharges

Proefschrift voorgelegd tot het behalen  
van de graad van doctor in de wetenschappen  
aan de Universiteit Antwerpen  
te verdedigen door

Tom Martens

Promotor: Prof. Dr. Annemie Bogaerts

Antwerpen, 2010



# Contents

<b>Acknowledgements</b>	<b>VII</b>
<b>List of Figures</b>	<b>IX</b>
<b>List of Tables</b>	<b>XV</b>
<b>General introduction</b>	<b>XVII</b>
<b>I Background</b>	<b>1</b>
<b>1 Plasmas</b>	<b>3</b>
1.1 Definition . . . . .	3
1.2 The plasma sheath . . . . .	4
1.3 Plasma regimes and structures . . . . .	6
1.3.1 The glow discharge . . . . .	6
At low pressure . . . . .	6
At elevated pressure . . . . .	7
1.3.2 The Townsend discharge . . . . .	8
1.3.3 The subnormal glow discharge . . . . .	9
1.4 The dielectric barrier discharge . . . . .	9
1.4.1 History and background . . . . .	9
1.4.2 Applications . . . . .	13
<b>2 Numerical simulations</b>	<b>15</b>
2.1 Motivation for numerical simulation . . . . .	15
2.2 Simulation methods . . . . .	16
2.2.1 Analytical . . . . .	16
2.2.2 Kinetic . . . . .	16
Solving the Boltzmann equation . . . . .	16
Using a sampling method . . . . .	17
2.2.3 Molecular dynamics . . . . .	17

2.2.4	Fluid	18
2.2.5	Hybrid	18
2.3	Fluid model used in this work	19
2.3.1	Historical background	19
2.3.2	Physical background	19
2.3.3	Boundary conditions	21
2.3.4	Solving the fluid equations	22
 <b>II Analytical plasma source characterization</b>		<b>23</b>
 <b>3 Characterization of a micro-DBD</b>		<b>25</b>
3.1	Introduction	25
3.2	Description of the simulations	26
3.2.1	Chemistry	26
3.2.2	Setup and conditions	29
3.3	Characterization of the discharge in time and space	31
3.3.1	Electrical characteristics	31
3.3.2	Plasma species densities	35
3.3.3	Importance of the chemical production and loss processes	38
3.4	Influence of the pressure on the discharge	43
3.4.1	Influence on the electrical characteristics	43
3.4.2	Influence on the species densities	47
	He <sub>m</sub> <sup>*</sup>	48
	Electrons	50
	He <sub>2</sub> <sup>+</sup>	52
	He <sup>+</sup>	53
	He <sub>2</sub> <sup>*</sup>	54
	He <sup>**</sup>	55
3.4.3	The stability of the discharge	56
3.5	Conclusion	57
 <b>4 Characterization of a DC glow discharge</b>		<b>59</b>
4.1	Introduction	59
4.2	Description of the simulations	62
4.2.1	Models, species and chemical reactions	62
4.2.2	Description of the fluid model	63
4.2.3	Description of the Monte Carlo model	64
4.2.4	Discharge cell geometry and operating conditions	65
4.3	Characterization of the discharge	67
4.3.1	Electric potential and field distributions	67

---

4.3.2	Mean electron energy . . . . .	69
4.3.3	Electron induced collision rates . . . . .	70
4.3.4	Plasma species number densities . . . . .	73
4.3.5	Production and loss processes of the plasma species . . . . .	78
4.4	Conclusion . . . . .	83
<b>III</b>	<b>The atmospheric pressure DBD</b>	<b>85</b>
<b>5</b>	<b>The influence of impurities</b>	<b>87</b>
5.1	Introduction . . . . .	87
5.2	Description of the simulations . . . . .	88
5.2.1	Description of the model . . . . .	88
5.2.2	Description of the chemistry . . . . .	88
5.2.3	Operating conditions and validation . . . . .	90
5.3	Influence of the impurities . . . . .	90
5.3.1	Influence on the composition . . . . .	91
5.3.2	Influence on the reaction rates . . . . .	94
5.3.3	Influence on the electrical profiles . . . . .	95
5.3.4	Influence on the discharge performance . . . . .	97
5.3.5	Pulse shape analysis . . . . .	98
5.3.6	The interplay between chemistry and electrics . . . . .	99
5.4	Conclusion . . . . .	101
<b>6</b>	<b>The regime transitions during operation</b>	<b>103</b>
6.1	Introduction . . . . .	103
6.2	Operating modes in the atmospheric pressure DBD . . . . .	103
6.3	Description of the simulations . . . . .	105
6.3.1	Description of model and chemistry . . . . .	105
6.3.2	Validation of the model . . . . .	106
6.4	The regime transitions during operation . . . . .	107
6.4.1	The charge and electric field distributions . . . . .	107
6.4.2	The influence of the previous discharge pulse . . . . .	110
6.5	Conclusion . . . . .	112
<b>7</b>	<b>The influence of the applied voltage profile</b>	<b>113</b>
7.1	Introduction . . . . .	113
7.2	Description of the simulations . . . . .	113
7.3	Electrical characterization . . . . .	114
7.4	The efficiency of the setups . . . . .	116
7.5	The mechanism of the pulsed DC discharge . . . . .	118

7.6 Conclusion . . . . .	120
<b>Summary</b>	<b>123</b>
<b>Samenvatting</b>	<b>129</b>
<b>Publications related to this work</b>	<b>135</b>
<b>List of conference contributions</b>	<b>137</b>
<b>Bibliography</b>	<b>141</b>

# Acknowledgements

This work would not have been possible without the help and the encouragements of others. First I would like to thank prof. Annemie Bogaerts for giving me the opportunity to do this PhD, for making critical remarks when necessary and for helping making the choices which paths to follow in the research. I would also like to thank you for always making the time to help me in sometimes very busy schedules.

In the beginning of my research prof. Wim Goedheer was so hospitable to help me with my first programming issues by first looking into my problems and later inviting me to come over to Rijnhuizen for two days. This short visit was very instructive to me and I am very grateful for taking the time and making the efforts to help me, thank you.

In the course of tackling the first research problems and applying for scholarships I have had the experienced help of prof. Renaat Gijbels. Thank you for thinking with me to find solutions and for introducing me to prof. José Broekaert to help me with my problems.

For technical help I always could count on Luc Van't Dack to assist me in arranging and solving a whole variety of things for which I am very grateful.

For all help with financial and administrative issues and for the paperwork concerning my PhD I always could count on the help of Nelly Suijkerbuijk, Ingrid Swenters and Tania Beyers. Thank you for all helping hands. It feels great to get your kind assistance.

In Eindhoven there are some people who tremendously helped me with my PhD. They had answers to my questions, we had scientific discussions and we wrote papers together. I really want to thank Jan van Dijk, Joost van der Mullen, Wouter Brok and Diana Mihailova. I really enjoyed our collaborations and I learned a lot from you guys.

My Plasmant colleagues at the University of Antwerp have always been great. Either to have a drink, to do some polls or to go out after work, the company was always great. David and Evi, we started our work in the group at the same moment. This way we had at similar timings a laugh together, shared a tear and had great company during those years. Thanks to all of you.

To all the members of Secret Me. We go way back by now, but our musical ensembles are still great. Thanks for the support and all the fun we have together. Also thanks to all the members of Concordia. We already had some trips together, musical ensembles and even succesful soccer enterprises and I loved them, they were brilliant.

My parents and Wim and Beate, thank you for being there for me, for having an interest in what I am doing and for supporting me when necessary. Also Jos, Nard, Bart and Joke, I'll never forget the support I received from you guys. Thank you, you really have been great.

My final and deepest thanks is to Leen, who always supported me in everything I ventured and who was always there for me. Thank you so much.

# List of Figures

1.1	The top figure illustrates the charge density distributions in case a plasma is present between two surfaces at zero potential [1,2]. Total positive ion density is denoted with $n_i$ and electron density is denoted with $n_e$ . The $\oplus$ denotes the positive charge in the sheath region. In the plasma region the densities of $n_i$ and $n_e$ are about equal. The bottom figure illustrates the resulting potential distribution and the direction of the electric field. The walls are at a lower potential because more electrons than ions reach the walls. . . . .	4
1.2	Illustration of the different regions that can be seen in a glow discharge together with their most important physical parameters [2]. . . . .	5
1.3	Distributions of electron and ion number densities and the typical accompanying electric field. The sketch illustrates that the ion density is usually much higher than the electron density and that the charge number densities are too low to disturb the electric field. . . . .	8
1.4	Typical arrangements for electrodes and dielectrics in DBDs [3]. . . . .	10
1.5	Drawings from Werner von Siemens of the cross section and the side view of his dielectric barrier ozonizer [4]. . . . .	10
1.6	The manifestation of filaments in an atmospheric pressure dielectric barrier discharge [5]. . . . .	11
3.1	Cross sections of the different electron-induced processes as a function of electron energy. The labels correspond to the numbers in Table 3.1. The label (a) denotes the electron elastic cross section for He atoms, which only changes the electron energy in the model, not the species densities. Label (1) indicates the electron-induced excitation to the He metastable levels $\text{He}_m^*$ , (2) the electron induced excitation to the higher excited He levels $\text{He}^{**}$ , (3) the electron-induced ionization from the He ground state and (4) the electron-induced ionization from the He metastable level. These cross-sections were adopted from the Siglo Database [6], except for the cross section of reaction 4 which originates from the work of Janev and coworkers [7]. . . . .	28
3.2	Schematic diagram of the setup. . . . .	30

---

3.3	Potential applied to the electrodes ( $V_{appl}$ , black dashed line, left axis) and calculated electric current density (red line, right axis), as a function of time at 80 mbar, 20 kHz, and 750 $V_{pp}$ . The calculated voltage over the discharge gap (so-called gap voltage, $V_{gap}$ ) is also plotted (black solid line, left axis), because this determines the plasma characteristics. (a) shows the temporal periodicity over a long time, whereas (b) is a magnification of one period, consisting of a positive and a negative voltage polarity. In (b) the solid circles on the gap voltage profile denote specific moments in time, related to figure 3.4. . . . . .	32
3.4	Calculated voltage drop or potential distribution between the electrodes at several moments in time (see legend), when the powered electrode is negative (a, solid lines) and positive (b, dashed lines) under the same discharge conditions as in figure 3.3. The arrows represent the time evolution of the potential distribution. The positions of grounded electrode (GE) and powered electrode (PE) are also indicated. Note that not only the potential distribution inside the plasma but also the potential drop across the dielectrics is depicted. . . . . .	33
3.5	Calculated electron number density profiles inside the plasma at approximately the same moments in time as in figure 3.4 and under the same discharge conditions. Note the logarithmic scale of the y-axis, which was necessary to visualize all curves on one plot. . . . . .	35
3.6	Calculated spatially averaged number densities of the different plasma species as a function of time, under the same conditions as in figure 3.3. Note that the $\text{He}_m^*$ density was divided by 10, to enable its inclusion in the same figure as the other curves. . . . . .	36
3.7	Calculated number density profiles of the different plasma species at the peak of their temporal evolution (i.e., at 349 $\mu\text{s}$ ) for the same discharge conditions as in figure 3.3. The charged particles are represented with solid lines whereas the dashed curves stand for the neutral species. Note that the $\text{He}_m^*$ density was divided by 10, to enable its inclusion in the same figure as the other curves. . . . . .	38
3.8	Voltage applied to the electrodes (top frame, dotted line) and potential difference between the surfaces of the dielectrics, also called gap voltage (top frame, solid line). The current density peak shown in the bottom frame, always occurs right after the maximum in gap voltage. This profile is taken for a pressure of 87 mbar and the current density peaks have an amplitude of 0.28 A/cm <sup>2</sup> . . . . . .	43
3.9	Inuence of the pressure on the discharge current density. In the top frame the absolute values of the positive and negative current peaks ( $J_+$ and $J_-$ , respectively) are plotted at different pressures. In the bottom frame the absolute value of the ratio of the positive to the negative current peak is shown. There is clearly a higher current density in the region from 50 to 140 mbar, where also the positive current peak seems to be significantly higher than the negative one. . . . . .	45

3.10	Calculated spatial distributions of the potential, the electron density and the sum of positive ion densities for two distinct cases of 120 mbar and 500 mbar. The grounded electrode is at the left hand side and the powered electrode at the right, which is currently at a positive potential. From 0 to 20 $\mu\text{m}$ and from 980 to 1000 $\mu\text{m}$ there is no discharge gas, since the space is filled with dielectric. Hence, the species densities in those regions are zero. The vertical dotted lines denote the border between plasma and dielectrics. . . . .	46
3.11	Calculated spatially averaged neutral species densities at the maximum positive current for pressures ranging from 25 to 1100 mbar. . . . .	47
3.12	Calculated spatially averaged charged particle densities at the maximum positive current for different pressures. . . . .	48
3.13	Calculated relative contributions of the chemical reactions leading to the destruction of $\text{He}_m^*$ at the maximum positive current, as a function of pressure. The numbers between brackets correspond to the numbers in the first column of Table 3.1 . . . . .	49
3.14	Calculated spatially averaged reaction rates of the seven most important reactions in the plasma at the maximum positive current for different pressures. . . . .	50
3.15	Calculated relative contributions of the chemical reactions leading to the production and destruction of the electrons at the maximum current for different pressures. . . . .	51
3.16	Calculated relative contributions of the different chemical reactions leading to the production and destruction of the $\text{He}_2^+$ ions at the maximum positive current for different pressures. . . . .	52
3.17	Calculated relative contributions of the different chemical reactions leading to the production (top frame) and destruction (bottom frame) of $\text{He}^+$ ions. . . . .	54
3.18	Maximum values of the calculated spatially averaged densities of $\text{He}_2^*$ and the reaction rates of the most important production and destruction reactions. . . . .	55
3.19	Calculated average electron energy at maximum positive current for the different pressures under study. . . . .	57
4.1	Schematic diagram of the APGD source under study (not completely to scale) (a) The shaded box gives the simulated area. Because of the cylindrical symmetry, the calculation results will be presented in only one-half of this box, as indicated in part b. . . . .	66
4.2	Calculated 2D electric potential distribution (a) and axial (b) and radial (c) electric field distributions in the cell geometry illustrated in figure 4.1b. The cathode is found at the left ( $Z=0$ ) whereas the anode cone is at the right. The symmetry axis is at $R=0$ . . . . .	68
4.3	Calculated 2D profile of the mean electron energy. . . . .	70

4.4	Calculated 2D profiles of the electron induced reaction rates: (a) ionization of He ground state atoms, (b) excitation to the $\text{He}_m^*$ metastable atoms, (c) ionization from the $\text{He}_m^*$ metastable atoms and (d) rotational-vibrational excitation of the $\text{N}_2$ molecules. In part b, different spatial zones of the GD, as obtained from the excitation (or emission) intensities are also schematically indicated. . . . .	71
4.5	Calculated 2D electron number density profile. . . . .	73
4.6	Calculated 2D number density profiles of the $\text{He}^+$ (a), $\text{He}_2^+$ (b), $\text{N}_2^+$ (c) and $\text{N}_4^+$ (d) ions. . . . .	75
4.7	Calculated 1D profiles of the total positive ion number density (i.e. sum of $\text{He}^+$ , $\text{He}_2^+$ , $\text{N}_2^+$ , and $\text{N}_4^+$ ions; solid line) and electron density (dashed line) taken at the discharge axis. . . . .	77
4.8	Calculated 2D number density profiles of the $\text{He}_m^*$ metastable atoms (a) and the $\text{He}_2^*$ excimers (b). . . . .	78
4.9	Calculated 2D reaction rate profiles of the dominant production mechanisms of (a) the $\text{He}_2^+$ ions (i.e. Hornbeck-Molnar associative ionization), (b) the $\text{N}_2^+$ ions and $\text{He}_2^*$ excimers (i.e. charge transfer between $\text{He}_2^+$ and $\text{N}_2$ ) and (c) the $\text{N}_4^+$ ions (i.e. conversion from $\text{N}_2^+$ ions). The dominant production mechanisms for the $\text{He}^+$ ions and $\text{He}_m^*$ metastable atoms are electron induced ionization and excitation respectively, for which the rates were presented in figure 4.4a and b. . . . .	81
5.1	Top frame: Experimental results for the discharge current density, gap voltage and applied voltage as a function of time obtained by Mangolini and coworkers [8]. Bottom frame: Our calculated results using the same conditions (see text). . . . .	91
5.2	Calculated time and spatially averaged densities of the important charged particles in an atmospheric DBD in helium with different levels of $\text{N}_2$ impurity. The vertical dotted line indicates the boundary between the $\text{He}_2^+$ governed part and the $\text{N}_2^+$ governed part. The upper dotted curve indicates the sum of the positive ion densities. . . . .	92
5.3	Calculated time and spatially averaged densities of the important charged particles in an atmospheric pressure helium DBD with nitrogen impurity levels ranging from 0.5 ppm to 0.5% . Region <b>I</b> denotes the $\text{He}_2^+$ governed part, region <b>II</b> the $\text{N}_2^+$ governed part, region <b>III</b> the $\text{N}_4^+$ governed part with significant $\text{N}_2^+$ contribution and region <b>IV</b> is completely governed by $\text{N}_4^+$ ions. . . . .	93
5.4	Calculated sum of total production and destruction rates for $\text{He}_2^+$ , $\text{N}_2^+$ and $\text{N}_4^+$ . . . . .	94
5.5	Calculated results for the discharge current density and gap voltage as a function of time, shown together with the applied voltage. Each frame corresponds with a different level of impurity. . . . .	96
5.6	Normalized calculated electron density, dissipated power and electron production efficiency as a function of $\text{N}_2$ content. . . . .	97

5.7	Top frame: Charge density transferred during the positive part of the current pulse and the maximum value of the discharge current as a function of the N <sub>2</sub> content. Bottom frame: Equivalent peak width determined by dividing the integrated positive part of the current pulse by the maximum value of the discharge current. . . . .	99
6.1	Calculated results for the discharge current and gap voltage as a function of time, shown together with the applied voltage. . . . .	106
6.2	Calculated electron density distributions at six different moments in time relative to the maximum of discharge current. The subfigure indicates the exact positions of these six moments in time on the discharge current peak. . . . .	107
6.3	Calculated net charge density distributions at six different moments in time relative to the maximum of discharge current. . . . .	109
6.4	Calculated axial component of the electric field at six different moments in time relative to the maximum of discharge current. . . . .	109
6.5	Calculated contour plot of the time evolution of the electron density distribution. At 0 and 14.26 $\mu$ s respectively the first and second maximum of discharge current occur. . . . .	111
6.6	Calculated positions (red) and values (black) of the maximum electron density from the first pulse (full lines) and the second pulse (dashed lines) illustrated in figure 6.5. At 0 and 14.26 $\mu$ s respectively the first and second maximum of discharge current occur. . . . .	111
7.1	Calculated current density and gap voltage as well as applied voltage during one period of applied voltage. Setup (1) uses a rf voltage, (2) a 10 kHz sinusoidal profile, (3) a rectangular voltage and (4) a pulsed dc profile. . . . .	115
7.2	Normalized electron density, plasma power and electron production efficiency for the rf voltage (1), the 10 kHz sinusoidal voltage (2), rectangular (3) and pulsed dc voltage (4). . . . .	116
7.3	Spatial profiles of the calculated electric potential from the powered electrode on the left to the grounded electrode on the right. The vertical lines illustrate the surfaces of the dielectrics on the electrodes. The profiles are shown from 50 ns before the maximum gap voltage of 3.4 kV is reached (0), until 80 ns after the maximum gap voltage. . . . .	119
7.4	Similar profiles as in figure 7.3. The profiles are shown from 50 ns before the minimum gap voltage of -3.4 kV is reached (0), until 80 ns after the minimum gap voltage. Note that the green dashed line in the upper frame (-50 ns) has exactly the same shape as the green dashed line in the bottom frame of fig 3 (80 ns), demonstrating that the potential distribution does not change for about 50 microseconds between the times of maximum and minimum gap voltage. . . . .	120



# List of Tables

3.1	Complete set of reactions used in the model with their reaction rate coefficients.	27
3.2	Calculated relative contributions of the different production and loss processes for each of the different plasma species, both at the peak (i.e., 349 $\mu\text{s}$ ) and during the plateau time (i.e., 360 $\mu\text{s}$ ) at the same discharge conditions as indicated in figure 3.3. The numbers between brackets in the first column correspond to the numbers of the reactions listed in Table 3.1.	41
4.1	Complete set of reactions used in the model with their reaction rate coefficients. The electron impact reactions are described with energy-dependent cross sections. The last column gives the references where the rate coefficients and cross sections are adopted from. In the MC model, the electron induced reactions (reactions 1,2 and 3) are included as well as electron induced excitation of the $\text{N}_2$ impurities to the lowest rotational and vibrational levels.	63
4.2	Calculated relative contributions (in %) of the production and loss processes for the various plasma species, taken into account in the model. The numbers between parentheses correspond to the reactions given in Table 4.1.	80
5.1	Reactions included in the model with their reaction rate coefficients. The first three reaction rate coefficients are calculated using Bolsig. In reaction 16, M denotes a heavy collision partner and the destruction frequency is taken from Golubovskii and coworkers [9].	89



# General introduction

The dielectric barrier discharge (DBD) is a setup which is already more than 150 years old. However, the number of new applications is increasing like never before. The reason for this lies in the growing realization that it is a remarkably good method to generate atmospheric pressure plasmas with highly energetic electrons in a background gas which is still near room temperature. These new applications, however, need a much higher degree of control over the discharge and often work in very small dimensions. The separation between the electrodes in a DBD is mostly only a few millimeters. Such dimensions become too small for probe techniques to accurately measure electron energies and electric potentials. In such case numerical modeling of the plasma is indispensable to obtain detailed information. Moreover, using simulations specific parameters such as applied voltage, reflection coefficients or small changes in gas purity can be studied independently from the rest, which is experimentally almost never possible.

The present work can be divided in three major parts. **Part I** provides the background information. **Part II** treats analyses of two experimental atmospheric pressure plasma sources and **Part III** provides for in-depth research results on the classical atmospheric pressure dielectric barrier discharge.

The research in this thesis focuses on numerical descriptions of gas discharges in helium. Therefore, in **Part I, Chapter 1** the plasmas and their most important properties that are encountered in this work are clarified, as well as the historical background of the dielectric barrier discharge. In **Chapter 2** an overview is first given of the advantages and disadvantages of commonly used simulation techniques as an introduction to the second part, which is a description of the model that is used in this work.

**Part II** focuses on the development of new plasma sources used to dissociate molecules in order to analyze them using atomic spectrometry. Two experimental setups have been investigated in detail using numerical simulations. For both setups detailed spatial profiles of the potential distributions and the species densities are presented, as well as an analysis of the most important production and destruction processes of the important species. In **Chapter 3** a dielectric barrier discharge is investigated which is being miniaturized in order to develop in the future a complete

miniature analytical tool or a so-called “lab on a chip”. **Chapter 4** presents the investigation of a new atmospheric pressure discharge, which has the remarkable feature that although the discharge is operated at atmospheric pressure, a stable glow discharge is obtained using a separation length of 1 cm between a small rod and a large cone as the electrodes.

**Part III** treats the research results of very specific analyses of the atmospheric pressure dielectric barrier discharge using flat electrodes. These are mainly focused on a better understanding of the discharge in order to improve its use and operation. In **Chapter 6** numerical simulations of high time and space resolution are performed in order to obtain information on the regime transformations during the operation of the so-called dielectric barrier ‘glow’ discharge. Usually these plasma regimes are determined using photographs, but since the small dimensions complicate photography, crucial information such as the spatial charge distributions are not experimentally accessible. Therefore, simulations are carried out to provide the background information to explain the experimentally observed phenomena. **Chapter 5** treats the influence of impurities in the feeding gas on the composition and the electrical performance of the discharge. Explanations for the observed phenomena are found by analyzing the influence of  $N_2$  on the reaction chemistry, which has not only a direct influence on the composition, but even on the time behavior of the discharge. Finally, in **Chapter 7**, a comparison is made of the generation of the dielectric barrier discharge using different types of voltage profiles. This voltage profile shape is very important for the power consumption, because there is a certain interaction with the accumulated charges on the dielectric barriers. It is first investigated which profile forms the most efficient combination with the dielectric charging effect and then for this setup the synergetic effect is studied in great detail.

**Part I**  
**Background**



# Chapter 1

## Plasmas

### 1.1 Definition

A plasma or gas discharge mostly resembles an ionized gas. It is one of the four states of matter next to solid, liquid and gas. It is generated by applying a sufficiently high electric field to a gas, which partially breaks it down, turning some atoms or molecules into positive ions and generating free electrons. These free charges make the plasma electrically conductive, internally interactive and strongly responsive to electromagnetic fields and surfaces. These unique properties make plasma a fourth state of matter.

The name ‘plasma’ was introduced in 1929 by Irving Langmuir [10] who chose this name, because the multi-component, strongly interacting ionized gas reminded him of blood plasma. In a more rigorous way, a plasma can be defined as “*a quasi-neutral gas of charged and neutral particles characterized by a collective behavior*”[11].

The collective behavior originates from the motion of charged particles, which causes local concentrations of positive and negative electric charges. These charge concentrations create Coulomb fields that affect the motion of many other charged particles away from the original charges. Thus elements of the plasma continuously affect each other, giving the plasma its characteristic collective behavior. These local charge perturbations are confined to volumes of small dimensions. The characteristic dimension of such a charge perturbation is called the *Debye length*. In order for a plasma to be stable it is necessary that its dimensions are much larger than this Debye length. Outside of these tens of micrometers large volumes the positive and negative species densities are equal, making the plasma quasi-neutral.

## 1.2 The plasma sheath

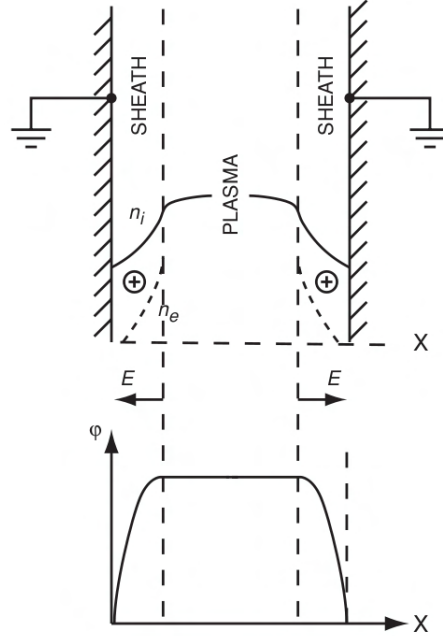


**Figure 1.1:** The top figure illustrates the charge density distributions in case a plasma is present between two surfaces at zero potential [1,2]. Total positive ion density is denoted with  $n_i$  and electron density is denoted with  $n_e$ . The  $\oplus$  denotes the positive charge in the sheath region. In the plasma region the densities of  $n_i$  and  $n_e$  are about equal. The bottom figure illustrates the resulting potential distribution and the direction of the electric field. The walls are at a lower potential because more electrons than ions reach the walls.

Although plasma is quasi-neutral in general, when it is in contact with a wall, non-quasi-neutral, positively charged thin layers called sheaths are formed. The example of a sheath between plasma and zero-potential surfaces is illustrated in figure 1.1. The formation of a positively charged sheath is due to the fact that electrons can move much faster than ions. For example, an electron thermal velocity ( $\sim \sqrt{T_e/m_e}$ ) exceeds that of ions ( $\sim \sqrt{T_i/M_i}$ ) by about 1000 times. The fast electrons stick to the walls, leaving the region near the walls (the sheath) for positively charged ions alone ( $n_i > n_e$ ). The positively charged sheath results in a potential profile illustrated in figure 1.1. The plasma bulk is quasi-neutral ( $n_i \simeq n_e$ ) and, hence, iso-potential ( $\phi = \text{constant}$ ) according to Poisson's equation,  $\nabla^2\phi = -\rho/\epsilon$ , where  $\phi$  is the electric potential,  $\rho$  is the charge density and  $\epsilon$  is the permittivity of the medium. Near the discharge walls the positive potential falls sharply, providing a high electric field, an acceleration of ions towards the wall and an acceleration of electrons away from the wall.

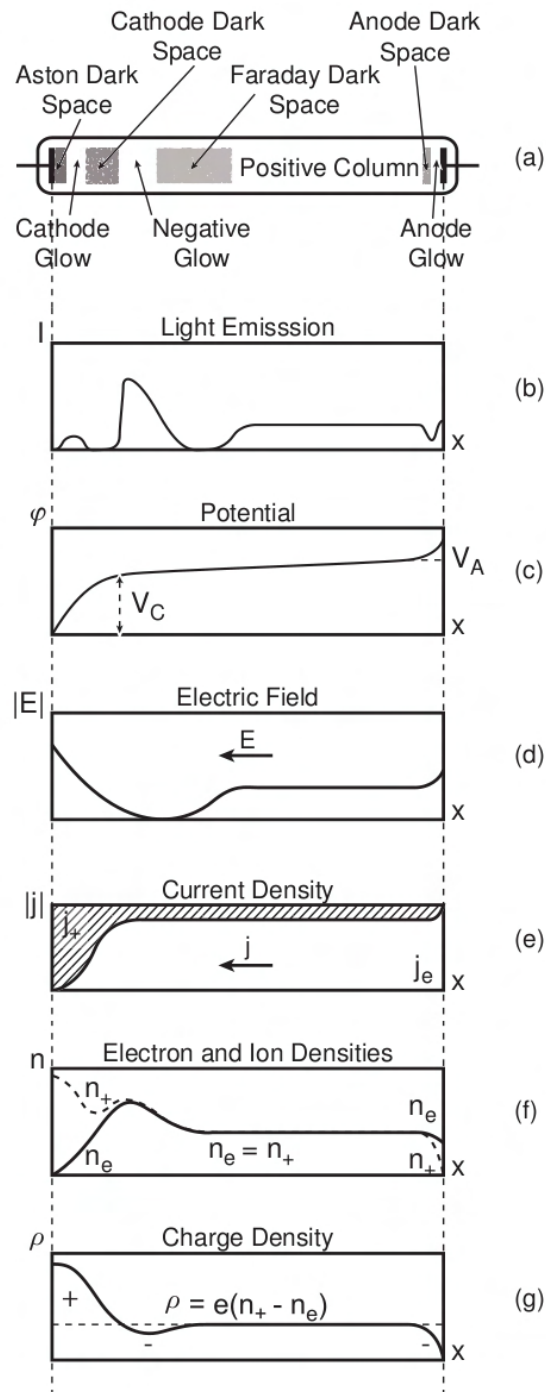


**Figure 1.2:** Illustration of the different regions that can be seen in a glow discharge together with their most important physical parameters [2].

## 1.3 Plasma regimes and structures

The discharges dealt with in this thesis are typically characterized by transient phenomena. This means that they are continuously changing plasma regimes and therefore also changing structures. Luckily these changes are always limited to transferring from the so-called glow discharge to Townsend discharge and back, where the intermediate regime is defined as the subnormal glow discharge. In the following these names for plasma regimes will be clarified.

The above mentioned collective behavior and the formation of the plasma sheath are responsible for the formation of the different structures in the plasma. The discharges under study are always compared with the specific structure of the glow discharge, because it is the best-known type of non-thermal discharge. This way the terminology and insights for this discharge, that has already widely been used and studied for more than a century, can be adopted in order to understand much more complicated discharges, such as transient discharges.

### 1.3.1 The glow discharge

#### At low pressure

The classical glow discharge can be defined as a self-sustained luminous direct current (DC) discharge with a cold cathode, which emits electrons as a result of secondary emission mostly induced by positive ions [2]. The different regions that can be observed in such a discharge and the related physical properties are illustrated in figure 1.2. The displayed setup is a classical glass discharge tube with a metal cathode on the left and an anode on the right several centimeters separated from each other in direct contact with a noble gas such as He or Ar at about 13 Pa.

Immediately adjacent to the cathode is a dark layer known as the *Aston dark space*. Then there is a relatively thin layer of the *cathode glow*, followed by the *cathode dark space*, which in its turn is sharply separated from the *negative glow*. The *negative glow* is gradually less and less bright towards the anode, becoming the *Faraday dark space*. After that the *positive column* begins, which is bright, though not as bright as the *negative glow*. The long and uniform *positive column* is transferred near the anode first into the *anode dark space* and finally into a narrow zone of the *anode glow*.

The glow pattern can be interpreted using the discharge parameter distributions shown in figure 1.2b to 1.2g [2]. Electrons are ejected from the cathode with about 1 eV of energy, which is insufficient for the excitation of atoms and explains the Aston dark space. By moving through the Aston dark space the electrons obtain enough energy from the high electric field for electronic excitation, which causes the cathode

glow. Further acceleration of electrons in the cathode dark space leads mostly to ionization, not to electronic excitation, because the energy becomes too high for efficient excitation. This explains the low level of radiation and increase of electron density in the cathode dark space. Slowly moving ions have a high concentration in the cathode layer and provide most of the current. A high electron density at the end of the cathode dark space results in a decrease of the electric field, electron energy and ionization rate, but leads to intensification of radiation. This explains the transition to the brightest layer, the negative glow. Farther from the cathode the electron energy decreases. This results in a transition from the negative glow to the Faraday dark space. At that position the plasma density decreases and the electric field builds up, establishing the positive column. In the interface region between the Faraday dark space and the positive column the electrons reach sufficiently high energy in order to excite the atoms. These excited species make the positive column also a luminous region. The cathode layer structure remains the same if electrodes are moved closer, whereas the positive column shrinks. The anode repels ions and pulls out electrons from the positive column, which creates the negative space charge and leads to an increase of the electric field in the anode layer. A reduction of the electron density explains the anode dark space, whereas the electric field increase explains the anode glow.

### **At elevated pressure**

The plasmas under study in this work are mostly operated at elevated pressures ranging from 0.05 to 1.013 bar or atmospheric pressure. This changes the discharge structure considerably, but the terminology and the underlying mechanisms remain the same. In order to generate a stable discharge between flat electrodes at elevated pressure, the distance between the electrodes needs to be reduced. This means a reduction from several centimeters, as illustrated in figure 1.2 for 13.33 Pa, to a separation of several millimeters for atmospheric pressure. Obtaining similar discharge properties at higher pressures by decreasing the interelectrode spacing is a tendency already known since 1889, when it was first described by Friedrich Paschen [12].

Increasing the pressure and decreasing the interelectrode spacing usually leads to a disappearance of the cathode glow, so that the Aston dark space and the cathode dark space become one very small region [13]. The most luminous region remains to be the negative glow, which is still separated from the mildly radiating positive column by the Faraday dark space. Whether the anode glow and the anode dark space are present or not, depends greatly on the physical properties of the anode [14, 15, 16]. With metal electrodes or electrodes covered with a resistive layer usually an anode glow is present with virtually no anode dark space. When there is a dielectric on the anode, there is usually a clear anode dark space without an anode

glow.

### 1.3.2 The Townsend discharge

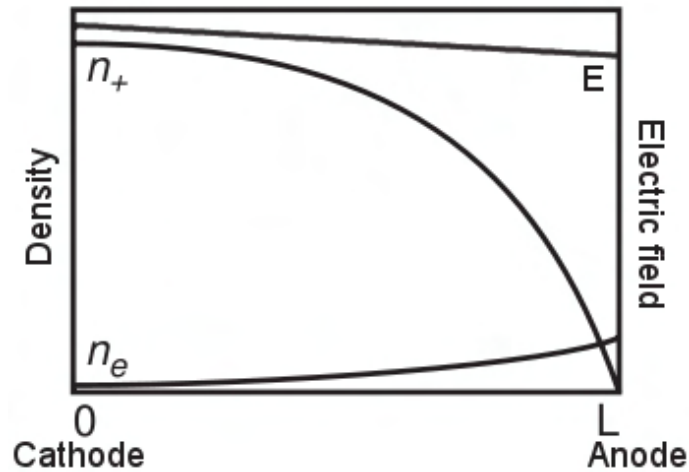


**Figure 1.3:** Distributions of electron and ion number densities and the typical accompanying electric field. The sketch illustrates that the ion density is usually much higher than the electron density and that the charge number densities are too low to disturb the electric field.

The typical electron and positive ion distributions for a Townsend discharge are illustrated in figure 1.3. Typically the ion densities are much larger than the electron densities, because much more electrons than ions are lost at the walls due to the higher electron mobility. In the Townsend discharge the electron and ion densities are too small to disturb the applied electric field with their space charges. As a consequence, there are no clear structural features as for the glow discharge structure in figure 1.2. Such a Townsend discharge is characterized at low pressures (tens of Pa) by a very low discharge current in comparison with the glow discharge and it does not emit visible light [13]. Therefore, it is sometimes also called the *dark Townsend discharge*. At atmospheric pressure, however, the discharge is characterized by a weak anode glow [17]. This regime is usually obtained if the voltage difference applied to the gas is exactly the breakdown voltage.

Considering the current density on the entire electrode, the low pressure Townsend discharge usually generates current densities ranging from  $10^{-9}$  to  $10^{-4}$  mA/cm<sup>2</sup>, while the glow discharge operates between  $10^{-3}$  and 1 mA/cm<sup>2</sup> [13,18]. At atmospheric pressure, however, the obtained operating range is usually much more lim-

ited to maximum current densities ranging from 0.01 to 1 mA/cm<sup>2</sup> for a Townsend discharge and from 1 to 100 mA/cm<sup>2</sup> for a glow discharge [9, 8, 19].

### 1.3.3 The subnormal glow discharge

The subnormal glow discharge is the intermediate regime between the Townsend discharge and the glow discharge. In this regime there is a space charge build-up near the cathode which is strong enough to disturb the electric field so that there is sheath formation. This manifestation of spatial structure and the presence of charged particles cause the electric field to energize the discharge much more efficiently, which considerably lowers the breakdown voltage in comparison with the Townsend discharge. This regime is mostly unstable, which can lead to temporal or spatial pattern formation [20], a transition into a glow discharge when energy increases or a transition into a Townsend discharge when energy decreases. Massines recently proposed [19] that when the electrodes are insulated this regime should be called the *inhibited atmospheric pressure glow discharge* (I-APGD), because it is neither a Townsend discharge nor a glow discharge and further development into a glow discharge is prevented somehow. This is probably due to the current limitation by the insulators and the use of an alternating current, but this is still under investigation [8, 21, 19]. Such a setup is called a dielectric barrier discharge and will be described in more detail later in this work.

## 1.4 The dielectric barrier discharge

### 1.4.1 History and background

The dielectric barrier discharge or DBD is an electrical discharge that is generated using two electrodes of which at least one is covered by an electrical insulator. As a consequence, it is not possible to generate the plasma by applying a DC voltage on one of the electrodes. This setup always requires the use of an alternating current. Several possible electrode arrangements are illustrated in figure 1.4. The setup that is mostly used for fundamental research is the planar reactor with both electrodes covered with a dielectric. These electrodes are mostly disc-shaped and have a diameter of about 4 cm [14, 8, 22]. Industrial use of this reactor is mostly gas conversion and for this purpose it is mainly the cylindrical reactor that is used. This setup has already been developed for more than 150 years ago and, consequently, has an extensive history.

The first experimental investigations of the dielectric barrier were reported in

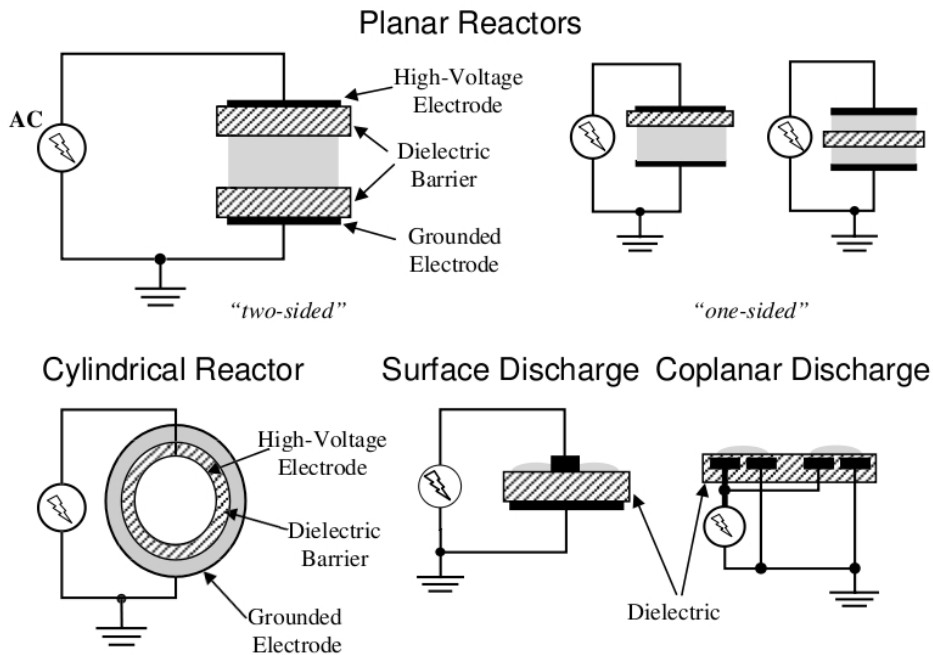


**Figure 1.4:** Typical arrangements for electrodes and dielectrics in DBDs [3].

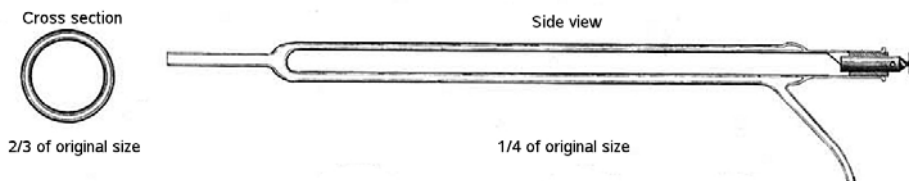


**Figure 1.5:** Drawings from Werner von Siemens of the cross section and the side view of his dielectric barrier ozonizer [4].

1857 by Werner von Siemens [4]. The research was mainly focused on the generation of ozone. This was done by blowing air or oxygen through an annular gap between two coaxial glass tubes of which the gas inlet was at the left and the outlet at the bottom. The inlet and outlet can be seen in the original drawing of the setup of Siemens, which is displayed in figure 1.5. The two electrodes were made of tinfoil, which was attached to the inside and outside of the cylinder and therefore outside of the discharge gap. The novelty of this setup was that the electrodes were not in direct contact with the plasma, which considerably increased their lifetime.

In the following decades the DBD research was mainly focused on the formation of ozone and  $N_xO_y$  compounds. At the beginning of the 20<sup>th</sup> century Emile Warburg in Berlin [23] conducted important investigations which lead to a much

better control of these discharges. In the 1920s Otto [24] and Becker [25] separately industrialized the designs of the ozone generators. In the 1930s it was discovered by Buss [26] that the breakdown of air between planar parallel electrodes covered by dielectrics always occurs in a large number of tiny short lived current filaments. He obtained the first traces of these microdischarges on photo-sensitive plates (Lichtenberg figures) and was able to obtain oscilloscope recordings of their current and voltage properties. An example of such a filamentary discharge is shown in figure 1.6.

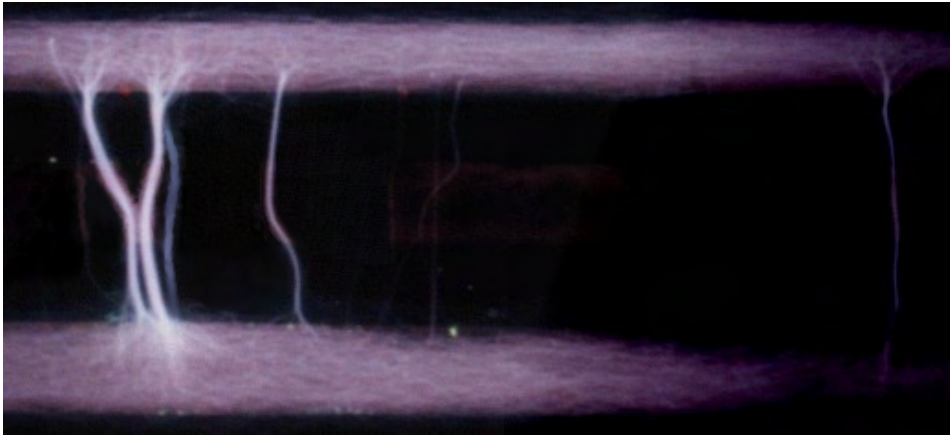


**Figure 1.6:** The manifestation of filaments in an atmospheric pressure dielectric barrier discharge [5].

The atmospheric pressure DBD typically operates in the filamentary mode, but under specific operating conditions it is also possible to operate it in a diffuse mode, where spatial homogeneity in the direction parallel to the electrodes is obtained. This enables the discharge to be used for homogeneous surface treatments at atmospheric pressure. The investigations and successes of this discharge mode start around 1976 when Donohoe finished his PhD research on the development and characterization of glow discharges in mixtures of helium and acetylene in this setup [27]. In 1987 and afterwards uniform dielectric barrier glow discharges were developed in the research group of Okazaki [28]. They used an electrode configuration using two metal foils covered with a special metal mesh and ceramic dielectrics. In this way homogeneous discharges were obtained in helium, nitrogen, air, oxygen and argon, even with or without the addition of organic precursors. They proposed to use the term atmospheric pressure glow discharge or APGD.

About five years later Roth and coworkers developed at the university of Tennessee a similar uniform dielectric barrier discharge reactor. Without using a special metal mesh on the electrodes they were able to obtain uniform glow discharges in helium and argon between electrodes with a separation length of several centimeters

[29].

In 1992 and afterwards Massines and her team made essential contributions to the understanding of the glow mode in the atmospheric pressure DBD using both experiments and simulations on mainly He and N<sub>2</sub> discharges [14, 17, 30]. They made important steps in understanding which elementary processes are responsible for the existence of the glow mode. More recent activities of several teams [17, 9, 8, 31, 32, 33, 34] focused on obtaining high temporally and spatially resolved spectroscopic measurements as well as on developing detailed theoretical models, where the objective mainly lies in obtaining a better understanding in order to control these sometimes unstable transient discharges.

These research efforts led to the insight that the generation of stable diffuse DBDs at atmospheric pressure requires special operating conditions, which are greatly determined by the properties of the feeding gas. A crucial point seems to be that the initial ionization process should be somewhat stimulated by a high level of pre-ionization, Penning ionization by metastables and the possibility of direct ionization at low electric fields. The first phenomenon, *pre-ionization*, means the ionization processes that are not directly related to the electric field, such as ionization by external UV radiation, thermal desorption of electrons from a dielectric surface or residual ionization from some previous discharge phenomenon. The second phenomenon, *Penning ionization*, is the ionization by collision of a metastable with a species having an ionization threshold below the metastable energy (e.g.  $\text{He}_m^+ \text{X} \rightarrow \text{He} + \text{X}^+ + \text{e}^-$ ). Helium metastables, for example, have an internal energy of about 20.2 eV, which allows them to ionize N<sub>2</sub> with an ionization threshold of 15.6 eV. The third phenomenon, *direct ionization at low electric field*, focuses on the efficiency that energy from the electric field is transferred to the discharge gas. This efficiency is much higher for atomic gases such as He and Ar, because there is no energy lost to the molecular internal energy modes such as rotation and vibration, hence, a lower electric field can be used to generate the discharge. This effect promotes stable discharge operation, but is not yet fully understood.

These insights suggest that the stability of the diffuse mode in a DBD is sensitive to impurities, admixtures and residual ions. Residual ion densities from a previous discharge pulse depend on the repetition frequency of the applied voltage. Another crucial mechanism in a DBD is the charge accumulation on the dielectric material. Some materials accumulate charges much more homogeneously than others [35]. This is also a determining factor for the spatial homogeneity, because these charges influence the electric field and vice versa, because some of these charge carriers are released back into the gas when the electric field changes polarity.

The argumentation based on the pre-ionization mechanisms is not generally accepted. In the group of van de Sanden an electronic feedback system was developed [36] which is based on limiting the current in order to prevent transitions to an arc dis-

charge, a much more powerful discharge which would damage the dielectric materials. Their electronic feedback circuit prevents these transition mechanisms and is successful in obtaining homogeneous dielectric barrier discharges. Consequently, this is used as an argument to state that it is the current limitation which determines the formation of a homogeneous glow and not the pre-ionization and it is implied that there are other still unknown mechanisms which are able to produce electrons at a low electric field [35].

There still remain unanswered questions to be solved [19]. These questions mainly concern the nature and formation of the subnormal discharges, the influence of the charges on the dielectric on the secondary electron emission coefficient, the possible detachment of electrons from the dielectric surface when polarity of the electric field is reversed, the role of impurities on the composition of the gas, the role of these impurities on the electrical properties of the discharge and finally how the use of a resistor or a coil in the electrical circuit avoids filamentation of the discharge. In this work we will attempt to solve some of these questions.

## 1.4.2 Applications

Until about ten years ago, ozone generation was the major industrial application of DBDs with thousands of installed ozone generating facilities used mainly in water treatment [37]. For this reason the dielectric barrier discharge is sometimes also referred to as the ‘ozonizer discharge’. The extensive research activities employing modern diagnostic and modeling tools started around 1970. Although they were originally aimed at a better understanding of the physical and chemical plasma processes in ozonizers, these research efforts resulted not only in improved ozone generators, but also in a number of additional applications of dielectric-barrier discharges.

The principal gravity of this invention and its applications nowadays lies in the ability to use the DBD to ionize atmospheric pressure gases, while keeping the gas temperature low ( $T < 1000$  K). This means that a highly non-equilibrium situation is created where the electrons have energies up to several electronvolts, while the gas temperature remains rather low, sometimes even as low as room temperature. This also means that there is no need for a robust vacuum system, but that the processes can take place without a pressure difference with the outside world and sometimes even in the open air. These applications can be divided in four categories, namely *gas treatment*, *surface treatment*, *light generation* and *analytical ionization source*.

Besides ozone production [38], gas treatments using DBDs include cleaning of gas streams and gas conversion processes to partially oxidize  $\text{CH}_4$  into the much more valuable  $\text{CH}_3\text{OH}$  [39]. Surface treatments of DBDs include cleaning, sterilization, increasing wettability and adhesion properties [40], deposition of polymer coatings,

thin SiO<sub>2</sub> layers or even diamond like carbon film [37]. Lighting purposes with DBDs include the excitation of CO<sub>2</sub> lasers [41], excimer lamps [42] and more recently, the discharge cells in large area plasma display panels [43]. The DBD ionization sources are developed to be used in low power and small analytical devices mostly driven by noble gases [44].

# Chapter 2

## Numerical simulations

### 2.1 Motivation for numerical simulation

Experimental physics is the base for understanding natural phenomena. Experimental observations lead to new theories and the discovery of proportionalities, which allows mathematical formulations of these theories. These descriptions can be tested and improved by additional observations up till the point where these observations become too difficult. Obstacles for such observations are for example that the phenomenon happens too fast, or that the setup becomes too small or too large, or that the materials under study are very expensive or very dangerous. These issues can be avoided if certain physical influences or experiments can be described or tested by using theoretical descriptions.

The equations used in these descriptions can be solved exactly or they can be solved numerically. Solving these equations numerically means that they have to be discretized in both space and time, so that by choosing an appropriate initial condition and by respecting the boundary conditions, the described system is recalculated again and again so that it iteratively evolves into the desired converged solution. Both the exact as the numerical solutions of these equations have their advantages and disadvantages, but basically the numerical methods are being used more and more, because they are able to describe enormously complex systems and can be defined much more generally than the exact solutions. As a consequence, numerical methods are being used nowadays in about every engineering environment, because it is generally cheaper to calculate the performance of a new system on a computer than to develop it in real life.

For the plasmas encountered in this work there exist various useful theoretical descriptions. In the next section a brief overview is given of the possible useful descriptions and their advantages and disadvantages. This will form a solid background for the subsequent section where a description is given of the model used in this work.

## 2.2 Simulation methods

### 2.2.1 Analytical

Solving the equations that describe the plasma directly, provides for simple formulas which are easy to use. In this way analytical expressions are obtained, which allows that results are obtained immediately by filling in basic operating parameters such as pressure, temperature and voltage [45]. An analytical expression does not need an iterative procedure to obtain a solution. This means that under the assumptions that have been made very reliable results can be obtained, independent of numerical procedures. Without these very specific assumptions it is not possible to obtain an analytical solution. As a consequence, the obtained expressions are only applicable in specific isolated cases, which is the most important drawback of this method. Such descriptions are not suitable for the investigations in this work, where we want to obtain a broad characterization and detailed insights. Hence, it is desirable to obtain spatial distribution profiles of species densities, energy and electric potentials for several situations. Therefore, it is not efficient to derive a separate analytical expression for each parameter of interest.

### 2.2.2 Kinetic

#### Solving the Boltzmann equation

Numerical models of gas discharges must always be built upon a microscopic description of particles in the discharge [46]. Most plasma models are built upon the Boltzmann equation. The Boltzmann equation describes the evolution of the density  $f(\mathbf{r}, \mathbf{v}, t)$  of a single particle species in the phase space spanned by configuration space  $\mathbf{r}$  and velocity space  $\mathbf{v}$ . Often the Boltzmann equation is written as [47]:

$$\frac{\partial f}{\partial t} + \mathbf{v} \cdot \frac{\partial f}{\partial \mathbf{r}} + \mathbf{a} \cdot \frac{\partial f}{\partial \mathbf{v}} = \left( \frac{\partial f}{\partial t} \right)_c \quad (2.1)$$

where  $\mathbf{a}$  is the acceleration of the particle and  $(\partial f / \partial t)_c$  is the change of the distribution function  $f$  due to collisions.

Numerical solution of the full Boltzmann equation is a very complex problem. Direct use is mostly approached by assuming spatial uniformity and using imposed electric fields [48, 49]. This method is used very often to determine the electron energy distribution functions (EEDFs) at different average electron energies. These EEDFs can then further be used to calculate input for a fluid model, such as electron

transport coefficients and rate coefficients.

### Using a sampling method

A completely different kinetic approach is by following individual particles in the discharge. The trajectories of the particles are calculated using the laws of Newton and the interactions or collisions between the particles are described using a Monte Carlo method, which determines which event takes place by evaluating the probabilities of the different interactions. Usually there are too many particles to follow each of them individually. Therefore, often a smaller set of particles is simulated, which is taken to be representative for the entire discharge.

When the trajectories of individual particles in the discharge are calculated, the calculation time is greatly depending on the amount of particles and therefore also the gas pressure. This is feasible when working at low pressures ( $p < 20Pa$ ), but would require an enormous calculation time for the discharges under study, which operate between 25 to 1100 mbar. Such models possess a very high degree of reliability, because they only require few simplifications, but this comes at the cost of a high computational demand.

### 2.2.3 Molecular dynamics

Molecular dynamics is a simulation technique which operates on the space and time scales of atomic interactions. The atoms and their behavior are described by determining the forces between the atoms using empirical potential energy functions [50]. Such techniques can not be used to describe a plasma, because charged particle interactions are often not directly taken into account in the potential energy functions and, moreover, a plasma usually consists of too many particles.

However, molecular dynamics is extremely useful to determine the interaction of the particles with the surface, especially when dielectrics are used. When high or low energy particles in a plasma hit a dielectric they can reflect, stick or detach an atom or atoms from the dielectric material. Such process can change the dielectric properties of the material or can be the source of impurities in the discharge. A more general insight by molecular dynamics simulations could be very useful in this matter, however, molecular dynamics is very dependent on the empirical potential energy function that is used and for some interactions these functions are not yet available.

## 2.2.4 Fluid

In fluid models the various discharge species are described in terms of average, hydrodynamic quantities such as density, momentum and energy. By taking the velocity moments of the Boltzmann equation (eq. 2.1) conservation equations for these quantities are obtained. The velocity moments are obtained by multiplying the Boltzmann equation with the velocity dependent function  $A(\mathbf{r}, \mathbf{v}, t)$  and then integrating it over velocity space. In this way continuity equations are obtained for density, momentum and energy. These are not solved for every species. Nowadays there is a general agreement that fluid models must include the continuity and the momentum transfer equations for electrons and ions, the electron mean energy transport equation and finally Poissons equation in order to determine the electric field. Typically the problem is solved self-consistently either in one-dimensional [51] or two-dimensional [52] geometries.

In fluid models the quantities of the species such as density, momentum and energy are calculated and particles or molecules are not followed individually. This makes fluid models so fast that reliable results are mostly obtained within a few hours. The theory behind fluid models assumes that the plasma must have a high enough density so that it resembles a continuum. At pressures above 30 Pa this is a rather safe assumption to make [52] and it makes the fluid model the best choice to simulate the plasmas in this work in the pressure range from 25 to 1100 mbar.

## 2.2.5 Hybrid

Hybrid models are the combinations between different types of models, in order to combine the advantages of the different types and to compensate for their limitations. Most of the present modeling approaches are hybrid in one way or the other. The low pressure Monte Carlo models are often used in combination with a ‘Particle in Cell’ method [53, 54], which weights the charges of the different particles on a grid so that a charge distribution is obtained, which allows that the Poisson equation can be used to calculate the electric field self consistently. At higher pressures the Monte Carlo method is often used in combination with a fluid model [55, 46]. The Monte Carlo model makes the evaluations whether a certain reaction takes place based on the energy dependent cross sections of those reactions and it can return calculated reaction rates to the fluid model.

The fluid model that is used in this work is also used in a hybrid way. It is used in combination with a program that uses a space averaged solution of the Boltzmann equation together with imposed electric fields. Such model is often referred to as a ‘Boltzmann solver’ and it calculates the energy dependent reaction rate coefficients and transport coefficients for the electrons, which are used as an input for the fluid model.

## 2.3 Fluid model used in this work

### 2.3.1 Historical background

In order to describe the plasmas under study in this work the fluid model MD2D is used. It originates from the University of Eindhoven, where it was first developed by G. Hagelaar [43] in order to simulate the discharge cells used in display technology. Later it was further optimized by W. Brok [46] and J. van Dijk [56] who worked on the integration of the model into the object oriented modeling framework that is called Plasimo [57]. At the same time W. Brok used the model to develop a hybrid fluid Monte Carlo model in order to simulate the breakdown phenomena in transient discharges such as fluorescent lamps.

### 2.3.2 Physical background

The used fluid model is based on the first three velocity moments of the Boltzmann equation (eq. 2.1). These velocity moments are calculated by multiplying the Boltzmann equation with a function  $A(\mathbf{r}, \mathbf{v}, t)$  and then integrating it over velocity space. For the details on these equations I refer to the work of A. Salabas [58] who has written a discussion on the derivation and the validity of these equations. The first equation is obtained by using  $A \equiv \mathbf{v}^0 = 1$  which produces the density conservation equation:

$$\frac{\partial n_i}{\partial t} + \nabla \cdot \mathbf{\Gamma}_i = S_{i,reactie} \quad (2.2)$$

In this equation  $n_i$  is the density of species  $i$ ,  $\mathbf{\Gamma}_i$  is the flux of  $i$  and  $S_i$  is the source term which describes the net rate of change in density of  $i$  due to chemical reactions expressed as:

$$S_i = \sum_r c_{i,r} R_{i,r} = \sum_r \left[ c_{i,r} k_r \prod_j n_j \right] \quad (2.3)$$

where  $r$  is the index of a production or destruction reaction of  $i$ ,  $c_{i,r}$  is the stoichiometric coefficient of  $i$  in reaction  $r$ ,  $R_{i,r}$  is the reaction rate,  $k_r$  is the reaction rate coefficient and  $j$  is the index for a reacting species.

The description of the flux term  $\mathbf{\Gamma}_i$  is derived from the second velocity moment of the Boltzmann equation, which is obtained by using  $A \equiv m\mathbf{v}^1$ . The obtained

momentum conservation equation is then transformed into the ‘drift-diffusion’ equation:

$$\mathbf{\Gamma}_i = \mu_i n_i \mathbf{E} - D_i \nabla n_i \quad (2.4)$$

The coefficients  $\mu_i$  and  $D_i$  represent the electric mobility and the diffusion coefficient of species  $i$  respectively. In order to obtain this equation, some assumptions have been made. It is assumed that both inertia and viscosity effects are negligible and that the diffusion and mobility coefficients are completely determined by collisions with the background gas and these can be expressed as:

$$\mu_i = q_i / (m_i \nu_{i-0}) \quad (2.5)$$

$$D_i = k_B T_i / (m_i \nu_{i-0}) \quad (2.6)$$

where  $q_i$  is the charge of species  $i$ ,  $m_i$  is the mass of species  $i$ ,  $\nu_{i-0}$  is the momentum transfer collision frequency of species  $i$  with the background gas,  $k_B$  is Boltzmann’s constant and  $T_i$  is the temperature of species  $i$ . Note that this implicitly confirms Einstein’s diffusion-mobility relation:

$$\frac{D_i}{\mu_i} = \frac{k_B T_i}{q_i} \quad (2.7)$$

In order to be able to write the diffusion term in the drift-diffusion equation (eq. 2.4) as  $-D_i \nabla n_i$  it is assumed that the diffusion described in the gas is dominated by the density gradient and that diffusion by temperature gradient can be neglected [58,59]. For the neutral species is the first term in equation 2.4 zero, because they do not interact with the electric field.

The third velocity moment is obtained by taking  $A \equiv mv^2/2$  and provides for the energy density conservation equation. Because the heavy particles are assumed to be in thermal equilibrium with the electric field, this equation is only solved for the electrons and can be written in the same form as the density conservation equation (eq. 2.2):

$$\frac{\partial n_\varepsilon}{\partial t} + \nabla \cdot \mathbf{\Gamma}_\varepsilon = S_\varepsilon \quad (2.8)$$

where  $n_\varepsilon$  is the electron energy density, defined as  $n_\varepsilon = n_e \bar{\varepsilon}$ , with  $\bar{\varepsilon}$  as the average electron energy. It is then assumed that this mean electron energy results mainly from random motion so that the electron velocity distribution is isotropic so that we can relate a temperature to the mean electron energy using  $k_B T_e = \frac{2}{3} \bar{\varepsilon}$ . This allows that the energy density flux can be written as [58]:

$$\mathbf{\Gamma}_\varepsilon = \frac{5}{3} \mu_e \mathbf{E} n_\varepsilon - \frac{5}{3} D_e \nabla n_\varepsilon \quad (2.9)$$

The source term  $S_\varepsilon$  in equation 2.8 has a slightly different form than the species source term (i.e. eq. 2.3), because there is an additional term for the Ohmic heating of the electrons by the electric field:

$$S_\varepsilon = -e\Gamma_e \cdot \mathbf{E} + \sum_r c_r \bar{\varepsilon}_r R_r \quad (2.10)$$

The second term in the above equation represents the change in electron energy due to chemical reaction, where  $\bar{\varepsilon}_r$  is the energy lost or gained by one electron in reaction  $r$ .

In our model the neutral gas temperature is assumed to be constant and uniform throughout the reactor. The temperature of ion  $i$  is increased with the energy gained from the electric field [60,61] using

$$k_B T_i = k_B T_g + \frac{m_i + m_g}{5m_i + 3m_g} m_g (\mu_i \mathbf{E})^2 \quad (2.11)$$

where the index  $g$  indicates the background gas. The ion temperature  $T_i$  is used to calculate the ion diffusion coefficient from the mobility coefficient using the Einstein relation (eq. 2.7).

The conservation equations are solved iteratively together with the Poisson equation:

$$\nabla \cdot (\epsilon_m \mathbf{E}) = -\nabla \cdot (\epsilon_m \nabla V) = \rho \quad (2.12)$$

where  $\epsilon_m$  is the permittivity of the medium and  $\rho$  is the charge density calculated by:

$$\rho = \sum_i q_i n_i \quad (2.13)$$

with  $n_i$  being a charged species density.

### 2.3.3 Boundary conditions

In order to solve the above system of equations boundary conditions need to be defined. There are open boundaries such as an opening in the wall or the axis of symmetry and there are physical boundaries such as an electrode or a dielectric. At the open boundaries homogenous Neuman boundary conditions are used. This means that the gradient of the quantities in the directions perpendicular to these boundaries are set to zero. As a consequence, for all particles is  $\nabla n_i \cdot \mathbf{e}_n = 0$ , for the electron energy density is  $\nabla n_\varepsilon \cdot \mathbf{e}_n = 0$  and for the electric potential is  $\nabla V \cdot \mathbf{e}_n = 0$ , where  $\mathbf{e}_n$  is the unit vector normal to the boundary.

At the physical boundaries the densities are described using flux expressions which include the effects of reflection and secondary electron emission. This means that for the electrons there is an additional production source term described by  $\sum_i \gamma_i \Gamma_i$ , where  $i$  is the index for a summation over the ions and  $\gamma_i$  is the secondary electron emission coefficient of  $i$ . The boundary condition of the electron energy density is defined in a way consistent with the electron densities [43,59].

The boundary condition for the electric potential at an electrode is a predefined value. This is 0 V at the grounded electrode and is  $V(t)$  at the powered electrode, where  $V(t)$  can be the value of a DC voltage, a sine function, a rectangular voltage or a pulsed DC signal. Inside the dielectrics Poisson's equation (eq. 2.12) is used to calculate the electric potential. The gradient of the potential distribution inside the dielectrics is always constant, because there is no space charge present. Since a dielectric is not conducting, a surface charge  $\sigma$  accumulates on it and it is calculated by:

$$\sigma = \int \mathbf{j} \cdot \mathbf{e}_t dt \quad (2.14)$$

with  $\mathbf{e}_t$  as the normal vector pointing towards the wall and  $\mathbf{j}$  as the current density:

$$\mathbf{j} = \sum_i q_i \Gamma_i \quad (2.15)$$

The effect of the surface charge  $\sigma$  is taken into account using Gauss's law:

$$\epsilon_d \mathbf{E}_d \cdot \mathbf{e}_t - \epsilon_g \mathbf{E}_g \cdot \mathbf{e}_t = \sigma \quad (2.16)$$

where  $\epsilon_d$  and  $\mathbf{E}_d$  respectively are the permittivity and the electric field inside the dielectric and  $\epsilon_g$  and  $\mathbf{E}_g$  are the permittivity and the electric field inside the discharge gas.

### 2.3.4 Solving the fluid equations

The spatial discretization of the equations uses the control volume method [43,46]. The equations are solved using a method closely resembling the method derived by Patankar [43,46,62].

In one iteration step first the Poisson equation (eq. 2.12) is solved, next the species densities are calculated from the density continuity equation (eq. 2.2) and finally the electron energy continuity equation is solved (eq. 2.8). These equations are then solved iteratively until convergence is reached. The details of the implementation of this model and discussions on the implementation can be found in the works of G. Hagelaar, W. Brok and D. Mihailova [43,46,59].

## Part II

# The characterization of plasma sources used for analytical spectrometry



# Chapter 3

## Characterization of a dielectric barrier microdischarge

### 3.1 Introduction

During the last decade, there has been an increased interest in the miniaturization of analytical instrumentation and methods, also called ‘lab on a chip’. In this respect, a lot of attention goes to miniaturized plasma sources. One of the most important advantages of these so-called microplasmas is the low instrumentation and operation costs, because smaller amounts of sample and reagents can be used. Moreover, high-throughput measurements might become possible, if several plasmas are used in parallel. Finally, because the miniaturized plasma sources are much smaller, it is possible to construct a portable device, which is much easier to be used outside of the laboratory.

Microplasmas exist in various configurations, operating at either atmospheric or reduced pressure. The generated discharges can be direct current (DC) glow discharges used as molecular emission detectors [63, 64, 65, 66], capacitively coupled radio-frequency (CC-RF) discharges [67, 68, 69, 70, 71, 72] including furnace atomization plasma excitation sources [73, 74, 75, 76, 77, 78], microwave induced plasmas based on the microstrip technology [79, 80, 81], miniature inductively coupled plasmas [82, 83, 84], electrolyte-as-cathode glow discharges (ELCAD) [85, 86, 87, 88, 89] and liquid-sampling atmospheric pressure glow discharges (LS-APGD) [90, 91, 92, 93], dielectric barrier discharges (DBDs) [44, 94, 95, 96, 97], microstructured electrode discharges (MSD) [95, 98, 99] and some other variations [100]. Several good review papers can be found in the literature, giving an overview and a description of these different types of analytical microplasmas [101, 98, 102, 103]. Moreover, microplasmas in various configurations are also of great interest for other than analytical spectrometry applications [104].

In the present chapter, numerical simulations are used to investigate the plasma

characteristics of a microplasma, more specifically a DBD, as developed by Niemax and coworkers [44,94,95,96]. A DBD is typically formed between two parallel electrodes, with a gap distance in the order of 0.1 – 10 mm. One or both electrodes are covered with a dielectric barrier. Hence, the DBD cannot be operated with direct current (dc), because of dielectric charging issues. Typically they are operated with sinusoidal wave currents, square wave currents or pulsed wave forms with a frequency ranging from a few Hz to MHz, and mostly in the kHz-range [105].

Niemax and coworkers have developed a DBD operating at reduced pressure ( $\sim 10$ -180 mbar) and applied it as a microchip source for analytical spectrometry [44,94,95,96]. This type of DBD was characterized by a dielectric layer on each of the electrodes. It was demonstrated to be a small, low electric power ( $< 1$  W), low gas temperature ( $\sim 600$  K) plasma source, with excellent dissociation capability for molecular species. It has been used in plasma modulation diode laser absorption spectrometry of excited chlorine and fluorine, with typically helium or argon as the plasma gases.

In order to obtain a better insight in the plasma characteristics of the DBD, we have described the behavior of the various plasma species using a fluid model. In the next section the details of the simulations will be given.

## 3.2 Description of the simulations

### 3.2.1 Chemistry

The fluid model and its equations is described in Chapter 2. The simulated discharge gas is helium and it is described using 7 chemical species and 21 chemical reactions. The species included in the model are electrons,  $\text{He}^+$  and  $\text{He}_2^+$  ions, He ground state atoms,  $\text{He}_2^*$  dimers, He atoms excited to the metastable levels,  $\text{He}(2^3\text{S})$  and  $\text{He}(2^1\text{S})$ , which are combined into one level  $\text{He}_m^*$ , and He atoms into higher excited levels ( $n > 2$ ), lumped together into one effective level  $\text{He}^{**}$ . This method of combining several levels into an effective level is commonly used in modeling [106,107], in order to limit the complexity of the calculations, when the focus is on the general plasma characteristics instead of on the detailed behavior of the excited levels [9].

The reactions that are described in the model define the production and loss processes of the different species in the discharge. They are summarized in Table 3.1, with references to the rate coefficients or cross sections used. Note that for most of the electron-induced processes, the reaction rates are calculated based on energy-dependent cross sections. The reaction rate coefficients are calculated with a separate program called BOLSIG+ [49], which is based on solving a space aver-

**Table 3.1:** Complete set of reactions used in the model with their reaction rate coefficients.

No.	Reaction	Reaction Coefficient	Ref.
0	$e^- + \text{He} \rightarrow e^- + \text{He}$	$k = f(\sigma(\bar{\epsilon}))$	[6]
1	$e^- + \text{He} \rightarrow e^- + \text{He}_m^*$	$k = f(\sigma(\bar{\epsilon}))$	[6]
2	$e^- + \text{He} \rightarrow e^- + \text{He}^{**}$	$k = f(\sigma(\bar{\epsilon}))$	[6]
3	$e^- + \text{He} \rightarrow 2 e^- + \text{He}^+$	$k = f(\sigma(\bar{\epsilon}))$	[6]
4	$e^- + \text{He}_m^* \rightarrow 2 e^- + \text{He}^+$	$k = f(\sigma(\bar{\epsilon}))$	[7]
5	$e^- + \text{He}_m^* \rightarrow e^- + \text{He}$	$k = 2.9 \times 10^{-15} \text{ m}^3 \text{ s}^{-1}$	[108, 109]
6	$e^- + \text{He}_2^* \rightarrow e^- + 2 \text{He}$	$k = 3.8 \times 10^{-15} \text{ m}^3 \text{ s}^{-1}$	[108]
7	$\text{He}^+ + 2 e^- \rightarrow \text{He}_m^* + e^-$	$k = 6.0 \times 10^{-32} \text{ m}^6 \text{ s}^{-1}$	[108]
8	$\text{He}_2^+ + 2 e^- \rightarrow \text{He}_m^* + \text{He} + e^-$	$k = 2.8 \times 10^{-32} \text{ m}^6 \text{ s}^{-1}$	[108]
9	$\text{He}_2^+ + e^- + \text{He} \rightarrow \text{He}_m^* + 2 \text{He}$	$k = 3.5 \times 10^{-39} \text{ m}^6 \text{ s}^{-1}$	[108]
10	$\text{He}_2^+ + 2 e^- \rightarrow \text{He}_2^* + e^-$	$k = 1.2 \times 10^{-33} \text{ m}^6 \text{ s}^{-1}$	[108]
11	$\text{He}_2^+ + e^- + \text{He} \rightarrow \text{He}_2^* + \text{He}$	$k = 1.5 \times 10^{-39} \text{ m}^6 \text{ s}^{-1}$	[108]
12	$\text{He}^{**} + \text{He} \rightarrow \text{He}_2^+ + e^-$	$k = 1.5 \times 10^{-17} \text{ m}^3 \text{ s}^{-1}$	[9]
13	$\text{He}_m^* + \text{He}_m^* \rightarrow \text{He}_2^+ + e^-$	$k = 2.0 \times 10^{-15} \text{ m}^3 \text{ s}^{-1}$	[108, 109]
14	$\text{He}_m^* + \text{He}_m^* \rightarrow \text{He}^+ + \text{He} + e^-$	$k = 8.7 \times 10^{-16} \text{ m}^3 \text{ s}^{-1}$	[108, 109]
15	$\text{He}^+ + 2 \text{He} \rightarrow \text{He}_2^+ + \text{He}$	$k = 6.5 \times 10^{-44} \text{ m}^6 \text{ s}^{-1}$	[108]
16	$\text{He}_m^* + 2 \text{He} \rightarrow \text{He}_2^+ + \text{He}$	$k = 1.9 \times 10^{-46} \text{ m}^6 \text{ s}^{-1}$	[108]
17	$\text{He}_m^* + \text{He}_2^* \rightarrow \text{He}^+ + 2 \text{He} + e^-$	$k = 5.0 \times 10^{-16} \text{ m}^3 \text{ s}^{-1}$	[108]
18	$\text{He}_m^* + \text{He}_2 \rightarrow \text{He}_2^+ + \text{He} + e^-$	$k = 2.0 \times 10^{-15} \text{ m}^3 \text{ s}^{-1}$	[108]
19	$\text{He}_2^* + \text{He}_2^* \rightarrow \text{He}^+ + 3 \text{He} + e^-$	$k = 3.0 \times 10^{-16} \text{ m}^3 \text{ s}^{-1}$	[108]
20	$\text{He}_2^* + \text{He}_2 \rightarrow \text{He}_2^+ + 2 \text{He} + e^-$	$k = 1.2 \times 10^{-15} \text{ m}^3 \text{ s}^{-1}$	[108]
21	$\text{He}_2^* + \text{He} \rightarrow 3 \text{He}$	$k = 4.9 \times 10^{-22} \text{ m}^3 \text{ s}^{-1}$	[9]

aged solution of the Boltzmann equation as was addressed in Chapter 2, Sections 2.2.2 and 2.2.5. In the program the exponential spatial growth model was used, as is recommended [49]. This program is applied for a wide range of different, fixed reduced electric fields. A reduced electric field in this context is the ratio of the electric field strength to the density of the background gas. For each value of the reduced electric field, the average electron energy, the mobility of the electrons and the rate coefficients of the various electron-induced processes are tabulated. Using these tables, the rate coefficients, the mobilities and the diffusion coefficients will be applied, which correspond to the electron energy calculated with the energy density conservation equation (eq. 2.8 Chapter 2).

The cross sections of the electron-induced reactions are plotted as a function of electron energy in Figure 3.1. Beside two electron induced ionization reactions (solid lines) and two electron induced excitation reactions (small dashed lines), also the cross section of the electron-induced elastic reaction is plotted (large dashed line), because this reaction is also included in the Boltzmann model. It is clear that the electron induced excitation and ionization reactions from the He ground state

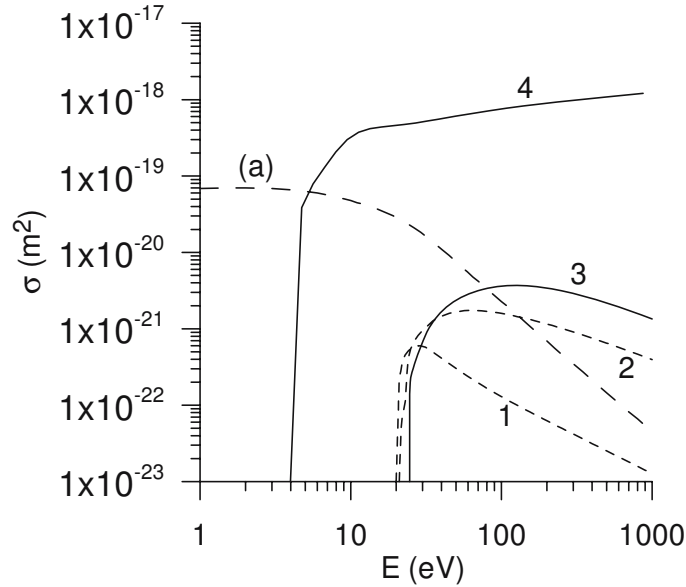


**Figure 3.1:** Cross sections of the different electron-induced processes as a function of electron energy. The labels correspond to the numbers in Table 3.1. The label (a) denotes the electron elastic cross section for He atoms, which only changes the electron energy in the model, not the species densities. Label (1) indicates the electron-induced excitation to the He metastable levels  $\text{He}_m^*$ , (2) the electron induced excitation to the higher excited He levels  $\text{He}^{**}$ , (3) the electron-induced ionization from the He ground state and (4) the electron-induced ionization from the He metastable level. These cross-sections were adopted from the Siglo Database [6], except for the cross section of reaction 4 which originates from the work of Janev and coworkers [7].

have a lower value and a higher threshold energy than the electron induced ionization reaction from the  $\text{He}_m^*$  level. The latter process, however, only occurs with He metastable atoms, which generally have a much lower number density in the plasma than the He ground state atoms, so that this process is not so important, in spite of the larger cross section.

The electron induced de-excitation and dissociation reactions, i.e., reactions 5 and 6 in Table 3.1, are treated independently of the electron energy. This independence is one of the experimental results in the detailed study of the elementary processes in high-pressure He of Deloche and coworkers [108]. Since we based most of our chemical description on their study, we tried to stay as much consistent with their results as possible. With respect to the excited states, our main interest is in the species with longer lifetimes (i.e.,  $\text{He}_m^*$  and  $\text{He}_2^*$ ), since they are considered the most important in determining the plasma properties [9, 8, 106, 108].  $\text{He}_m^*$  and  $\text{He}_2^*$  can also be excited to a radiative level and undergo radiative relaxation, but we did not consider these processes, because the superelastic de-excitation (i.e., reactions 5 and

6 in Table 3.1) is a much more efficient process for destroying metastables. Indeed, Deloche and coworkers [108] used these superelastic reactions to express the overall destruction of the metastables due to electron collisions and they calculated in this way the reaction rate coefficients for these reactions.

For the reactions between heavy particles such as ions and neutral species a rate coefficient is used in the model, because these species are assumed to be thermal. The same applies to the electron-ion recombination reactions (no. 7-11), because such reactions occur with low-energy electrons. Based on the detailed report of Deloche and coworkers [108] dissociative  $\text{He}_2^+$  - electron recombination is included in the model as a three-body process, with either electrons or He atoms as a third body (reactions 8 and 9, respectively). However, we have repeated our calculations using a simple two-body dissociative recombination reaction, with a rate constant of  $10^{-14} \text{ m}^3 \text{ s}^{-1}$  [110] and this yielded the same results. Beside dissociative recombination, we have also included three-body non-dissociative electron -  $\text{He}_2^+$  recombination, giving rise to  $\text{He}_2^*$  dimers. The other reactions included in the model are between heavy particles and represent association, dissociation, associative or dissociative ionization and ion conversion.

The experimental conditions of the research on which we based our reaction rate coefficients are high pressure helium afterglow studies [108,109]. The afterglow causes the densities of the excited species to be low and hence the possibility arises that reactions induced by excited states are underestimated, as is also mentioned in these studies. Therefore we make use of the additional reactions 12 and 21, i.e., Hornbeck-Molnar associative ionization and He atom induced dissociation respectively, to account for this effect.

### 3.2.2 Setup and conditions

The model is applied to a dielectric barrier discharge, as described by Miclea and coworkers [44]. It consists of two flat glass plates, each with an aluminium electrode of 50 mm long. Both electrodes are covered by 20  $\mu\text{m}$  thick glass layers, i.e., the dielectric layers, as is schematically illustrated in Figure 3.2. The distance between the electrodes, including the dielectric layers, is 1 mm. A rectangular voltage pulse of 750 V (peak-to-peak) is applied at the powered electrode, with a rise-time of 2  $\mu\text{s}$ , whereas the other electrode is grounded. The frequency is typically in the order of 5-20 kHz, and we have used a value of 20 kHz. In the experiment, the average power was very low, between 0.5 and 1 W. Furthermore, it is reported that any kind of noble gas with pressures between 10 and 180 mbar can be ignited and sustained. As mentioned in section 3.2.1, we have applied the model to a He DBD. The gas temperature is chosen to be 300 K and the studied pressure range is 25 to 1100 mbar, because the pressure range in which a discharge could be obtained appeared

to be much larger in our calculations.

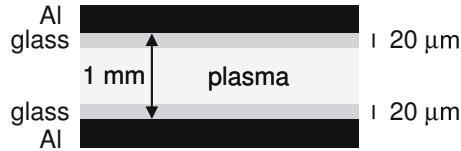


**Figure 3.2:** Schematic diagram of the setup.

The main idea is to obtain a better insight in the properties of this new discharge. For this purpose spatial profiles of the species densities and the electric potential are calculated for a pressure of 80 mbar. A second interest is to study the influence of the pressure on the possibility of stable discharge operation, on the electric current and on the densities of the active plasma species under the conditions of a dielectric barrier microdischarge.

The electrodes used in the experiments are 50 mm long and 800  $\mu\text{m}$  wide [44], which is long and narrow, as is also the discharge channel through which the plasma is transported. Such setup would require a three-dimensional approach to take into account all effects of the walls. This approach, however, would be very time consuming. Therefore a one-dimensional model was chosen, because such a model only uses the effects such as the gap width and the barrier thickness, which is very fast and makes it possible to study the pressure influence independently from the two and three-dimensional effects.

In the present simulations two different setups have been employed. For the calculations of the spatial variations in the discharge a cartesian geometry was chosen, because it is much closer related to the experimental geometry. In order to calculate the influence of the pressure a geometry was used that possesses axisymmetric symmetry consisting of 104 cells in the axial direction and three cells in the radial direction, so basically a one-dimensional model is used, which is computational less intensive than a two-dimensional model. For some test-cases more cells in the radial direction were implemented in order to check the effect of this simplification, but in the applied ranges no difference was observed.

The applied grid was equidistant in both radial and axial direction and the grid distance was 10  $\mu\text{m}$ . Of these 104 axial cells two on every end are electrodes of which one is grounded and on the other a voltage is applied. More to the middle, two cells on every end are dielectric and the remainder in between is discharge gas.

The experimentally used dielectrics are made of glass, therefore a dielectric constant of  $\epsilon_r = 6$  is used. Similar to Hagelaar and coworkers [111] for the atomic and molecular helium ions a secondary electron emission coefficient of 0.2 is used and the produced secondary electrons are assumed to have an initial energy of 5 eV.

As mentioned above the gas temperature in the model is assumed constant in time and space. Experimental data on the gas temperature in this He microdischarge were not directly available, therefore we used a gas temperature of 300 K. For the ignition of the dielectric barrier discharge a rectangular voltage pulse of 750 V peak-to-peak is used, together with a frequency of 5 kHz and a rise-time of  $2\mu\text{s}$ , as was reported by Kunze and coworkers [94].

## 3.3 Characterization of the discharge in time and space

### 3.3.1 Electrical characteristics

Figure 3.3 shows the applied voltage as a function of time (dashed line) for typical conditions of 80 mbar He pressure, 20 kHz and 750 V (peak-to-peak), as well as the calculated electrical current density (red line) and the calculated voltage drop over the discharge gap or gap voltage (black solid line). The latter arises as a result of the applied voltage in combination with the charging and discharging of the dielectrics. Indeed, the applied voltage causes a rise in the gap voltage until breakdown is reached, which appears to occur at a gap voltage of 230 V. A plasma is formed: the discharge gas ionizes and the charged particles migrate toward the electrode which bears an opposite charge. In this way charge accumulation occurs on the dielectric surface and the electric field in the discharge gap (or gap voltage) diminishes, since it is the sum of the field induced by the applied voltage and the opposite field created by the accumulated charges. This stabilizing effect makes DBDs so popular in producing controlled atmospheric pressure discharges, since it prevents the formation of an arc [30].

Figure 3.3a illustrates the periodic behavior of voltage and current over a long time period, whereas figure 3.3b focuses on one period, consisting of a positive and a negative voltage polarity, in order to visualize the detailed behavior of voltage and current. Note that some points are marked at the gap voltage profile. These are related to the discussion given below, with respect to figure 3.4. The applied voltage has an amplitude of 750 V peak-to-peak ( $V_{pp}$ ), the resulting gap voltage has an amplitude of  $460 V_{pp}$  during the applied voltage rise-time and it decreases to about  $40 V_{pp}$  during the plateau, before the powered electrode switches polarity. Note that it is the gap voltage, which determines the plasma characteristics. This is illustrated in the time-profile of the electric current density (red curve in figure 3.3). It exhibits a peak exactly at the peak of the gap voltage and drops to low values as soon as the applied voltage reaches its steady-state value. This typical electric current profile is also found in experiments and simulations of the more frequently

studied atmospheric pressure DBDs in helium [9, 8, 14].

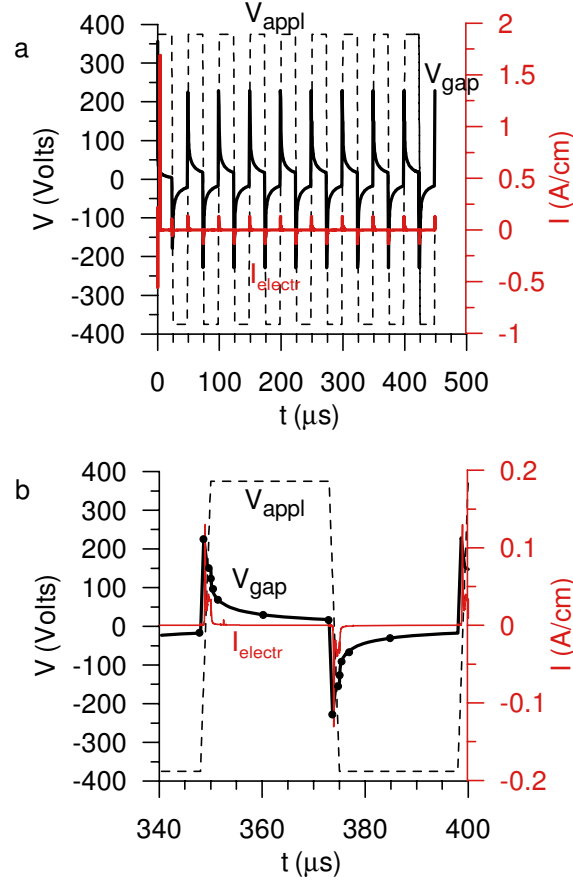


**Figure 3.3:** Potential applied to the electrodes ( $V_{appl}$ , black dashed line, left axis) and calculated electric current density (red line, right axis), as a function of time at 80 mbar, 20 kHz, and 750  $V_{pp}$ . The calculated voltage over the discharge gap (so-called gap voltage,  $V_{gap}$ ) is also plotted (black solid line, left axis), because this determines the plasma characteristics. (a) shows the temporal periodicity over a long time, whereas (b) is a magnification of one period, consisting of a positive and a negative voltage polarity. In (b) the solid circles on the gap voltage profile denote specific moments in time, related to figure 3.4.

Kunze and coworkers also measured the electric current in their DBD [94], although with argon as the discharge gas. They also observed a peak, although the latter was somewhat wider than in our calculations. The width depends on the electrical circuit properties, such as the capacity of the electrode configuration. Moreover, in the experiments there can always be some gas impurities present, but in the model at present a pure He discharge is assumed. More advanced chemical descriptions including impurities will be addressed later in this Ph.D thesis, because

it is recognized that also the presence of these impurities can lead to alterations in the electrical characteristics of the discharge [14,112]. Hence, exact comparison is not possible, but at least the characteristic behavior of rise and extinguishing of the electrical current, which is typical for DBDs, is found back in our calculation results.

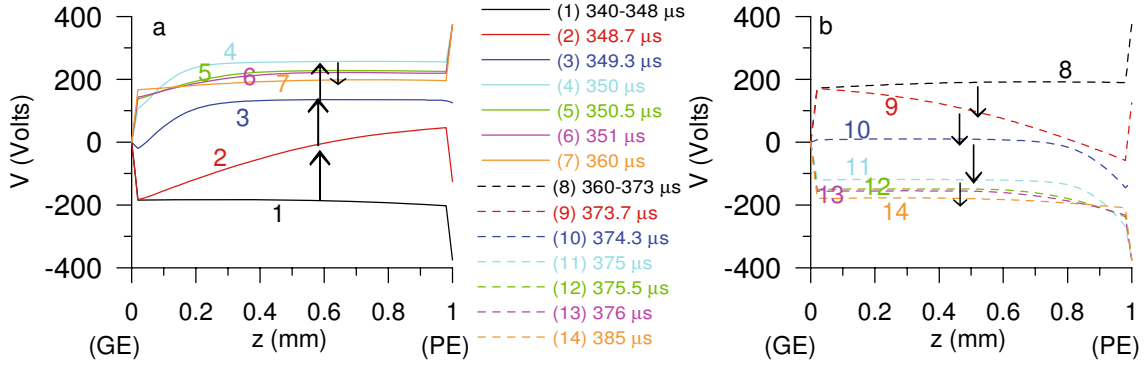


**Figure 3.4:** Calculated voltage drop or potential distribution between the electrodes at several moments in time (see legend), when the powered electrode is negative (a, solid lines) and positive (b, dashed lines) under the same discharge conditions as in figure 3.3. The arrows represent the time evolution of the potential distribution. The positions of grounded electrode (GE) and powered electrode (PE) are also indicated. Note that not only the potential distribution inside the plasma but also the potential drop across the dielectrics is depicted.

The voltage drop across the electrodes is depicted in figure 3.4 at several moments in time as indicated in the figure legend. Figure 3.4a (solid lines) illustrates the situation just before and during the positive applied voltage polarity, whereas figure 3.4b (dashed lines) refers to the situation when the applied voltage polarity is, or will soon become negative. These moments in time are also marked on the gap voltage profile of figure 3.3. The grounded and powered electrode (GE, PE) are situated at the left and right borders of figure 3.4, respectively. To explain the potential distribution inside the plasma based on the applied voltage, the voltage drop across both dielectrics is also included in the figure. Note that the electrodes are separated from each other by a distance of 1 mm, while both dielectrics have a thickness of  $20 \mu\text{m}$ , hence, the total discharge gap is  $960 \mu\text{m}$  or 0.96 mm.

From figure 3.4a it is clear that the potential distribution is constant in time from  $340 \mu\text{s}$  till  $348 \mu\text{s}$ , i.e., when the applied voltage is still negative. The grounded electrode on the left is at 0 V and the powered electrode on the right is at 375 V. However, this voltage drops almost completely in the dielectrics adjacent to the left and right electrodes. Indeed, the voltage drop over these two dielectrics is about -180 V (each), whereas the voltage drop over the plasma (the so-called gap voltage) is only about -20 V. This is also clear from the solid black line from figure 3.3b.

As soon as the applied voltage starts changing polarity, however, the potential distribution changes drastically. This is visualized by the red, blue and cyan curves in figure 3.4a. At 348.7  $\mu\text{s}$  (red curve), the applied voltage is only -125 V, but the voltage drops across both dielectrics are still about -180 V. Hence, the voltage drop, or better ‘rise’, across the discharge is now about +230 V. This value corresponds to the maximum value of the gap voltage reached as a function of time, as is also apparent from figure 3.3b. Consequently, at this moment also the electric current reaches its maximum, as can be seen in figure 3.3b.

After 349.3  $\mu\text{s}$  (blue line) the applied voltage is equal to +125 V, while the voltage drop across the electrodes is very small (about 10-20 V), due to the charging of the dielectrics. The surface charges on the dielectrics (not shown here) also switch polarity, albeit about a microsecond later than the applied voltage. Therefore, during the switching of the applied voltage and with a slight delay as to that voltage, a smaller voltage drop across the dielectrics is seen. Hence, the gap voltage at that time is about +150 V. At this moment the potential distribution inside the plasma resembles mostly that of a low pressure direct current glow discharge, where the potential is nearly constant and slightly above the potential of the most positive electrode (here at the right) in the largest part of the discharge, called the bulk plasma or negative glow. In front of the most negative electrode the potential exhibits a strong drop, characterizing the sheath or cathode dark space as is explained in Chapter 1 Section 1.3.

After 350  $\mu\text{s}$  (cyan curve), the potential distribution inside the plasma has the same shape as the one at 349.3  $\mu\text{s}$ , while the total gap voltage is again about +150 V. At this time the applied voltage has reached its steady positive polarity value of +375 V, therefore, the remaining voltage drop is now again found across both dielectrics (about 100-120 V each).

At later times, until 373  $\mu\text{s}$ , the applied voltage remains constant at +375 V. Meanwhile, the voltage drop across both dielectrics rises slightly, so that the gap voltage gradually decreases, as is clear from the green, pink and orange curves of figure 3.4a, as well as from the black curve in figure 3.3b. This situation corresponds also to the black dashed curve (representing 373  $\mu\text{s}$ ) of figure 3.4b.

After 373.7  $\mu\text{s}$ , however, the applied voltage starts to decrease again in order to change polarity. At this moment, there is still a large voltage drop across the dielectrics, so that the gap voltage reaches its maximum negative value of -230 V (red dashed curve). At 374.3  $\mu\text{s}$ , the applied voltage has become slightly negative (-125 V), the drop over the dielectrics is very small due to the charging of the dielectrics as a result of the large electrical current and the gap voltage has still a significant value of about -150 V (blue dashed line). At 375  $\mu\text{s}$  and later the applied voltage has reached its steady negative polarity of -375 V and the voltage drop across the dielectrics starts to increase again. As a consequence, the gap voltage amplitude

gradually starts to decrease again as a function of time, as is also seen in figure 3.3b.

Note that the orange dashed curve of figure 3.4b coincides more or less with the black solid curve of figure 3.4a, so that the cycle can be repeated when the applied voltage starts changing polarity again. Note also that the second half period (i.e., figure 3.4b) is more or less the mirror image of the first half period (i.e., figure 3.4a), because of the symmetrical electrode configuration. To summarize, the arrows in figure 3.4 visualize the time evolution of the potential distributions.

### 3.3.2 Plasma species densities

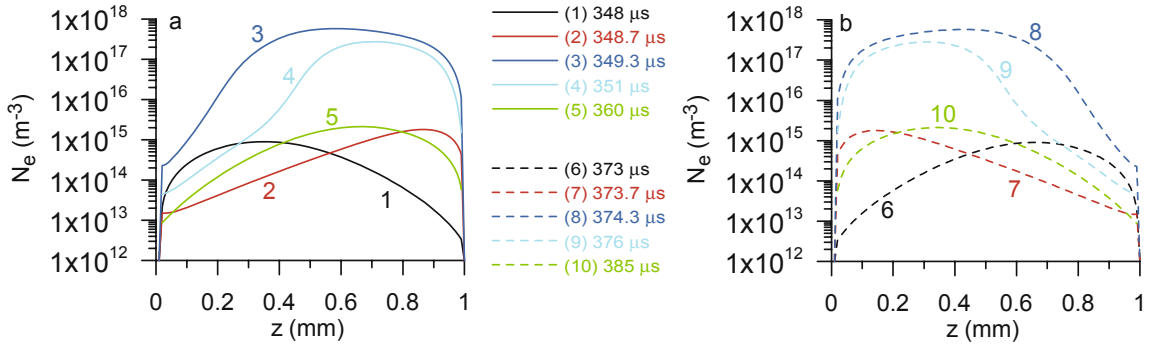


**Figure 3.5:** Calculated electron number density profiles inside the plasma at approximately the same moments in time as in figure 3.4 and under the same discharge conditions. Note the logarithmic scale of the y-axis, which was necessary to visualize all curves on one plot.

Figure 3.5 illustrates the number density profiles of the electrons at different times corresponding approximately to the same time-moments as in figure 3.4, and under the same discharge conditions as in figure 3.3. Note the logarithmic scale of this y-axis, which appeared necessary to fit all curves on one plot.

After 348  $\mu\text{s}$  (black solid line in figure 3.5a), i.e., just before the applied voltage changes polarity and the gap voltage and electrical current will start to rise, the electron density attains a value of a few times  $10^{14} \text{ m}^{-3}$ . The profile is asymmetric and reaches its highest value near the grounded electrode, which is the more positive electrode or anode at this time. (cf. figure 3.4a).

As soon as the applied voltage starts changing polarity, the electron density profile changes drastically. After 348.7  $\mu\text{s}$  (red solid curve in figure 3.5a) the absolute values of the electron density are still about the same, but the maximum shifts completely towards the other, powered, electrode. After 349.3  $\mu\text{s}$  (blue solid curve in figure 3.5a) the electron density has increased dramatically by almost three orders of magnitude to values of a few times  $10^{17} \text{ m}^{-3}$  and the maximum is more spread

over the entire discharge gap.

After this time, the electron density starts to decay again, as is visualized by the cyan and green solid curves of figure 3.5a and the profile becomes again more asymmetric, with its maximum near the powered electrode on the right. The density profile shown after 361  $\mu\text{s}$  (green solid curve in figure 3.5a) is more or less retained until 373  $\mu\text{s}$ , symbolized by the black dashed curve of figure 3.5b.

After 373.7  $\mu\text{s}$ , the applied voltage starts changing polarity and the electron density again changes drastically, with first a shift towards the other, grounded, electrode (red dashed line of figure 3.5b), followed by a dramatic increase and spreading of the maximum over the entire gap at 374.3  $\mu\text{s}$  (blue dashed curve). Then again decrease in electron density occurs and at even later times more asymmetric profiles are formed (cyan and green dashed curves). The green dashed curve of figure 3.5b again coincides more or less with the black solid curve of figure 3.5a, illustrating that the cycle is repeated when the applied voltage switches polarity again.

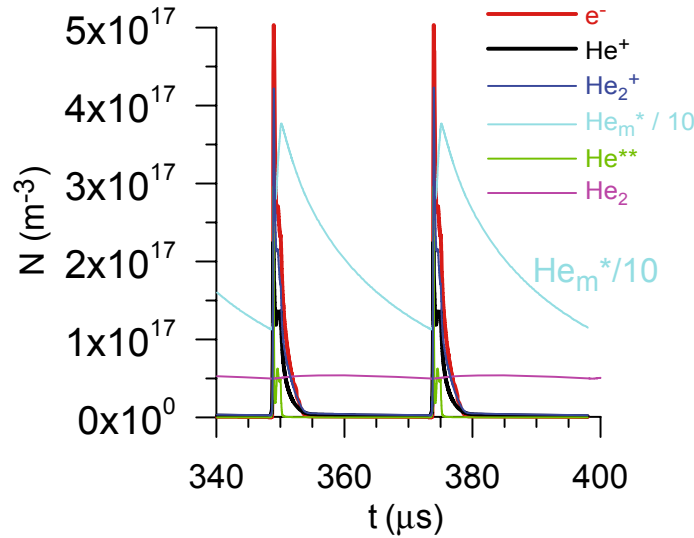


**Figure 3.6:** Calculated spatially averaged number densities of the different plasma species as a function of time, under the same conditions as in figure 3.3. Note that the  $\text{He}_m^*$  density was divided by 10, to enable its inclusion in the same figure as the other curves.

The spatially averaged electron density is plotted as a function of time in figure 3.7 (red curve), along with the spatially averaged densities of the other plasma species, for the same operating conditions as in the previous figures. As was already illustrated in figure 3.5, the electron density rises sharply at 349  $\mu\text{s}$ , when the applied voltage is switching polarity and the electrical current reaches its maximum. After this (spatially averaged) maximum value of  $5 \times 10^{17} \text{ m}^{-3}$  is attained, the density

decays rapidly to values in the order of  $10^{15} \text{ m}^{-3}$  in about  $5 \mu\text{s}$  and then more slowly to values in the order of  $10^{14} \text{ m}^{-3}$ , before it starts to rise again when the applied voltage switches polarity.

The spatially averaged densities of the  $\text{He}^+$  and  $\text{He}_2^+$  ions (black and blue curves, respectively) exhibit the same time profile as the electron density. Their (spatially averaged) maximum values are calculated to be  $2.3 \times 10^{17}$  and  $4.2 \times 10^{17} \text{ m}^{-3}$ , respectively.

The neutral plasma species have different time profiles. The He metastable ( $\text{He}_m^*$ ) density (cyan curve; 10 times reduced to fit in the same plot) also increases sharply when the electron density reaches its maximum, but it decays very slowly before it starts rising again when the voltage switches polarity. The (spatially averaged) maximum is about  $3.7 \times 10^{18} \text{ m}^{-3}$ , and the minimum value is still above  $10^{18} \text{ m}^{-3}$ . This slow decay illustrates that the metastables have a longer lifetime than the charged plasma species. Note that the density of these  $\text{He}_m^*$  atoms is about an order of magnitude higher than the densities of the other plasma species. However, their density is still about six orders of magnitude lower than the He ground state atom density, which is approximately  $10^{24} \text{ m}^{-3}$  under the conditions studied.

The He atoms excited to higher levels ( $\text{He}^{**}$ ; green curve), on the other hand, are characterized by a much faster drop and moreover, they have a very low density, with a spatially averaged maximum of only  $5 \times 10^{16} \text{ m}^{-3}$ . Hence, they are clearly less important in the plasma than the  $\text{He}_m^*$  metastable atoms.

Finally, the  $\text{He}_2^*$  dimers (pink curve) are characterized by a nearly constant density ( $\sim 5 \times 10^{16} \text{ m}^{-3}$ ) throughout time, hence, almost not affected by the applied voltage polarity switches. Their density is the lowest of all plasma species included. They can, however, become more important when the gas pressure increases, as is commonly the case for He DBDs used for technological applications [9, 109] and as will be illustrated in Section 3.4.

Figure 3.7 illustrates the spatial density profiles of the plasma species plotted at  $349 \mu\text{s}$ , which is the moment in time when they reach their maximum density. The charged species are represented by solid lines, whereas the neutral species are symbolized by dashed lines. The electron density (red solid line) exhibits a typical profile, which is also more or less characteristic for a low pressure dc glow discharge between conducting electrodes, with low values in the sheath near the cathode and much higher values in the bulk plasma. Note that this density profile is obtained at  $349 \mu\text{s}$ , when the potential distribution was indeed found to resemble that of a dc glow discharge (blue line of figure 3.4a). At other moments in time the potential distribution and hence the electron density profile (see figure 3.5) behave differently.

The  $\text{He}^+$  and  $\text{He}_2^+$  ion densities (black and blue curves, respectively) also reach a maximum in the so-called bulk plasma, where the electrons reach their maximum density. They are also characterized by a second maximum in the sheath near the cathode, which is at this moment in time the grounded electrode. For the  $\text{He}^+$  ions,

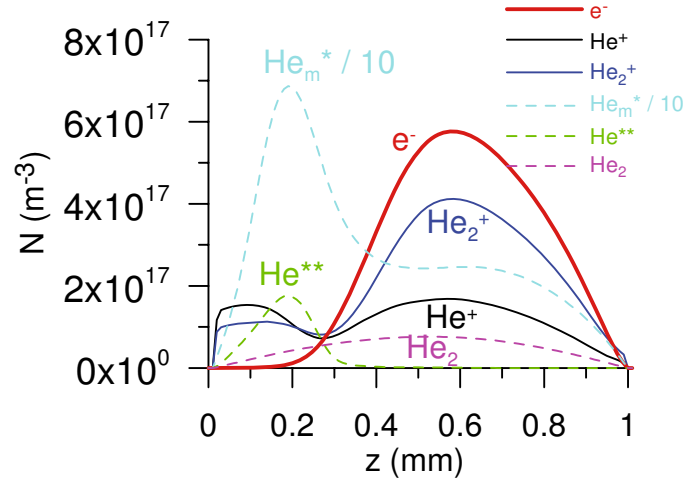


**Figure 3.7:** Calculated number density profiles of the different plasma species at the peak of their temporal evolution (i.e., at  $349 \mu\text{s}$ ) for the same discharge conditions as in figure 3.3. The charged particles are represented with solid lines whereas the dashed curves stand for the neutral species. Note that the  $\text{He}_m^*$  density was divided by 10, to enable its inclusion in the same figure as the other curves.

this maximum is even slightly higher than the maximum in the bulk plasma. This illustrates that the plasma only resembles a dc glow discharge, but is still different. Moreover, at the other times there is a clear distinction with the behavior of a dc glow discharge (see figures 3.4 and 3.5).

The  $\text{He}_m^*$  and  $\text{He}^{**}$  density profiles (cyan and green dashed lines, respectively) also reach a maximum in the sheath, because they are predominantly formed by electron induced excitation, as will be explained later. This process is mainly important in this region, as here the electrons can gain sufficient energy from the electric field. Note that the  $\text{He}_m^*$  density profile is reduced by a factor of 10 to fit in the same figure. Hence, the density of  $\text{He}_m^*$  excited atoms ( $\sim 7 \times 10^{18} \text{ m}^{-3}$  at the maximum of its profile) is a factor of 40 higher than the  $\text{He}^{**}$  density ( $\sim 1.8 \times 10^{17} \text{ m}^{-3}$ ).

The density of the  $\text{He}_2^*$  dimers is with a value of approximately  $7.6 \times 10^{16} \text{ m}^{-3}$  still lower, but they are more uniformly distributed throughout the discharge gap (pink curve).

### 3.3.3 Importance of the chemical production and loss processes

The characteristic temporal and spatial density profiles of the various plasma species can be explained when looking at their production and loss mechanisms. It

was found that all the direct electron induced processes (i.e., the electron induced reactions (1-6 from Table 3.1), but also electron-ion recombination; reactions 7-11 from Table 3.1), as well as Hornbeck-Molnar associative ionization (reaction 12) and ion conversion (reaction 15) exhibit a strong and narrow peak at about 349  $\mu$ s. The  $\text{He}_m^*$  metastable induced reactions (13, 14, 16-18 from Table 3.1), on the other hand, are characterized by a strong rise at 349  $\mu$ s, but a slow decay similar to the  $\text{He}_m^*$  density behavior (see figure 3.6). Finally, the  $\text{He}_2^*$  dimer induced reactions (19-21 from Table 3.1) appear to be nearly time-independent, which corresponds to the  $\text{He}_2^*$  density behavior.

The calculated relative contributions of the different production and loss processes for the various species, obtained both at their peak density (349 s) and during the plateau of the gap voltage (at 360 s) are summarized in Table 3.2. The results for the peak and plateau of the opposite polarity are not given, because they were found to be exactly the same.

The relative contributions of the chemical reactions to the total production and destruction rate of every particle is calculated using

$$\alpha_{i,j} = \frac{c_{i,j}R_{i,j}}{\sum_k c_{i,k}R_{i,k}} \quad (3.1)$$

where  $\alpha_{i,j}$  is the relative contribution of reaction  $j$  to the total production or destruction of particle  $i$  and  $R_{i,j}$  is the spatially averaged reaction rate of reaction  $j$  that influences the density of species  $i$  and is defined by

$$R_{i,j} = k_j \prod_p n_p \quad (3.2)$$

where  $k_j$  is the reaction rate coefficient and  $n_p$  the density of a reacting species. The coefficient  $c_{i,j}$  in equation 3.1 is the associated stoichiometric number that accounts for the amount of species  $i$  that are lost or created in reaction  $j$ .

The electrons are primarily formed at the peak of their density from He ground state atoms by electron induced ionization, and by Hornbeck-Molnar associative ionization, whereas metastable-metastable (associative and normal) ionization are the most important production mechanisms during the plateau. Indeed, by that time the electron density has already dropped to low values, whereas the density of the  $\text{He}_m^*$  metastable atoms is still substantial (see figure 3.5). As far as the loss of electrons is concerned, recombination with  $\text{He}^+$  ions and dissociative recombination with  $\text{He}_2^+$  ions appear to be nearly equally important processes at the peak. During the plateau, both dissociative and normal recombination with  $\text{He}_2^+$  ions were calculated to be the main loss mechanisms, but with He atoms as third body, because the electron density has dropped to low values, making these species less important as a third body.

The  $\text{He}^+$  ions are mainly created from the He ground state by electron induced ionization at the peak, and by metastable-metastable ionization during the plateau. They are predominantly lost by electron-ion recombination.  $\text{He}^+$  to  $\text{He}_2^+$  ion conversion seems to be of minor importance, especially during the plateau.

Hornbeck-Molnar associative ionization was found to be the dominant production mechanism for the  $\text{He}_2^+$  ions at the peak, whereas during the plateau time metastable-metastable ionization was most important. This is as expected, because the  $\text{He}_m^*$  metastables are characterized by a much longer lifetime than the highly excited  $\text{He}^{**}$  atoms. Loss of  $\text{He}_2^+$  ions occurs mostly by dissociative recombination at the peak and by dissociative or normal recombination, but with He atoms as a third body during the plateau time, in analogy to the loss mechanisms for the electrons.

The  $\text{He}_m^*$  atoms are almost exclusively populated by electron induced excitation, both at the peak and during the plateau. The dominant loss mechanism of these species is electron induced ionization at the peak, and metastable-metastable (associative or normal) ionization during the plateau. This is again as expected, because the electron density is much higher and can more easily give rise to electron-induced processes at the peak, whereas the density of the metastables is still substantial during the plateau.

The  $\text{He}^{**}$  atoms are only formed by electron induced excitation and are destroyed by Hornbeck-Molnar associative ionization, both at the peak and during the plateau, because these are the only production and loss mechanisms included in the model for these species. Note that this is an approximation, because in reality radiative decay will also be responsible for the loss of the  $\text{He}^{**}$  atoms. However, in order to describe this in an accurate way, various  $\text{He}^{**}$  atomic levels would have to be considered separately in a kind of collisional-radiative model [113] and this is beyond the scope of this study. The density of the  $\text{He}^{**}$  atoms would, in any case, be much less than, for example, the  $\text{He}_m^*$  density, so they would not be very important under the present conditions.

Finally, the  $\text{He}_2^*$  dimers are predominantly produced by metastable induced association. At the peak of the densities, however,  $\text{He}_2^+$  ion - electron recombination is also important, especially with He atoms as a third body. Loss of the  $\text{He}_2^*$  dimers occurs mainly by metastable induced (dissociative) ionization and to a lesser extent by He atom induced dissociation. Electron induced dissociation appears to be important only at the peak of its density, which is again as expected, because of the rapid decay of electrons as a function of time.

**Table 3.2:** Calculated relative contributions of the different production and loss processes for each of the different plasma species, both at the peak (i.e., 349  $\mu\text{s}$ ) and during the plateau time (i.e., 360  $\mu\text{s}$ ) at the same discharge conditions as indicated in figure 3.3. The numbers between brackets in the first column correspond to the numbers of the reactions listed in Table 3.1.

Process	Relative contribution (%)	
	At peak (349 $\mu\text{s}$ )	During plateau (360 $\mu\text{s}$ )
Production of electrons		
(3) Electron induced ionization from He ground state	39.3	0.1
(4) Electron induced ionization from metastables	2.5	2.2
(12) Hornbeck-Molnar associative ionization	58.2	1.64
(13) Metastable-metastable associative ionization	0.07	65.7
(14) Metastable-metastable ionization	0.03	28.1
(17) Metastable induced dissociative ionization of $\text{He}_2^*$	$\sim 0$	0.4
(18) Metastable induced ionization of $\text{He}_2^*$	0.002	1.8
(19) Dimer induced dissociative ionization of $\text{He}_2^*$	$\sim 0$	0.008
(20) Dimer induced ionization of $\text{He}_2^*$	$\sim 0$	0.03
Loss of electrons		
(7) $\text{He}^+$ ion-electron recombination	44.7	0.6
(8) $\text{He}_2^+$ dissociative recombination with e- as third body	35.8	0.5
(9) $\text{He}_2^+$ dissociative recombination with He as third body	12.6	69.3
(10) $\text{He}_2^+$ recombination with e- as third body	1.5	0.02
(11) $\text{He}_2^+$ recombination with He as third body	5.4	29.6
Production of $\text{He}^+$ ions		
(3) Electron induced ionization from He ground state	94	6.9
(4) Electron induced ionization from metastables	5.9	0.3
(14) Metastable-metastable ionization	0.07	91.3
(17) Metastable induced dissociative ionization of $\text{He}_2^*$	$\sim 0$	1.5
(19) Dimer induced dissociative ionization of $\text{He}_2^*$	$\sim 0$	0.03
Loss of $\text{He}^+$ ions		
(7) Ion-electron recombination	94	$\sim 100$
(15) $\text{He}^+$ to $\text{He}_2^+$ ion conversion	6	$\sim 0$
Production of $\text{He}_2^+$ ions		
(12) Hornbeck-Molnar associative ionization	99.3	2.2
(13) Metastable-metastable associative ionization	0.1	88.8
(15) $\text{He}^+$ to $\text{He}_2^+$ ion conversion	0.6	6.5
(18) Metastable induced ionization of $\text{He}_2^*$	0.003	2.4
(20) Dimer induced ionization of $\text{He}_2^*$	0.004	0.04
Loss of $\text{He}_2^+$ ions		
(8) Dissociative recombination with $\text{e}^-$ as third body	64.7	0.5
(9) Dissociative recombination with He as third body	22.7	69.7
(10) Ion-electron recombination with $\text{e}^-$ as third body	2.8	0.02
(11) Ion-electron recombination with He as third body	9.8	29.8

Process	Relative contribution (%)	
	At peak (349 $\mu$ s)	During plateau (360 $\mu$ s)
Production of He <sub>m</sub> <sup>*</sup> metastable atoms		
(1) Electron induced excitation	99.9	~ 100
(7) He <sup>+</sup> - electron recombination	0.03	~ 0
(8) He <sub>2</sub> <sup>+</sup> - electron dissociative recombination with e <sup>-</sup> as third body	0.02	~ 0
(9) He <sub>2</sub> <sup>+</sup> - electron dissociative recombination with He as third body	0.008	0.002
Loss of He <sub>m</sub> <sup>*</sup> metastable atoms		
(4) Electron induced ionization	94.9	2.0
(5) Electron induced de-excitation	0.7	9.2
(13) Metastable-metastable associative ionization	2.7	60.7
(14) Metastable-metastable ionization	1.2	26.0
(16) Metastable induced association	0.4	9.2
(17) Metastable induced dissociative ionization of He <sub>2</sub> <sup>*</sup>	0.02	0.4
(18) Metastable induced ionization of He <sub>2</sub> <sup>*</sup>	0.06	1.7
Production of He <sup>**</sup> atoms		
(2) Electron induced excitation	100	100
Loss of He <sup>**</sup> atoms		
(12) Hornbeck-Molnar associative ionization	100	100
Production of He <sub>2</sub> <sup>*</sup> dimers		
(10) He <sub>2</sub> <sup>+</sup> ion-electron recombination with e <sup>-</sup> as third body	5.9	~ 0
(11) He <sub>2</sub> <sup>+</sup> ion-electron recombination with He as third body	20.9	~ 0
(16) Metastable induced association	73.2	~ 100
Loss of He <sub>2</sub> <sup>*</sup> dimers		
(6) Electron induced dissociation	19.4	0.06
(17) Metastable induced dissociative ionization	13.6	16.9
(18) Metastable induced ionization	54.7	67.7
(19) Dimer induced dissociative ionization	0.2	0.3
(20) Dimer induced ionization	0.9	1.1
(21) He atom induced dissociation	11.3	13.9

## 3.4 Influence of the pressure on the discharge

The second interest of this research is to clarify the influence of the operating pressure on discharge characteristics such as the electric current, species densities and the identification of the governing processes occurring in this kind of configuration. Since the electric properties of the DBD are very characteristic and the amplitudes and widths of the current peaks tell us a lot about the discharge, these will be the first to be discussed.

### 3.4.1 Influence on the electrical characteristics

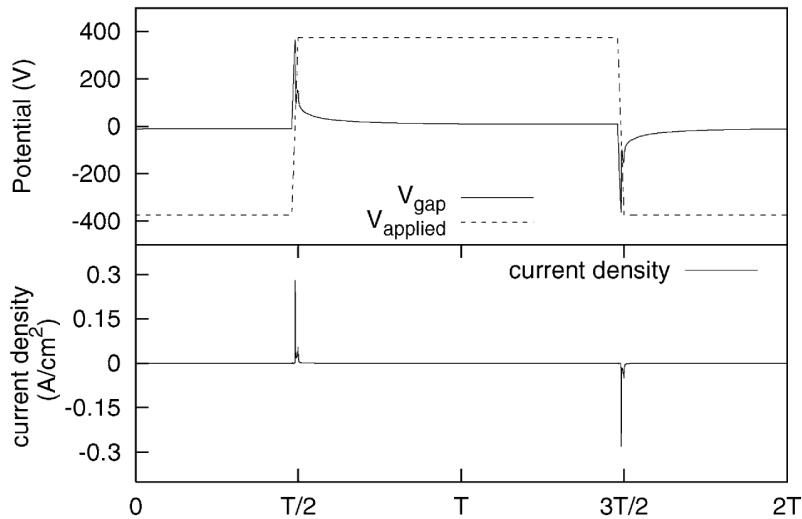


**Figure 3.8:** Voltage applied to the electrodes (top frame, dotted line) and potential difference between the surfaces of the dielectrics, also called gap voltage (top frame, solid line). The current density peak shown in the bottom frame, always occurs right after the maximum in gap voltage. This profile is taken for a pressure of 87 mbar and the current density peaks have an amplitude of  $0.28 \text{ A/cm}^2$ .

Figure 3.8 shows the calculated electrical characteristics of the helium DBD operated at 87 mbar. The parameter  $T$  on the bottom axis is the duration in time of half a period, hence  $2T$  is one period. In the top frame the rectangular applied voltage is shown together with the potential difference across the discharge gap or so-called gap voltage. The latter is determined both by the potentials applied to the electrodes and by the charging effects which occur on the dielectrics as was explained in Section 3.3. In the bottom frame the calculated current density is shown. The graph shows that the helium discharge event occurs once every half period when the gap voltage has reached a value of about 360 V and it causes a maximum

current density of  $280 \text{ mA/cm}^2$ . This rather high value is due to the overvoltage in the gap-voltage that occurs in the simulation. It was explained by Boeuf [114] that even a small overvoltage in a dielectric barrier discharge in He can cause the electric current densities to become 100 times larger than in the situation where the breakdown voltage is only just reached. The breakdown voltage of He at this pressure and discharge gap is about  $220 \text{ V}$  [13]. The gap voltage that can be seen in figure 3.8 is  $364 \text{ V}$ . This means that there is a significant overvoltage. In the case of sinusoidal applied voltages such an overvoltage leads to a multipeak discharge as in [115,31]. In the case of a rectangular voltage, the voltage rise is too fast for multiple discharges to be formed and the amplitude of the current peak rises significantly.

The value of  $87 \text{ mbar}$  has been chosen, because it lies right in between the values of  $10$  and  $180 \text{ mbar}$  of which it was reported by Miclea and coworkers [44] that “any kind of noble gas with a pressure value in that range can be ignited and sustained in this kind of experimental configuration”. In the present study concerning the influence of the pressure we have simulated far beyond this range. With the present model we were able to simulate periodic plasma behavior within the range of  $15$  to  $1113 \text{ mbar}$  in helium. The origins of these pressure limits will be discussed in Section 3.4.3. Outside this range the model was not able to sustain a large enough amount of charge carriers and therefore no periodic steady state was reached. The presented results are taken within a safe range of  $25$  to  $1100 \text{ mbar}$  to avoid the influences of possible instabilities due to pressure.

The obtained results at different pressures did not always show symmetric behavior regarding both halves of the period. In figure 3.9 the top frame illustrates the peak values of the parameters  $J_+$  and  $J_-$  which are the positive and negative current density peaks, respectively. For all pressures investigated the current density profiles were similar to figure 3.8 of the  $87 \text{ mbar}$  discharge, with of a single narrow current peak every half period. Differences in the profiles are only seen in the peak amplitudes and in the symmetry of the peaks. Therefore, the ratio of the positive to the negative peak values is shown in the bottom frame of figure 3.9.

For most of the pressures investigated, a discharge symmetric in time has been predicted with the model. At  $25$  and  $37 \text{ mbar}$ , however, an asymmetric discharge has been obtained of which the negative discharge pulse is stronger than the positive. Moreover, on the other hand at pressures from  $100$  to  $140 \text{ mbar}$  the negative peak was found to be lower than the positive peak. The reason for this asymmetry is not clear, but is probably due to the spatial differences in the reaction rates.

It is interesting to remark that the current density in the helium plasma seems to be considerably higher in the region from  $50$  to  $140 \text{ mbar}$ , which is similar to the typical operating pressures from  $10$  to  $180 \text{ mbar}$  reported in [44]. This higher current density is, as will be shown later in Section 3.4.2, associated with significantly higher charged particle densities, which indicates that the plasma may possess increased dissociative capabilities, or plasma ‘activity’. The reason for this activity

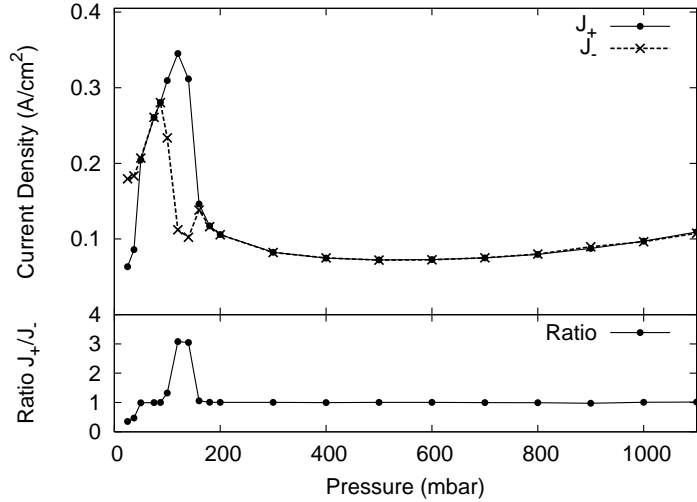


**Figure 3.9:** Influence of the pressure on the discharge current density. In the top frame the absolute values of the positive and negative current peaks ( $J_+$  and  $J_-$ , respectively) are plotted at different pressures. In the bottom frame the absolute value of the ratio of the positive to the negative current peak is shown. There is clearly a higher current density in the region from 50 to 140 mbar, where also the positive current peak seems to be significantly higher than the negative one.

will be discussed further in Section 3.4.2. This result is interesting for the use of this plasma in diode laser atomic absorption spectrometry, as is suggested by Miclea and coworkers [44], since the purpose of the plasma is the dissociation of molecules and excitation of atoms, which are processes that are determined by the plasma activity.

In order to obtain an idea of the plasma regimes that are reached in the high current and low current density zone, a comparison of the spatial potential distribution and the densities of the charged particles is made in figure 3.10 for two distinct pressures of 120 mbar and 500 mbar. These pressures are chosen as such, because 120 mbar is the pressure with the highest current density and 500 mbar is the pressure above 120 mbar with the lowest current density, as can be seen in figure 3.9. The positive ion density distributions shown in figure 3.10 are of course the sum of the densities of  $\text{He}^+$  and  $\text{He}_2^+$ . These spatial distributions are taken at the moment immediately after the positive current peak, because the potential distribution needs a fraction of time (about  $0.25 \mu\text{s}$  in the model) to adapt itself to the newly formed charges (see Section 3.3.1).

These spatial profiles are typical for dielectric barrier discharges as can be seen from the work of F Massines and coworkers [14,17], where the density profiles of the charged particles in the vicinity of the dielectric are even more narrow because of the atmospheric pressure. The reason that the electron density in the 500 mbar case

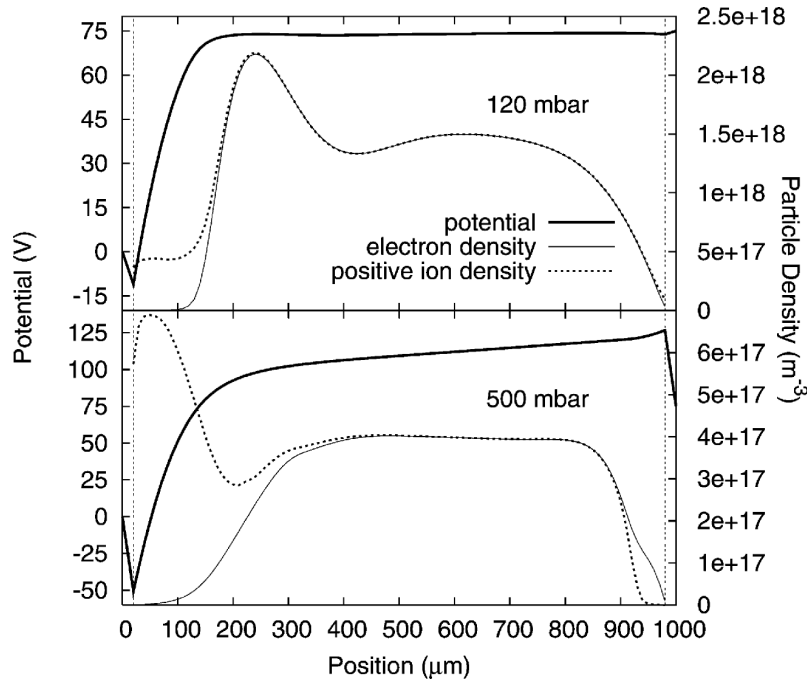


**Figure 3.10:** Calculated spatial distributions of the potential, the electron density and the sum of positive ion densities for two distinct cases of 120 mbar and 500 mbar. The grounded electrode is at the left hand side and the powered electrode at the right, which is currently at a positive potential. From 0 to 20  $\mu\text{m}$  and from 980 to 1000  $\mu\text{m}$  there is no discharge gas, since the space is filled with dielectric. Hence, the species densities in those regions are zero. The vertical dotted lines denote the border between plasma and dielectrics.

is not as high in the vicinity of the dielectric as in the 120 mbar case, lies in the very fast profile variation at maximum current in this kind of configuration, as explained in Section 3.3.1. Indeed, the electron profile in the 500 mbar case has already moved slightly away from the dielectric.

Important observable features are the positive charges near the grounded (i.e., most negative) electrode, where the densities are large enough to form a sheath, and the quasi-neutrality in the center of the plasma, which forms a plasma-bulk. In the 500 mbar profile there is also a small excess of electrons near the powered (i.e., most positive) electrode which causes a small rise in the potential profile, which is not observed in the 120 mbar case. These sheath and bulk formations, even with the possibility of a small electron excess near the powered electrode, are typical characteristics of the glow discharge regime, as explained in Chapter 1 Section 1.3.1.

In figure 3.10 there is also a very interesting difference in the densities of the charged particles. The densities in the plasma at 120 mbar are about 3 to 3.5 times as large as in the 500 mbar plasma. This was to be expected, since it can be seen in

figure 3.9 that the current density at 120 mbar is also about 3.5 times larger than the current density in the 500 mbar plasma.

The behavior of the neutral particles, which are not so closely related to the electrical plasma properties, will be discussed in the next section.

### 3.4.2 Influence on the species densities

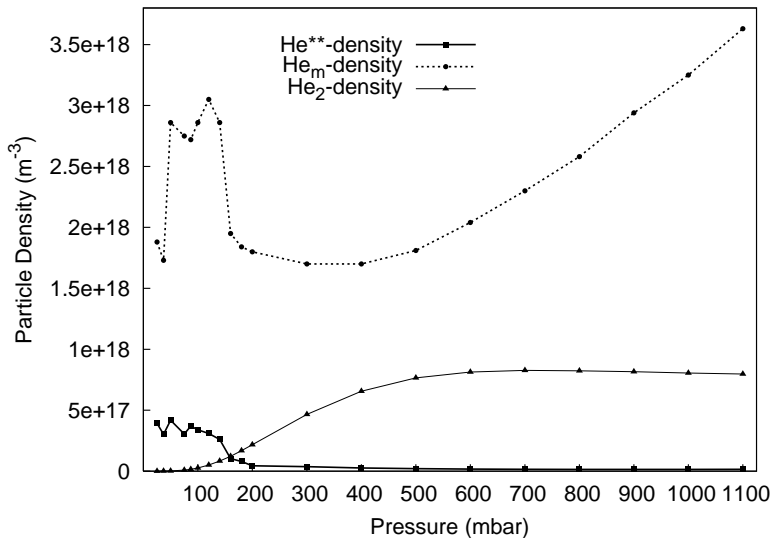


**Figure 3.11:** Calculated spatially averaged neutral species densities at the maximum positive current for pressures ranging from 25 to 1100 mbar.

The densities of the charged particles are determining for the plasma characteristics, but since in spectroscopic applications dissociation and excitation are the key elements one also has to study the behavior of the excited species present in the plasma. In figure 3.11 the spatially averaged densities of  $\text{He}_m^*$ ,  $\text{He}^{**}$  and  $\text{He}_2^*$  at the maximum of positive current are plotted as a function of pressure. The pressures range from 25 to 1100 mbar.  $\text{He}_m^*$  is clearly the most important in the entire range with values ranging from  $1.7 \times 10^{18} \text{ m}^{-3}$  to  $3.63 \times 10^{18} \text{ m}^{-3}$ , at pressures of 300 mbar and 1100 mbar respectively. This is rather high in comparison to  $\text{He}^{**}$ , of which the densities range from  $1.41 \times 10^{16} \text{ m}^{-3}$  to  $4.18 \times 10^{17} \text{ m}^{-3}$ , and  $\text{He}_2^*$  which is characterized by densities ranging from  $2.57 \times 10^{14} \text{ m}^{-3}$  to  $8.27 \times 10^{17} \text{ m}^{-3}$ .

In figure 3.12 the spatially averaged densities of the charged particles are shown for the same pressure range as in figure 3.11. In this figure it is seen that  $\text{He}_2^+$  is the most important positive ion in the entire pressure range. Only in the region from

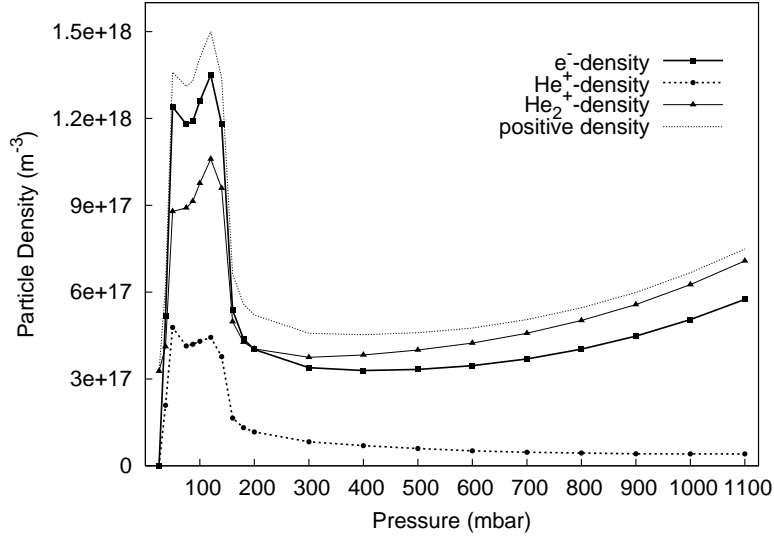


**Figure 3.12:** Calculated spatially averaged charged particle densities at the maximum positive current for different pressures.

50 to 140 mbar, where the plasma activity seems to be higher, there is about 30% contribution of  $\text{He}^+$  to the total positive charge density. Outside of this region  $\text{He}_2^+$  almost completely dominates the positive charge.

Figure 3.11 and figure 3.12 show that all plasma species, except for  $\text{He}_2^*$ , exhibit a significantly higher density in the range from 50 to 140 mbar. It is remarkable how the increase of the pressure has a different effect on different species:  $\text{He}_m^*$  exhibits the most spectacular rise in density as a function of pressure. The  $\text{He}_2^+$  and the electron densities also show a rise, but it is less steep. The  $\text{He}^+$  and the  $\text{He}^{**}$  densities appear to decrease as a function of pressure and the  $\text{He}_2^*$  densities become independent of He pressure above *ca.* 500 mbar. In the following we will study this behavior in more detail to identify the governing processes in the discharge. For this purpose, we calculated the relative contributions of the chemical reactions to the total production and destruction rate of every species. Subsequently, these relative contributions will be compared with the absolute reaction rates. Hence, a thorough insight in the underlying chemical mechanisms can be obtained.

### $\text{He}_m^*$

For every pressure it is calculated that the relative contribution of electron induced excitation from ground state helium (reaction 1) to the total production of  $\text{He}_m^*$  is more than 93%. Therefore the production of  $\text{He}_m^*$  is almost completely governed

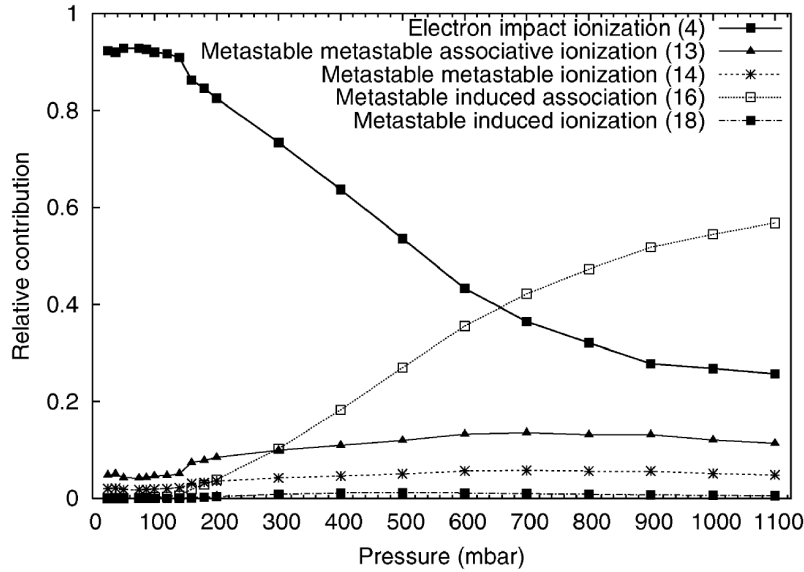


**Figure 3.13:** Calculated relative contributions of the chemical reactions leading to the destruction of  $\text{He}_m^*$  at the maximum positive current, as a function of pressure. The numbers between brackets correspond to the numbers in the first column of Table 3.1

by this reaction. The relative contributions of the different reactions leading to the destruction of He are presented in figure 3.13. This figure clearly shows that at pressures below 650 mbar the electron induced ionization (reaction 4) is the most important reaction in the destruction of  $\text{He}_m^*$ . At pressures above 650 mbar metastable induced association (reaction 16) becomes the dominating reaction. Indeed, this reaction occurs with 2 He atoms, so it is straightforward that the rate increases with the He pressure. The other destruction processes are of minor importance in the entire pressure range investigated.

The study of the relative contributions can only tell *which* process is important and not *how* important it is. In order to obtain information on the absolute importance of a reaction, also the absolute reaction rates need to be studied. Therefore, we present in figure 3.14 the absolute reaction rates of the most important reactions in the discharge. The electron induced excitation (reaction 1), which completely governs the production of  $\text{He}_m^*$ , appears to be one of the two most important reaction mechanisms in the discharge. Figure 3.14 shows that for pressures above 160 mbar the electron induced excitation (reaction 1), is the most important reaction and that for pressures below 160 mbar this reaction is the second most important, after the Hornbeck-Molnar associative ionization (reaction 12).

The electron induced ionization (reaction 4) and the metastable induced association (reaction 16) do not attain values higher than  $5 \times 10^{17} \text{ cm}^{-3}\text{s}^{-1}$ . This is much lower than the electron induced excitation rates (reaction 1), as can be seen

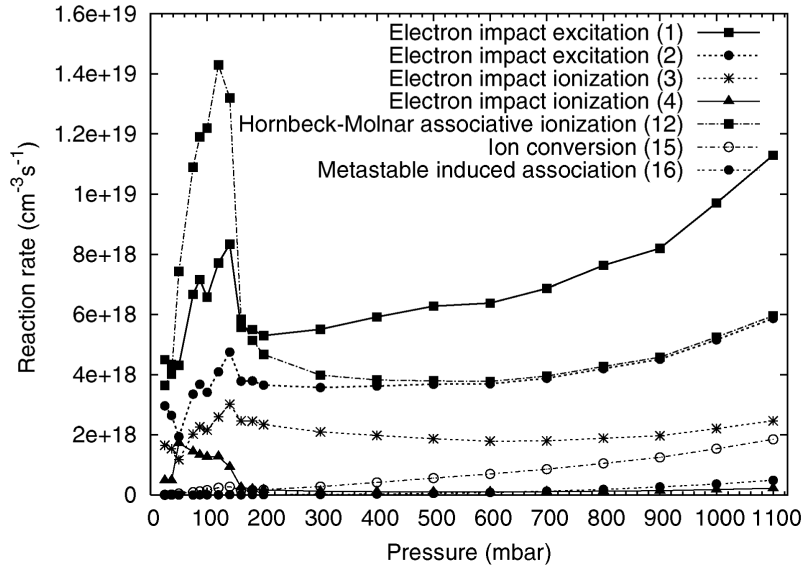


**Figure 3.14:** Calculated spatially averaged reaction rates of the seven most important reactions in the plasma at the maximum positive current for different pressures.

in figure 3.14. Therefore the two important  $\text{He}_m^*$  destruction reactions are negligible in comparison with the  $\text{He}_m^*$  production reaction. In Table 3.1 it can be seen that the electron induced excitation reaction is directly dependent on the He background gas pressure. This causes the rate of this reaction to steeply rise as a function of pressure, as can be seen in figure 3.14. It also explains the same steep rise of the  $\text{He}_m^*$  densities in figure 3.11, since the  $\text{He}_m^*$  densities are completely governed by the electron induced excitation (reaction 1).

In figure 3.14 it can also be observed that in the region from 50 to 140 mbar the Hornbeck-Molnar associative ionization (reaction 12) is clearly the dominant process in the discharge. This reaction boosts up the production of the  $\text{He}_2^+$  ions and the electrons. Subsequently, the newly created electrons will produce  $\text{He}_m^*$  excited states through electron induced excitation (reaction 1). This explains the higher  $\text{He}_m^*$  density in the region from 50 to 140 mbar which can be seen in figure 3.11. The Hornbeck-Molnar associative ionization (reaction 12) appears to be responsible for the higher plasma activity in the range from 50 to 140 mbar.

## Electrons

In figure 3.15 the relative contributions of the chemical reactions leading to the production (top frame) and loss (bottom frame) of the electrons are presented at maximum current for different pressures. In the top frame of figure 3.15 it can be

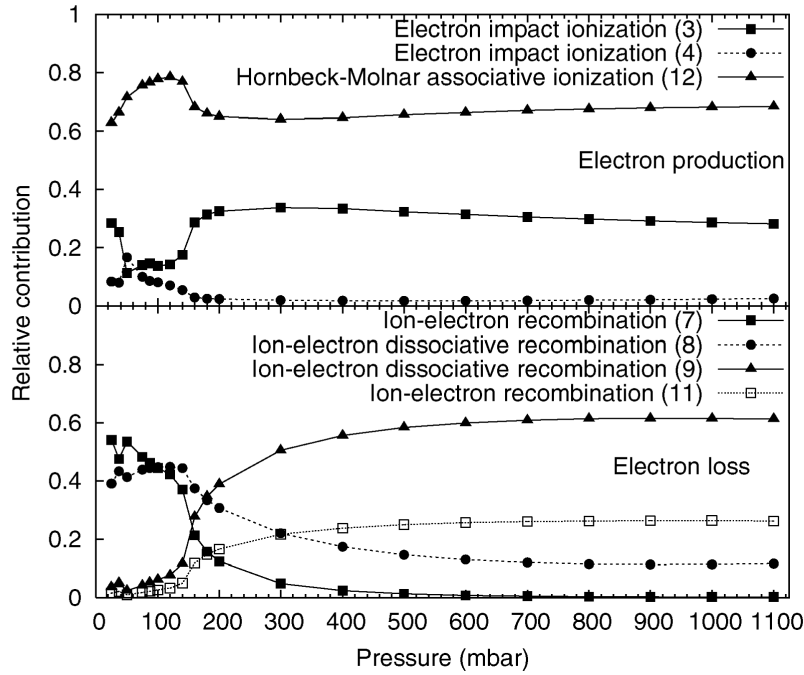


**Figure 3.15:** Calculated relative contributions of the chemical reactions leading to the production and destruction of the electrons at the maximum current for different pressures.

seen that Hornbeck-Molnar associative ionization (reaction 12) contributes for 60 to 80% to the production of the electrons at every pressure. Also electron induced ionization (reaction 3) has a significant influence ranging from 15 to 35% in the entire pressure range.

In the bottom frame of figure 3.15 the relative contributions of the chemical reactions leading to the loss of the electrons are shown. For pressures below 160 mbar ion-electron recombination (reaction 7) and ion-electron dissociative recombination (reaction 8) both have relative contributions of about 40 to 50%. For pressures above 160 mbar the loss of the electrons appears to be governed mainly by ion-electron dissociative recombination (reaction 9), ion-electron recombination (reaction 11) and ion-electron dissociative recombination (reaction 8).

For every pressure none of the above mentioned loss processes attains a reaction rate value above  $1.7 \times 10^{17} \text{ cm}^{-3}\text{s}^{-1}$ . These rates are negligible in comparison with the electron production rates shown in figure 3.14 for Hornbeck-Molnar associative ionization (reaction 12) and electron induced ionization (reaction 3). As a consequence, Hornbeck-Molnar associative ionization is the reaction with the largest influence on the electron densities. In figure 3.14 the Hornbeck-Molnar associative ionization (reaction 12) shows very high reaction rates in the range from 50 to 140

mbar. This behavior is responsible for the high electron densities in that same pressure range. For higher pressures the Hornbeck-Molnar associative ionization (reaction 12) also shows a rise in figure 3.14 similar to the electron induced excitation (reaction 1), but it is less steep. This explains why the rise of the electron densities for higher pressures (shown in figure 3.12) is less steep than the rise of the  $\text{He}_m^*$  densities shown in figure 3.11.

For every pressure the influence of the Hornbeck-Molnar associative ionization on the electron densities is found to be very important. For the electrons it is shown that the high electron densities in the range from 50 to 140 mbar are directly caused by the Hornbeck-Molnar associative ionization (reaction 12).

## $\text{He}_2^+$

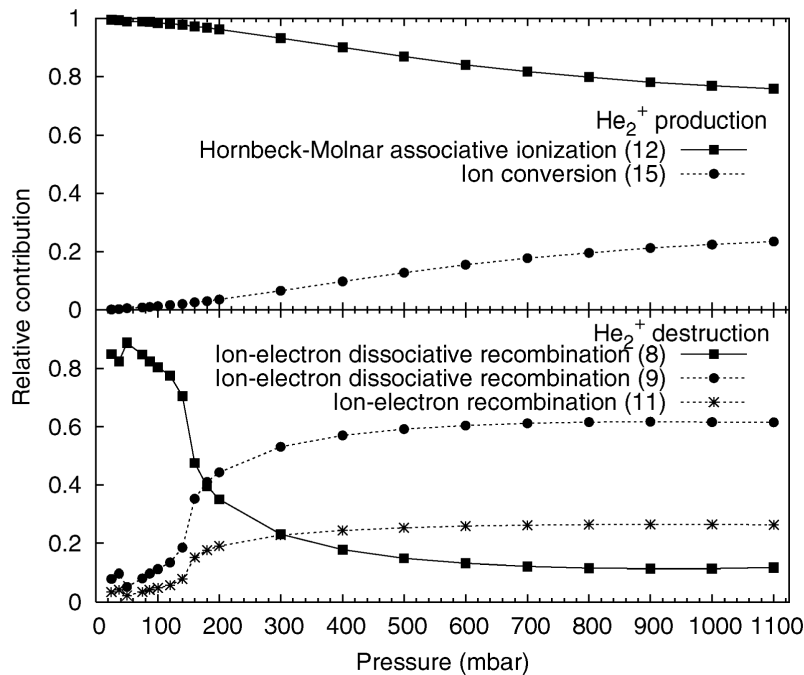


**Figure 3.16:** Calculated relative contributions of the different chemical reactions leading to the production and destruction of the  $\text{He}_2^+$  ions at the maximum positive current for different pressures.

The relative contributions of the different reactions to the production and destruction of  $\text{He}_2^+$  are presented in figure 3.16. The top and bottom frame show the relative contributions to the production and destruction of  $\text{He}_2^+$ , respectively. The Hornbeck-Molnar associative ionization (reaction 12) is again clearly the most

important production reaction. However for higher pressures also the ion conversion (reaction 15) attains relative contributions of about 10 to 20%. The bottom frame in figure 3.16 shows that the destruction of  $\text{He}_2^+$  is completely governed by ion-electron dissociative recombination (reactions 8 and 9) and ion-electron recombination (reaction 11). These three  $\text{He}_2^+$  destruction reactions are already discussed above as electron loss processes and have been found negligible in comparison with the reactions shown in figure 3.14.

The Hornbeck-Molnar associative ionization (reaction 12) and the ion conversion (reaction 15) are both shown in figure 3.14. It is already stated that Hornbeck-Molnar associative ionization is clearly the most important  $\text{He}_2^+$  production process. Therefore, the higher reaction rates of Hornbeck-Molnar associative ionization in the range from 50 to 140 mbar (see figure 3.14) are directly responsible for the higher  $\text{He}_2^+$  densities in that pressure range.

The rise of the  $\text{He}_2^+$  densities as a function of pressure (see figure 3.12) is mostly governed by the Hornbeck-Molnar associative ionization. However, since the ion conversion (reaction 15) shown in figure 3.14 rises more clearly as a function of pressure, it attains a larger contribution in the production of  $\text{He}_2^+$  (see figure 3.16). Since the rise of the ion conversion (reaction 15) as a function of pressure is higher than the rise of Hornbeck-Molnar associative ionization, the  $\text{He}_2^+$  densities also obtain a steeper rise as a function of pressure, compared to the electron densities.

## $\text{He}^+$

In figure 3.17 the relative contributions of the different reactions leading to the production (top frame) and the destruction (bottom frame) of  $\text{He}^+$  are presented at pressures ranging from 25 to 1100 mbar. This figure shows that the production of  $\text{He}^+$  is completely governed by electron induced ionization from ground state He (reaction 3) for almost every pressure. The destruction of  $\text{He}^+$ , shown in the bottom frame, is completely governed by the ion conversion (reaction 15), except for pressures below 100 mbar.

In figure 3.12 it is shown that also the  $\text{He}^+$  ions have a higher density in the range from 50 to 140 mbar. For higher pressures, however, these densities seem to drop. The higher densities of  $\text{He}^+$  in the range from 50 to 140 mbar are due to the higher reaction rates of electron induced ionization from the  $\text{He}_m^*$  particles (reaction 4, shown in figure 3.14). The influence of the destruction reactions is small at low pressures, since their rates stay below  $1.7 \times 10^{17} \text{ cm}^{-3}\text{s}^{-1}$ . The high reaction rate of the electron induced ionization (reaction 4) at low pressure is due to the increased  $\text{He}_m^*$  and electron densities in that range (shown in figure 3.11).

The decrease of the  $\text{He}^+$  density as a function of pressure is due to the main destruction process, namely the ion conversion (reaction 15). Figure 3.17 shows that

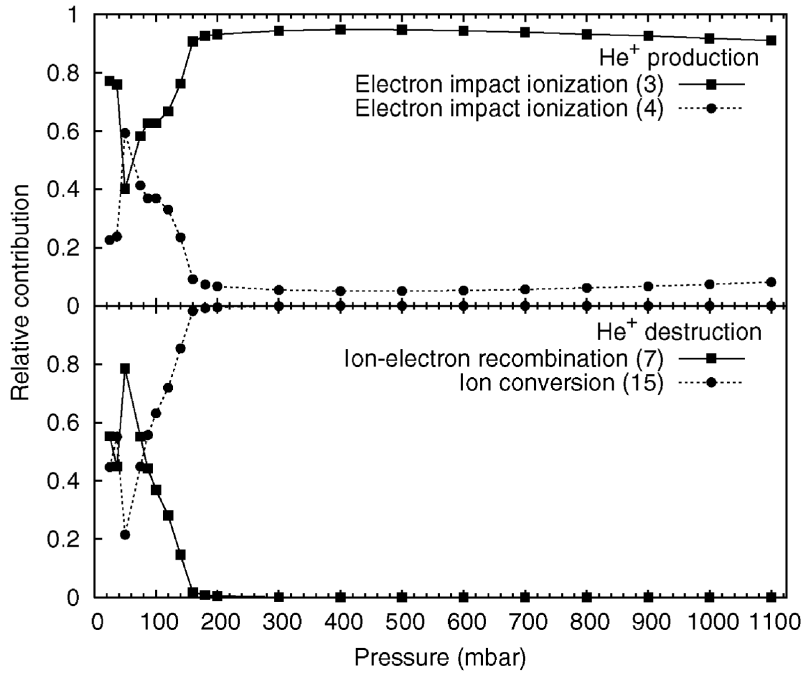


**Figure 3.17:** Calculated relative contributions of the different chemical reactions leading to the production (top frame) and destruction (bottom frame) of  $\text{He}^+$  ions.

at higher pressures the electron induced ionization of the He ground state (reaction 3) is the main  $\text{He}^+$  production reaction and also that the ion conversion (reaction 15) is the main  $\text{He}^+$  loss reaction. In figure 3.14 it is shown that electron induced ionization (reaction 3) does not significantly rise as a function of pressure. The ion conversion (reaction 15), however, exhibits a significant rise as a function of pressure. Since the main production process does not show appear to change much under the influence of the pressure and the main destruction process shows a significant rise, the  $\text{He}^+$  densities illustrated in figure 3.12 decrease as a function of pressure.

## $\text{He}_2^*$

In figure 3.11 the spatially averaged densities of  $\text{He}_2^*$  for pressures ranging from 25 to 1100 mbar are depicted. This figure shows the  $\text{He}_2^*$  densities at maximum current density, ranging from 0.1 to 0.3  $\text{A cm}^{-2}$  depending on pressure. At the given moments in time, the current density is very much determined by the conduction current and does not necessarily coincide with the maximum densities of the neutral particles.  $\text{He}_2^*$  is the only plasma species that does not achieve a maximum density at the maximum current. Indeed  $\text{He}_2^*$  is much more important in the afterglow of

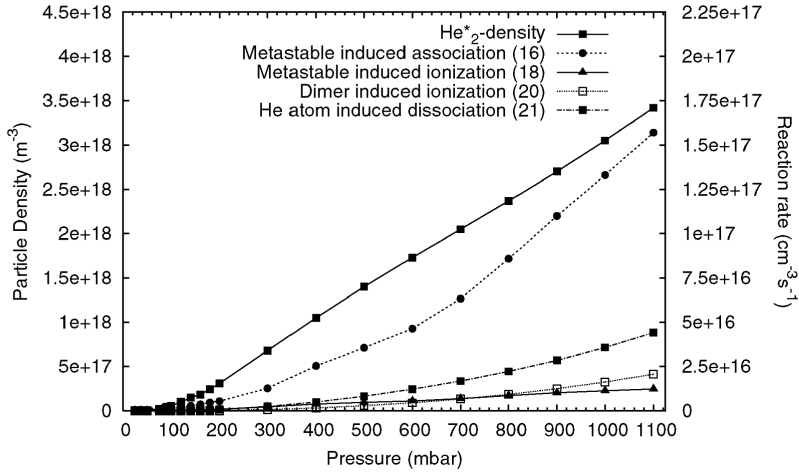


**Figure 3.18:** Maximum values of the calculated spatially averaged densities of  $\text{He}_2^*$  and the reaction rates of the most important production and destruction reactions.

the discharge. Therefore, to study the influence of the pressure on the  $\text{He}_2^*$  density, we present in figure 3.18 the  $\text{He}_2^*$  densities and the rates of the important production and destruction processes as a function of pressure at a later time in the discharge (about  $15 \mu\text{s}$  later). Figure 3.18 clearly shows that at a later time in the discharge  $\text{He}_2^*$  becomes a very important plasma species. It is also clearly observed that the  $\text{He}_2^*$  densities rise steeply as a function of pressure. This rise is due to the metastable induced association (reaction 16) illustrated in figure 3.18. The relative contribution of the metastable induced association (reaction 16) to the production of  $\text{He}_2^*$  is more than 86% for every pressure. The three processes that govern the destruction of  $\text{He}_2^*$  are also shown in figure 3.18. These are the metastable induced ionization (reaction 18), the dimer induced ionization (reaction 20) and the He atom induced dissociation (reaction 21). Figure 3.18 shows that the metastable induced association (reaction 16) is also much more important than these destruction processes. This reaction has a great dependency on the He background gas pressure (see Table 3.1), which explains the steep rise as a function of pressure. Therefore also the  $\text{He}_2^*$  densities show the same rise.

## He\*\*

It can be seen in Table 3.1 that the electron induced excitation (reaction 2) and the Hornbeck-Molnar associative ionization (reaction 12) are the sole processes where  $\text{He}^{**}$  is involved. Therefore, the production and destruction of this particle is completely governed by these two reactions. Figure 3.11 shows that the  $\text{He}^{**}$  atoms only attain significant densities at pressures below 150 mbar. Hence it appears that

for pressures above 150 mbar the Hornbeck-Molnar associative ionization (reaction 12) completely suppresses the production of  $\text{He}^{**}$ .

It appears that the higher plasma activity in the range from 50 to 140 mbar is closely related to the He densities and the associated Hornbeck-Molnar associative ionization reaction. Figure 3.14 illustrates that the Hornbeck-Molnar associative ionization has a reaction rate that is almost twice the rate of the second most important reaction in that pressure range. It is shown above that the high densities in that pressure range of the two most important charge carriers,  $\text{He}_2^+$  and the electrons, are also directly related to this reaction. Subsequently, the densities of the other plasma species are directly influenced by these newly formed charge carriers.

Hence, it can be concluded that these  $\text{He}^{**}$  densities are rather low for every pressure, but they appear to play a crucial role in the mechanisms of the discharge.

### 3.4.3 The stability of the discharge

In 2001 Miclea and coworkers [44] stated that in this experimental configuration any kind of noble gas with pressures from 10 to 180 mbar can be ignited and sustained. Our calculations show that in the range from 50 to 140 mbar the plasma is significantly more active, as can be seen in the profile of the current densities which are three times as high (see figure 3.9) and in the profiles of the plasma densities, which are also clearly higher in that range (see figures 3.11 and 3.12). This observation appears to confirm the choice of operating pressures made by Miclea and coworkers [44].

However, the pressure range in which a merely stable discharge can be obtained appears to be much larger in our calculations. Indeed our calculations predict that a stable discharge can be obtained with pressures ranging from 15 to 1113 mbar at a constant applied voltage of 750 V<sub>pp</sub>. The reasons for the lower and upper limit are evident. Below the pressure of 15 mbar the He background gas density is too low. Therefore there are not enough collisional reactions to create a stable plasma. This effect is illustrated in figure 3.19, where we present the average electron energy at maximum current as a function of pressure. This figure shows that at low pressures there are not enough collisions for the electrons to lose energy and therefore at lower pressures the energy becomes higher and higher.

Above the pressure of 1113 mbar there are too many He background gas atoms, which causes the electrons to lose too much energy in collisions with He particles. Therefore, the electron energy becomes too low (cf. figure 3.19) and they are not able to perform enough ionization reactions to create a stable plasma for the same applied voltage.

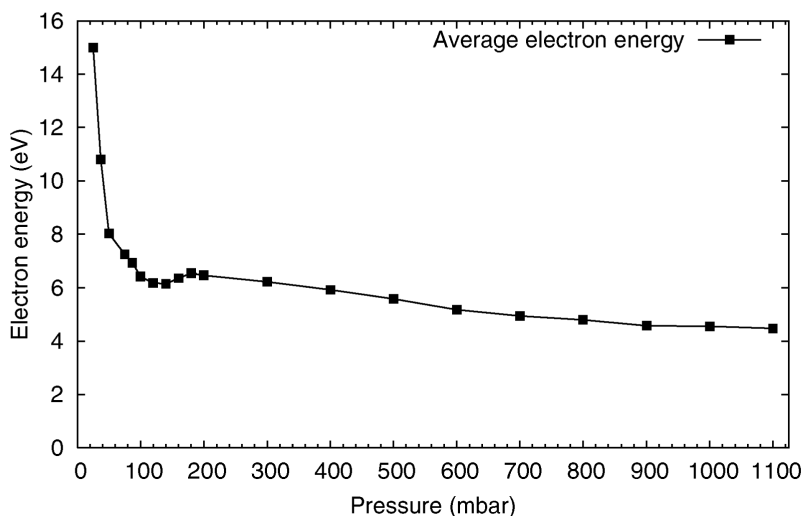


**Figure 3.19:** Calculated average electron energy at maximum positive current for the different pressures under study.

## 3.5 Conclusion

We have investigated by means of a numerical fluid model a dielectric barrier discharge (DBD) in helium, used as a source in analytical spectrochemistry. The model is applied for the same gap distance ( $960 \mu\text{m}$ ), dielectric thickness ( $20 \mu\text{m}$ ), type of dielectric (glass), voltage amplitude ( $750 \text{ V}_{\text{peak-to-peak}}$ ) and for applied voltage frequencies (5 to 20 kHz) as is common for this plasma source. The model describes the behavior of electrons,  $\text{He}^+$  and  $\text{He}_2^+$  ions, He metastable atoms ( $\text{He}_m^*$ ) and He atoms in highly excited levels ( $\text{He}^{**}$ ), as well as the  $\text{He}_2^*$  dimers. Characteristic for a DBD is that one or both electrodes are covered with dielectrics, which affects the electrical behavior of the DBD significantly. Indeed, the potential difference applied between both electrodes drops not only inside the plasma, but also across the dielectrics. Hence, the so-called gap voltage (or potential difference across the plasma) is clearly different from the applied voltage. It is the gap voltage, which determines the plasma characteristics. Consequently, the electrical current profile follows more closely the gap voltage profile than the applied voltage profile.

Beside the electrical characteristics and the potential distribution inside the plasma as a function of time, the model calculates also the spatial and temporal number density profiles of the various plasma species. It is found that, besides the He ground state atoms, the He atoms in metastable levels ( $\text{He}_m^*$ ) are the plasma species with the highest number density, with densities of at least an order of magnitude higher than the other plasma species densities. Moreover, the  $\text{He}_m^*$  atoms exhibit a different temporal behavior than the other plasma species. Indeed, the

electrons, ions and  $\text{He}^{**}$  highly excited atoms reach a maximum density when the applied voltage switches polarity and their density drops again rapidly as a function of time. The  $\text{He}_m^*$  metastable atoms, on the other hand, exhibit a very slow decay as a function of time. Finally, the density of the  $\text{He}_2^*$  dimers appears to be roughly time-independent, but of lower importance than the other plasma species. This situation becomes different when the DBD is operated at much higher pressures.

The relative contributions of the different production and loss mechanisms of the various plasma species were also determined, both at the peak of the species densities (i.e., when the applied voltage switches polarity) and during the plateau time of the applied voltage profile. It is illustrated that different production and loss mechanisms can become dominant at different moments in time.

In order to obtain more insight in the operation of this new plasma source for analytical spectrometry, we have also used the fluid model to investigate the influence of the background gas pressure.

Our results show that for this configuration in the region from 50 to 140 mbar the plasma current density is three times as high as outside this pressure range and that the electrons, the ions and the excited species, except for the  $\text{He}_2^*$  excimers, also have a distinctly higher density. This shows that for pressures from 50 to 140 mbar there is a higher plasma activity. This appears to be in agreement with the typical operating conditions of 10 to 180 mbar used in the experiments of Miclea and coworkers [44].

Our calculated stability range is, however, larger than 50 to 140 mbar. Stable discharges were obtained at pressures ranging from 15 to 1113 mbar. The lower pressure limit is due to the lack of background gas atoms available for collision in the discharge. The upper pressure limit is due to the loss of the electron energy in collisions with the background gas, resulting in too low electron energies to sustain the plasma.

In order to obtain information on the discharge regime we also investigated the spatial distributions of the potential and the charge densities. For two very different cases glow-like profiles with distinct positively charged sheaths and quasi-neutral plasma bulks were obtained.

The high plasma activity in the pressure range from 50 to 140 mbar has been found to be closely related to the Hornbeck-Molnar associative ionization reaction (reaction 12). Our calculations show that this reaction clearly has the highest rate in the pressure range from 50 to 140 mbar. The two most important charge carriers  $\text{He}_2^+$  and the electrons are directly formed by this reaction and subsequently, these species determine the formation of the other plasma species. Therefore, the calculations show that, although  $\text{He}^{**}$  has a low density in the discharge, it is an important source for the governing Hornbeck-Molnar associative ionization.

# Chapter 4

## Characterization of an atmospheric pressure DC glow discharge

### 4.1 Introduction

Glow discharges (GDs) at reduced pressure, typically between 50 and 500 Pa, are widely used for the analysis of (mainly solid) materials [116,117]. In recent years, however, there is increased interest for the analysis of liquids and gaseous samples. For these applications GDs operating at atmospheric pressure (so-called APGDs) appear to be particularly useful. Various groups have proposed different plasma designs and several review papers have been published on these APGDs and microplasmas, not only for analytical applications [101,98,102,81], but also for materials processing, environmental and biomedical applications [118,119]. The miniaturized direct current (dc) GDs [120,63,66,64,65] are based on similarity laws, which state that the gap between the electrodes must be reduced when pressure is increased (see Chapter 1, Section 1.3.1). They have been applied for instance for dc microplasma ‘on a chip’ gas chromatography [63,66,64,65]. Also the use of microhollow cathode dc discharges (MHCDs) has been investigated for analytical applications [121]. Radiofrequency (rf) powering schemes have also been applied, in order to avoid transient instabilities at the electrodes [69,71,70,73,74,75,77]. Sturgeon and coworkers developed the so-called furnace atomization plasma emission spectrometry (FAPES) system, where a graphite furnace was used for atomization, in combination with an rf He plasma for excitation [73,74,75,77]. A variant of this was the furnace atomization plasma ionization mass spectrometry (FAPIMS) system [78]. This rf powering is often combined with dielectric barrier materials at the surface of one or both electrodes (DBD), which can operate both at atmospheric pressure and reduced pressure

[97,122,44,94,96] (cf. Chapter 3). Also a pulsed corona discharge has been applied as ionization source for ion mobility spectrometry [123].

In 1993 Mezei and Czerfalvi [85] developed an APGD where a liquid sample directly served as the cathode, i.e. the so-called electrolyte cathode atmospheric glow discharge (ELCAD), to be used for liquids analysis. These authors published several papers characterizing this plasma [87,124,125]. This kind of plasma source and modified versions of it, which are generally called ‘liquid sampling APGD or LS-APGD’, were also adopted by other groups such as Kim and coworkers [126,127,89], Marcus and coworkers [90,92,128,91] and Hieftje and coworkers [93,129,130,131,132]. Marcus and coworkers also developed the so-called ‘particle beam’ (PB) sample introduction system for liquid samples into GD plasmas [133,134,135,136,137,138,139]. This PB interface was combined both with hollow cathode optical emission spectrometry (PB/HC-OES) [133,134,135,136,137,138] and with glow discharge mass spectrometry (PB/GDMS) [139].

Hieftje and coworkers have been particularly active in recent years in developing new designs for APGDs. The so-called annual GD [140], maintained in atmospheric pressure He between a tubular cathode and a rod-shaped anode was developed for solution analysis. For gaseous analysis the Hieftje group reported on a versatile direct current (dc) APGD in He, interfaced with a time-of-flight mass spectrometer [141,142]. A very stable APGD could be maintained between a rod-shaped cathode and anode, separated by a distance of 1 cm. The anode was characterized by a conical end, which appeared to help in stabilizing the discharge in the high-pressure regime. This APGD was characterized by Andrade and coworkers [142] by means of electrical and spectroscopic measurements. It could be deduced from the presence of  $\text{He}^+$  ions in the mass spectrum that a significant amount of energy was available for the ionization of gaseous analyte species. When this detection system is coupled with hydride generation, the analytical performance becomes comparable to that of an inductively coupled plasma source [141].

This APGD has also been modified by Andrade and coworkers [143,144], to be used in the flowing afterglow mode as a chemical ionization source for organic mass spectrometry. The ions and excited species generated by the APGD were transported outside the discharge chamber, where they reacted with atmospheric constituents. This so-called flowing atmospheric pressure afterglow (FAPA) source has been applied both for ionization of compounds in the gas phase [143], as well as for desorption ionization for the direct analysis of solid compounds [143]. Furthermore, Shelley and coworkers coupled the source with laser ablation to be used for molecular mass spectral imaging [145] and made also a detailed comparison with another ambient ionization source, i.e. the so-called direct analysis in real time (DART) [146]. Although both sources appear to be similar at first glance, they seem to operate in different regimes, i.e. corona-to-glow transition for DART and glow-to-arc transition

for the FAPA source. Finally, Schilling and coworkers applied the FAPA source for elemental analysis through hydride generation [147]. This study demonstrated the ability to use an ambient mass spectrometry source, commonly used for molecular analysis, for the detection of gas phase elemental species with the possibility of performing speciation analysis by coupling with a separation technique.

To optimize the applications of APGDs, a thorough characterization of the GD plasma is desirable. This can be done by experiments, but due to the small dimensions, measuring inside the plasma is not always practical. Moreover, measuring the number densities of the various species present in the plasma is not so straightforward. In this respect, computer modeling can be very useful.

There exist several papers in the plasma physics literature about modeling APGDs [14,9,148,149,150]. Most commonly, fluid approaches are applied [14,9,148,149], although the particle-in-cell Monte Carlo technique has been used as well [150]. Most studies concern DBDs, because of their increasing applications in materials processing, environmental and biomedical applications [37,3]. We have also studied a reduced pressure DBD, used as a microchip source for analytical spectrometry [151] of which we have investigated the effect of pressure in the discharge [152] (cf. Chapter 3). In 2003 Shi and Kong presented a hybrid model for a dc APGD in He used for material processing applications [153]. The model was based on a so-called kinetic description in the cathode fall region and a hydrodynamic model in the rest of the discharge. The calculation results confirmed many characteristics of GDs and correlations were made with low-pressure GDs in terms of the manifestation of the structural characteristics, especially in the formation of the non-equilibrium cathode fall and a nearly neutral positive column.

In the past decades, comprehensive models to describe the plasma behavior of reduced pressure GDs used for analytical spectrometry were developed in our group [154,155,156]. However, these insights cannot directly be transferred to APGDs, because of the different operating conditions, i.e. the typically high voltage and low current at reduced pressure and vice versa at higher pressure. Moreover, the structure of the GD is also different in both cases. In the low pressure case the positive column region is typically absent, whereas this region can become the dominant one at atmospheric pressure. This was very nicely demonstrated in [142]. Therefore, the present paper focuses on modeling efforts for an APGD used for spectrochemical analysis. As a case study, the APGD described by Wetzal [141] and Andrade [142] in 2006 is investigated, but the results can be transferred also to other APGD designs.

## 4.2 Description of the simulations

### 4.2.1 Models, species and chemical reactions

To describe the APGD, we make use of fluid as well as Monte Carlo (MC) simulations. Fluid modeling is particularly useful for describing plasmas at atmospheric pressure. At high pressure the plasma species have high number densities and they take part in many collisions. To describe these species and all their collisions with a kinetic model like MC simulations, would be very time-consuming. Moreover, at high pressure the plasma species can lose much of their energy by collisions, so that a fluid approach is generally acceptable, because the gain of energy by the electric field is more or less balanced by the loss of energy due to collisions. However, this is not really true for the electrons, because they gain more energy from the electric field than they lose by collisions. Therefore, we have also developed a MC model to describe the behavior of the electrons in the APGD.

As mentioned above, the APGD under study is the one described by Wetzel [141] and Andrade [142] in 2006. It operates at atmospheric pressure helium (99.999% purity). Because some nitrogen peaks are detected in the UV-VIS emission spectrum [142], we have included 10 ppm nitrogen in the calculations. The species included in the model comprise the background gases He and N<sub>2</sub>, the ions He<sup>+</sup>, He<sub>2</sub><sup>+</sup>, N<sub>2</sub><sup>+</sup> and N<sub>4</sub><sup>+</sup>, the metastable He atoms (He<sub>m</sub><sup>\*</sup>) and the He excimers (He<sub>2</sub><sup>\*</sup>), as well as the electrons. Atomic N, N<sup>+</sup> and N<sub>3</sub><sup>+</sup> ions are not taken into account, because they play a minor role in the plasma [157].

The chemical reactions and the reagents considered in the model differ from the reactions used in Chapter 3. For the simulation of atmospheric pressure helium it was chosen to stay more consistent with the successful chemical descriptions of Mangolini and coworkers [8], Sommerer and coworkers [158] and Golubovskii and coworkers [9]. These descriptions are not too complicated and account for the most important effects such as the influence of the molecular gas N<sub>2</sub> and electron energy depending reaction rate coefficients. The reactions considered in the model are presented in Table 4.1, as well as their rate coefficients and the references where these data are adopted from. For the electron induced reactions, energy dependent cross sections are used. In order to include the electron energy loss associated with the rotational and vibrational excitation of N<sub>2</sub>, we included excitations to a rotational level at 0.02 eV and to two vibrational levels at 0.29 and 0.291 eV as additional energy loss terms in the electron energy continuity equation.

**Table 4.1:** Complete set of reactions used in the model with their reaction rate coefficients. The electron impact reactions are described with energy-dependent cross sections. The last column gives the references where the rate coefficients and cross sections are adopted from. In the MC model, the electron induced reactions (reactions 1,2 and 3) are included as well as electron induced excitation of the N<sub>2</sub> impurities to the lowest rotational and vibrational levels.

No.	Reaction	Rate Coeff.	Ref.
1	$e^- + \text{He} \rightarrow e^- + \text{He}_m^*$	$f(\sigma)$	[6,159]
2	$e^- + \text{He} \rightarrow 2 e^- + \text{He}^+$	$f(\sigma)$	[6,159]
3	$e^- + \text{He}_m^* \rightarrow 2 e^- + \text{He}^+$	$f(\sigma)$	[6,159]
4	$2 e^- + \text{He}^+ \rightarrow e^- + \text{He}$	$3 \times 10^{-20} (T_g/T_e)^4 \text{ cm}^6 \text{ s}^{-1}$	[108]
5	$2 e^- + \text{He}^+ \rightarrow e^- + \text{He}_m^*$	$3 \times 10^{-20} (T_g/T_e)^4 \text{ cm}^6 \text{ s}^{-1}$	[108]
6	$e^- + \text{He}_2^+ \rightarrow \text{He}_m^* + \text{He}$	$8.9 \times 10^{-9} (T_g/T_e)^{1.5} \text{ cm}^3 \text{ s}^{-1}$	[9]
7	$e^- + \text{N}_2^+ \rightarrow \text{N} + \text{N} \rightarrow \text{N}_2$	$4.8 \times 10^{-7} (T_g/T_e)^{0.5} \text{ cm}^3 \text{ s}^{-1}$	[9]
8	$e^- + \text{N}_4^+ \rightarrow \text{N}_2 + \text{N}_2$	$2 \times 10^{-6} (T_g/T_e)^{0.5} \text{ cm}^3 \text{ s}^{-1}$	[160]
9	$\text{He}^+ + 2 \text{He} \rightarrow \text{He}_2^+ + \text{He}$	$1.1 \times 10^{-31} \text{ cm}^6 \text{ s}^{-1}$	[9]
10	$\text{He}_2^+ + \text{N}_2 \rightarrow \text{He}_2^* + \text{N}_2^+$	$1.4 \times 10^{-9} \text{ cm}^3 \text{ s}^{-1}$	[9]
11	$\text{N}_2^+ + 2 \text{N}_2 \rightarrow \text{N}_4^+ + \text{N}_2$	$1.9 \times 10^{-29} \text{ cm}^6 \text{ s}^{-1}$	[161]
12	$\text{N}_2^+ + \text{N}_2 + \text{He} \rightarrow \text{N}_4^+ + \text{He}$	$1.9 \times 10^{-29} \text{ cm}^6 \text{ s}^{-1}$	[161]
13	$\text{N}_4^+ + \text{N}_2 \rightarrow \text{N}_2^+ + 2 \text{N}_2$	$2.5 \times 10^{-15} \text{ cm}^3 \text{ s}^{-1}$	[160]
14	$\text{N}_4^+ + \text{He} \rightarrow \text{N}_2^+ + \text{N}_2 + \text{He}$	$2.5 \times 10^{-15} \text{ cm}^3 \text{ s}^{-1}$	[160]
15	$\text{He}_m^* + 2 \text{He} \rightarrow \text{He}_2^* + \text{He}$	$2 \times 10^{-34} \text{ cm}^6 \text{ s}^{-1}$	[9]
16	$\text{He}_m^* + \text{He}_m^* \rightarrow \text{He}^+ + \text{He} + e^-$	$1.5 \times 10^{-9} \text{ cm}^3 \text{ s}^{-1}$	[108]
17	$\text{He}_m^* + \text{He}_m^* \rightarrow \text{He}_2^+ + e^-$	$1.5 \times 10^{-9} \text{ cm}^3 \text{ s}^{-1}$	[9]
18	$\text{He}_m^* + \text{N}_2 \rightarrow \text{He} + \text{N}_2^+ + e^-$	$5 \times 10^{-11} \text{ cm}^3 \text{ s}^{-1}$	[9]
19	$\text{He}_2^* + \text{M} \rightarrow 2 \text{He} + \text{M}$	$10^{-4} \text{ s}^{-1}$	[9]
20	$\text{He}_2^* + \text{He}_2^* \rightarrow \text{He}_2^+ + 2 \text{He} + e^-$	$1.5 \times 10^{-9} \text{ cm}^3 \text{ s}^{-1}$	[9]
21	$\text{He}_2^* + \text{N}_2 \rightarrow 2 \text{He} + \text{N}_2^+ + e^-$	$3 \times 10^{-11} \text{ cm}^3 \text{ s}^{-1}$	[9]

## 4.2.2 Description of the fluid model

The fluid model is the same model that is described in Chapter 2 Section 2.3. For the ions in the discharge the local field approximation was assumed, using mobilities that were obtained from [60,162,163]. The diffusion coefficients were calculated from the mobilities using the Einstein relation (eq. 2.7 Chapter 2). For the neutral species experimental diffusion coefficients were used obtained from [164].

For the boundary conditions at sides where there is no dielectric or electrode present the derivative of the quantities such as electric potential, species density or energy density were assumed to be zero. At the sides where there is a physical boundary such as a dielectric or electrode the flux expressions are characterized by zero densities for ions and excited species, due to neutralization and de-excitation respectively. For the electrons, the boundary condition was mainly determined by

secondary electron emission from the ions using a secondary electron emission coefficient of 0.092 for the helium ions and 0.01 for the nitrogen ions. The coefficients were chosen as such to match the experimental discharge current measured by Andrade and coworkers [142].

### 4.2.3 Description of the Monte Carlo model

As mentioned above, we have also developed a MC model for the electrons, to describe their behavior in more detail, because they are not really in equilibrium with the electric field. The MC model is based on following the behavior of a large number of individual electrons. It is not possible to follow all electrons in the plasma within a reasonable time scale, because of the typical number densities of  $10^{18}$  electrons per  $\text{m}^3$  (see below, Section 4.3.4). Therefore, the real electrons are replaced by so-called super-electrons, which represent a fixed number of real electrons, as defined by their weight. Typically, about  $10^5$  super-electrons are followed, to obtain good statistics.

The behavior of these super-electrons is described, one after the other, as a function of time. During successive time steps their trajectory under the influence of the electric field in the plasma, is calculated by solving Newtons laws. The probability for a collision during that time step,  $Prob_{coll}$ , is calculated with eq. 4.1 and compared with a random number between 0 and 1:

$$Prob_{coll} = 1 - \exp\left(-\Delta s \sum (n\sigma_{coll}(\varepsilon))\right) \quad (4.1)$$

$\Delta s$  is the distance traveled during the time step, while  $n$  and  $\sigma_{coll}(\varepsilon)$  are the densities of the target particles and the cross sections of the different collision types of the electrons with energy  $\varepsilon$ . If the probability is lower than the random number, no collision occurs. If the probability is higher, a collision takes place and the kind of collision that takes place needs to be determined.

The collisions taken into account in the model are elastic collisions with He atoms, electron induced ionization and excitation from the He ground state atoms and the  $\text{He}_m^*$  metastable levels. Most electron induced collisions with the  $\text{N}_2$  molecules are neglected, as these species are only present as an impurity (10 ppm). However, electron induced excitation to the lowest rotational and vibrational levels of  $\text{N}_2$  is included, because it can be important to determine the electron energy distribution function in the low energy range [157, 165]. The references where the cross sections of these processes are adopted from, were presented in Table 4.1 above.

To determine which collision takes place, the partial collision probabilities of the various collisions are calculated based on the individual cross sections. The total collision probability, which is equal to one because it is the sum over all partial collision probabilities, is subdivided in intervals with lengths corresponding to these

partial collision probabilities. A second random number between 0 and 1 is generated and the interval into which the random number falls, determines the collision that takes place. Then, the new energy and direction after collision are also defined by random numbers, based on energy and angular differential cross sections.

This procedure of calculating the trajectory by Newtons laws and treating the collisions by random numbers is repeated during successive time steps, until the super-electron is lost by recombination at the cell walls. Then, the next super-electron is followed. It should be noted that some new super-electrons can be created by ionization collisions. These additional super-electrons are also followed with the same procedure.

#### 4.2.4 Discharge cell geometry and operating conditions

The fluid and MC model are applied to the APGD setup, described by Wetzel [141] and Andrade [142]. A schematic diagram is presented in figure 4.1a. The discharge chamber is a 10 cm cubic aluminum cell. The anode and cathode are located on opposite faces of the cell. The cathode is a 3 mm diameter tungsten rod with a flat, polished end surrounded by a 3 mm internal diameter and 6.35 mm outer diameter alumina tube, to limit the cathode area. The anode is a cylindrical 2.5 cm diameter brass rod with a conical end with a half-angle of  $60^\circ$ . The gap between the anode tip and the cathode is 1 cm. For the simulations only the region between anode and cathode is important, where the plasma is most intense. Therefore, the calculation results will be presented only in the shaded box, illustrated in figure 4.1a. Moreover, because of the cylindrical symmetry of this region only one half of this box is sufficient to present the results, because the data can be projected to the other sides of the axis of symmetry. Hence, figure 4.1b presents the details of the simulated area.

The calculations are performed for typical conditions of this APGD, as reported by Andrade [142], i.e., a He pressure of 1 atm with 10 ppm of  $N_2$  as impurity gas and a dc discharge voltage of 650 V. Secondary electron emission coefficients of 0.092 for helium ions and 0.01 for nitrogen ions and a gas temperature of 1350 K [142] are assumed. These conditions provide for a discharge current of 30 mA, which is also obtained in the experiments [142].

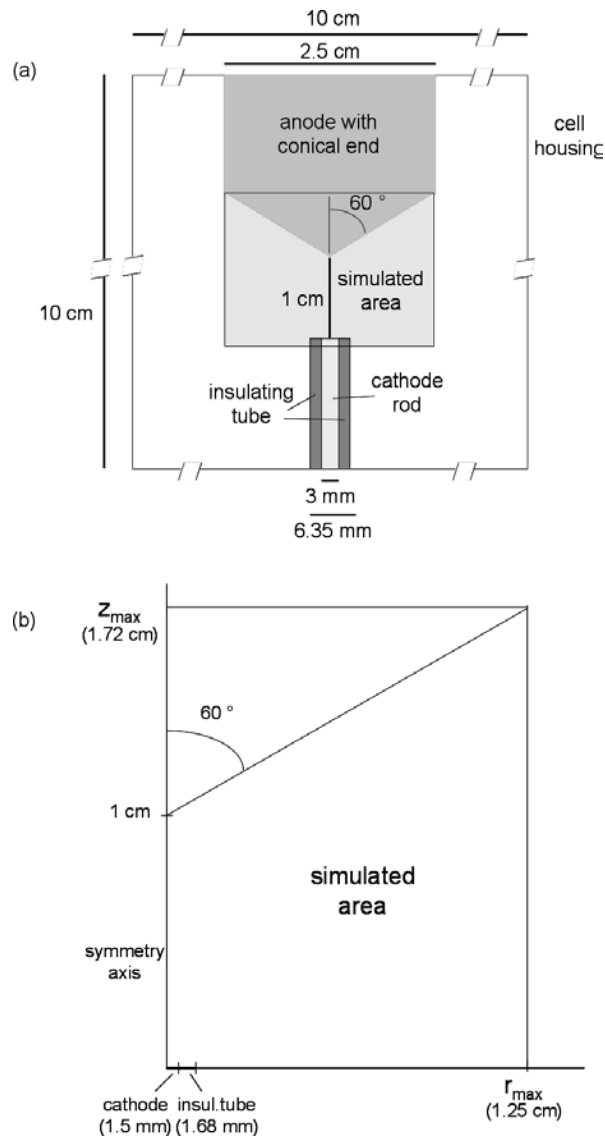


**Figure 4.1:** Schematic diagram of the APGD source under study (not completely to scale) (a) The shaded box gives the simulated area. Because of the cylindrical symmetry, the calculation results will be presented in only one-half of this box, as indicated in part b.

## 4.3 Characterization of the discharge

### 4.3.1 Electric potential and field distributions

Figure 4.2 illustrates the calculated potential distribution (part a) and the axial and radial electric field distributions (parts b and c) in one half of the cell, as calculated with the fluid model. The cathode is found at the left end of the figure ( $Z=0$  cm), whereas the anode cone is at the right. The symmetry axis is at  $R=0$  cm. As can be observed from figure 4.2(a), the potential drops very quickly from  $-650$  V at the cathode to about  $-300$  V at a distance of  $0.25$  mm from the cathode. This small region can be seen as the cathode dark space (CDS) region. It is much thinner than the CDS in reduced pressure GDs, where typical values of about  $0.5$ - $5$  mm are reported for pressures in the range of  $50$ - $700$  Pa [166,167,155]. However, it is in the same range as the CDS width of  $0.2$  mm, calculated for a needle cathode in atmospheric pressure helium [165] and a CDS width of  $0.4$  mm calculated for a DBD operating in the same gas [9]. This is to be expected, because it is generally known that the CDS thickness drops with increasing pressure [166].

Another difference with reduced pressure GDs is the behavior of the potential in the rest of the discharge. Indeed, in the present case the potential remains negative in the entire discharge region and it increases only gradually from  $-300$  V at the end of the CDS to zero at the anode. This is completely different from the reduced pressure case, where the potential is slightly positive (typically a few up to  $10$  V) and almost constant in the largest part of the discharge (i.e. the so-called negative glow (NG) region), before it returns to zero at the anode [167,155]. Such a NG region is not clearly observed in the atmospheric pressure case. Therefore, we can conclude that the APGD consists of a small CDS and a large positive column (PC), which fills most of the discharge region, whereas this PC is typically absent in reduced pressure GDs used for analytical spectrometry [154,167]. It is indeed generally accepted that with increasing pressure (or larger distance between anode and cathode) a PC is formed and can become the largest region in the discharge [168,18]. Hieftje and coworkers have also clearly demonstrated by means of photography the growing importance of the PC region in the APGD under study here when raising the pressure from a few Torr to atmospheric pressure [142]. The presence of a PC is also observed in other publications on APGDs [14,9,148,153].

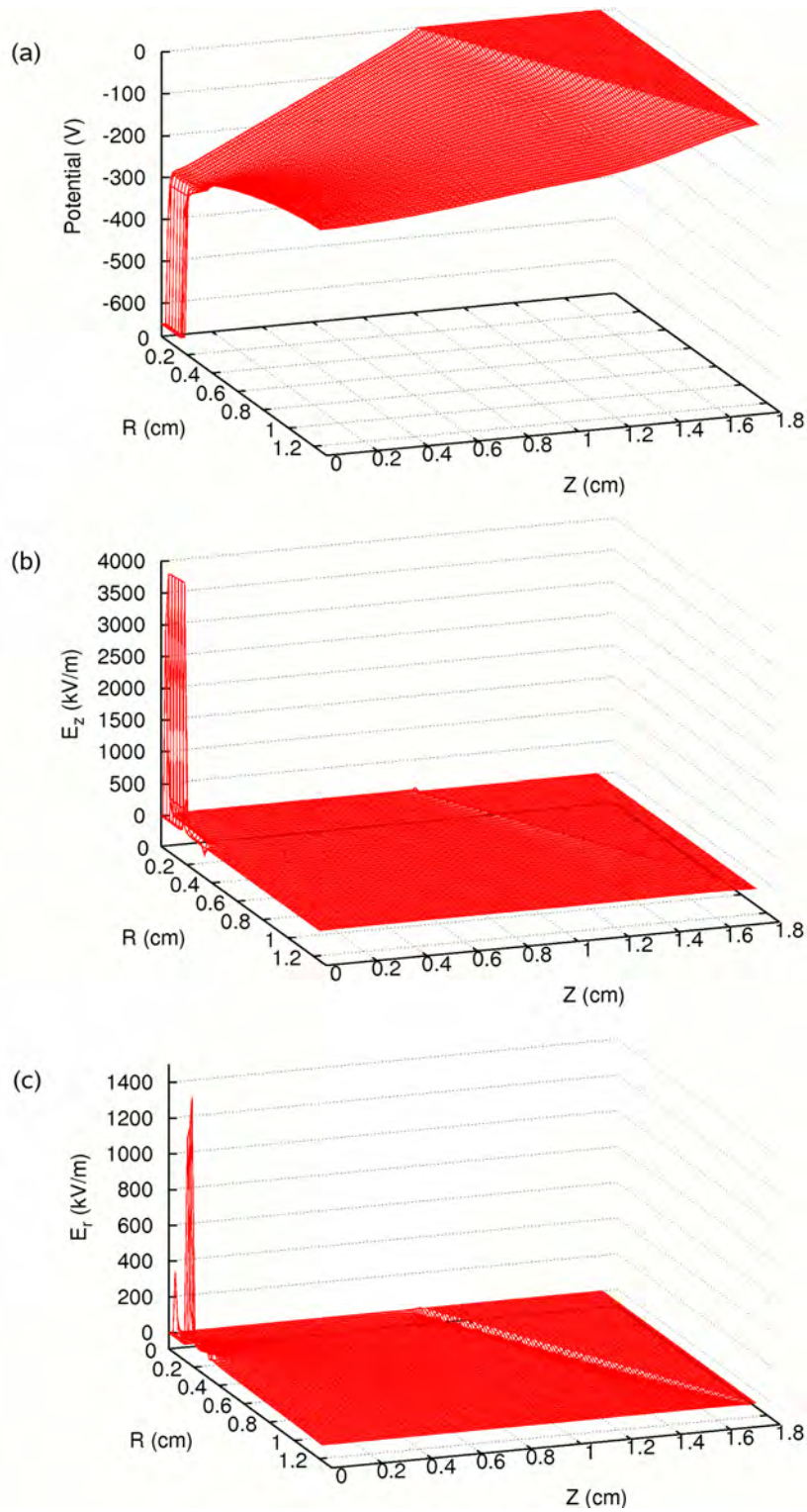


**Figure 4.2:** Calculated 2D electric potential distribution (a) and axial (b) and radial (c) electric field distributions in the cell geometry illustrated in figure 4.1b. The cathode is found at the left ( $Z=0$ ) whereas the anode cone is at the right. The symmetry axis is at  $R=0$ .

The potential distribution presented in figure 4.2a gives rise to an axial and radial electric field distribution, illustrated in parts b and c of figure 4.2, respectively. In the CDS the axial electric field is  $3.8 \times 10^6$  V/m which was also found by Shi and Kong for similar conditions in a parallel plate setup [153] and it is about 2-3 times higher than the obtained values for atmospheric pressure DBDs of  $1.1-1.8 \times 10^6$  V/m [14,9]. The calculated value is about five times higher than the reduced pressure GD value of about  $8 \times 10^5$  V/m obtained for both DC and pulsed DC discharges [169,107]. However, it remains high (in the order of  $3 \times 10^4$  V/m) in most of the discharge region, which is different from the reduced pressure GD situation. It points out the importance of the PC region, in order to ensure a sufficient flux of electrons towards the anode by accelerating them in the electric field and hence to maintain the electrical current throughout the discharge [168,55]. Indeed, it appears that at atmospheric pressure, the electrons lose so much of their energy by collisions, that they would not be able to reach the anode, unless they are accelerated by this electric field in the PC region. The radial electric field is presented in figure 4.2c. It is very localized next to the alumina tube with values slightly above  $10^6$  V/m. Since the alumina tube is charged by the plasma, also in the radial direction a rather strong electric field is formed. The radial field is not so important since there is no electrode in this direction and the distance to the wall of the discharge cell is 5 cm.

### 4.3.2 Mean electron energy

The mean electron energy, as calculated with the MC model, is plotted in figure 4.3 in one half of the cylindrically symmetrical discharge region. In the CDS the electrons gain a lot of energy from the electric field, but they lose most of this energy by inelastic collisions, such as ionization and excitation of the He gas. Therefore, their mean energy is only in the order of 50 eV. This is considerably lower than in reduced pressure GDs, where the mean electron energy at the end of the CDS can be as high as 500-800 eV (i.e. for 1000-1200 V discharge voltage, depending on the pressure) [167,155]. This difference is of course explained by the fact that at low pressure the electrons do not lose so much energy by collisions.

However, because of the significant axial electric field in the PC region, the mean electron energy remains considerable (i.e., about 6 eV) in the largest part of the discharge and it increases again to almost 10 eV at the anode cone. These results are very similar to the results obtained by Shi and Kong for a dc parallel plate setup in atmospheric pressure helium [153]. In their work a mean electron energy of 40 eV at the cathode is obtained together with a bulk energy of about 10 eV, as well as a small increase at the anode reaching 15 eV. This profile has important consequences for the electron induced collision rates, as will be illustrated below.

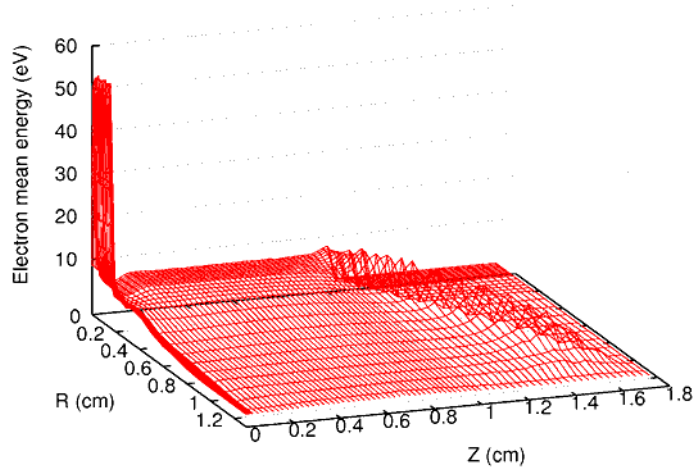


**Figure 4.3:** Calculated 2D profile of the mean electron energy.

### 4.3.3 Electron induced collision rates

Figure 4.4 presents the two-dimensional (2D) distributions of the electron induced reaction rates, as obtained from the MC calculations. The wire surfaces present the data on a linear scale, while the flat surfaces in the plane of the R and Z axis present the data on a logarithmic scale. In this way an estimate of the order of magnitude of the bulk values can be given. Light tints represent low values and dark tints represent high values. Figure 4.4a illustrates that the mean electron energy is only sufficient to produce ionization from the He ground state atoms in the CDS region. Indeed, this process requires 24.6 eV. This is in the range of the mean electron energy calculated at the end of the CDS, but is much higher than the mean electron energy of 10 eV in the PC. However, the logarithmic scale demonstrates that the calculated ionization rate in the PC is not zero. This is because the electrons are characterized by an energy distribution with a tail ranging to much higher energies and the latter can give rise to these inelastic collisions. The electron impact ionization rate reaches a peak of almost  $4 \times 10^{26} \text{ m}^{-3} \text{ s}^{-1}$ , which is several orders of magnitude higher than the ionization rates obtained in reduced pressure GDs, typically in the order of  $10^{22}$ - $10^{23} \text{ m}^{-3} \text{ s}^{-1}$  [167]. However, it is still about four orders of magnitude below the ionization rates reported for a dc APGD in  $\text{H}_2$  [170] in a rod to plane setup.

These high localized ionization rates are again due to the atmospheric pressure giving rise to many collisions, until the energy becomes too low for ionization, which

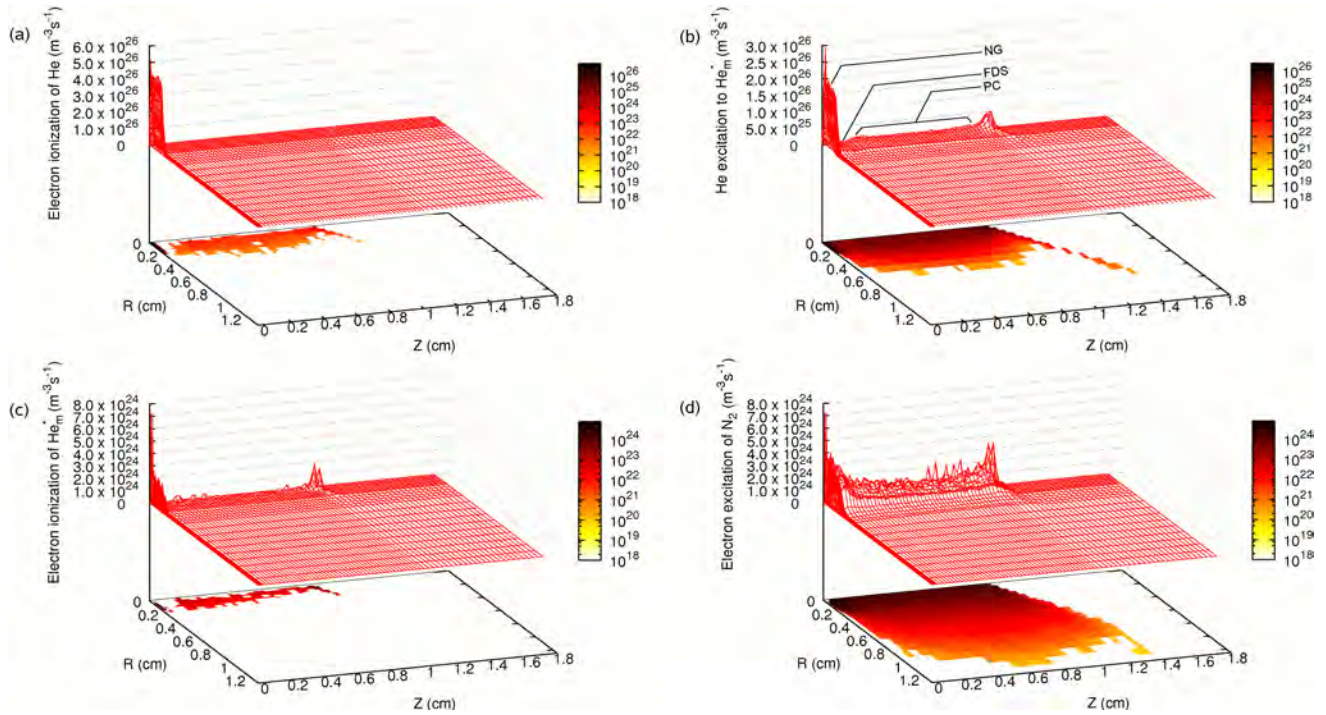


**Figure 4.4:** Calculated 2D profiles of the electron induced reaction rates: (a) ionization of He ground state atoms, (b) excitation to the  $\text{He}_m^*$  metastable atoms, (c) ionization from the  $\text{He}_m^*$  metastable atoms and (d) rotational-vibrational excitation of the  $\text{N}_2$  molecules. In part b, different spatial zones of the GD, as obtained from the excitation (or emission) intensities are also schematically indicated.

occurs already at the end of the CDS. This is important, because it prevents an ionizing cascade, which would lead to an arc, as is also discussed in [142]. Integrated over the entire discharge region, the overall ionization rate of He will therefore be quite moderate.

The rate of electron induced excitation (figure 4.4b) reaches also a maximum at the end of the CDS (or the beginning of the NG), but in contrast to the electron induced ionization rate, it is clearly non-zero in the region between cathode and anode, with again a small peak near the anode tip. This is explained by the increase in mean electron energy, as was anticipated above. Note that figure 4.4b presents the electron induced excitation rate to the  $\text{He}_m^*$  metastable levels. The maximum value appears to be comparable to the maximum in the electron induced ionization rate. However, the total electron induced excitation rate from the He ground state atoms is about twice as high as the excitation rate to the  $\text{He}_m^*$  metastable levels, as it includes also excitation to all other levels. It is not shown here, because it looks qualitatively very similar to figure 4.4b, with a pronounced maximum in the CDS, small but non-zero values in the region between cathode and anode and a second

maximum near the anode tip. The reason that the total excitation rate is twice as high as the ionization rate, in spite of the fact that the cross section is lower [159], is due to the lower threshold for excitation compared to ionization (i.e., 19.8 eV vs. 24.6 eV). This also explains the non-zero values in the region between cathode and anode on the linear scale and the small maximum near the anode tip.

Finally, it should be noted that the most significant contributions in the excitation rate (visible on the linear scale) occur only for a radial position up to about 2.5 mm from the cell axis. This corresponds to the radius of the cathode and some part of the insulating tube around the cathode (cf. figure 4.1). Indeed, when the electrons are emitted from the cathode, they can move slightly in the radial direction away from the discharge center, but they are mostly accelerated in the forward direction by the axial electric field. Therefore, there are not many electrons present at radial distances further than 2 mm from the discharge axis and, consequently, not many electron induced collisions will occur in this region.

The calculated electron induced excitation rate profile is in excellent agreement with the spatial distribution of HeI lines, as measured by Hieftje and coworkers [142], which exhibits also a pronounced peak near the cathode, very low values in the gap between cathode and anode and a second, smaller maximum near the anode. Moreover, our calculation results compare favorably with the photographs taken of the APGD [142]. Indeed, Hieftje and coworkers observed a very bright thin layer on the cathode surface (called the NG), followed by a small dark region (the Faraday dark space or FDS) and a very diffuse cylinder of light, corresponding to the PC region, with a diameter slightly larger than the cathode diameter and with the maximum intensity close to the anode [142]. This is exactly what is predicted with our MC simulations, presented in figure 4.4b. The different spatial zones are therefore also schematically indicated in this figure.

Although electron induced ionization from the He ground state atoms is found to be almost negligible in the largest part of the discharge, ionization from the  $\text{He}_m^*$  metastable atoms appears to be possible in the region between cathode and anode and especially near the anode tip, as is clear from figure 4.4c. Indeed, a much lower amount of energy is required to ionize the  $\text{He}_m^*$  metastable levels, as they are already excited to 19.8 eV. Hence, only 4.8 eV is needed to ionize them, compared to 24.6 eV for the ionization of the He ground state atoms. Comparing the absolute values of parts a and c of figures 4.4 tells us that the ionization rate from the  $\text{He}_m^*$  metastable levels is almost two orders of magnitude lower than ionization from the He ground state. Nevertheless, this illustrates again that ionization from the  $\text{He}_m^*$  metastable levels is more efficient (due to the lower energy threshold), because the  $\text{He}_m^*$  metastable atom density is more than 5 orders of magnitude lower than the He background gas density (see below, Section 4.3.4).

Finally, figure 4.4d illustrates the rate of rotational and vibrational excitation of

the  $\text{N}_2$  gas. We included excitations to one rotational level at 0.02 eV and to two vibrational levels at 0.29 and 0.291 eV as additional energy loss processes. Note that the  $\text{N}_2$  density is also 5 orders of magnitude lower than the He density, at an impurity level of 10 ppm, and hence, comparable to the  $\text{He}_m^*$  density. Nevertheless, the rate of rotational and vibrational excitation of the  $\text{N}_2$  gas is considerable, because the cross section reaches a maximum between 1 and 5 eV, which is close to the mean electron energy in the discharge (cf. figure 4.3). This process is important, as it determines the electron energy distribution function in the lower energy region, where the other inelastic processes with He (ionization, excitation) do not occur. Indeed, the threshold for rotational and vibrational excitation is assumed to be 0.02 eV, which is significantly lower than the threshold for ionization and excitation of He (i.e., 24.6 eV and 19.8 eV, respectively).

#### 4.3.4 Plasma species number densities

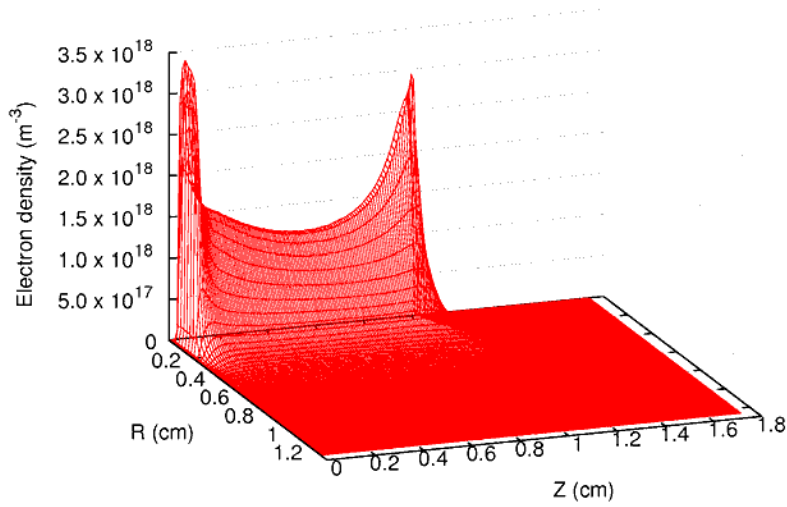


**Figure 4.5:** Calculated 2D electron number density profile.

The 2D electron number density profile is plotted in figure 4.5. The results shown here were obtained with the fluid model, but the MC simulations yielded almost exactly the same profile, which can be considered as a partial validation of both models. The electron density reaches a maximum of about  $3.5 \times 10^{18} \text{ m}^{-3}$  at a distance of 0.35 mm from the cathode, which corresponds to the end of the CDS region. This is quite similar to low pressure GDs, although in that case a much

broader maximum is observed, which fills most of the NG region [167,155]. Indeed, in the present case the density drops quickly by about a factor of 2 and maintains values of about  $1.4 \times 10^{18} \text{ m}^{-3}$  throughout the gap between cathode and anode, until it increases again to values of about  $3 \times 10^{18} \text{ m}^{-3}$  near the anode cone (i.e., at the end of the PC region). As was anticipated above, the density becomes negligible at radial distances further than 2.5 mm from the discharge axis, because the electrons emitted from the cathode are mainly accelerated in the axial direction. The two maxima in the electron number density profile correspond to the two maxima in the electron impact ionization rate (at least for ionization from the  $\text{He}_m^*$  metastable levels) and are characteristic for an APGD, where the PC region plays an important role.

We believe that this second maximum in electron density and in electron impact ionization and excitation rates is partly induced by the conical end of the anode rod. Indeed, figure 4.2a demonstrated two important effects that influence the electrons. The cone shaped end with a half angle of  $60^\circ$  creates an active region where the distance between the electrodes decreases and consequently the electric field slightly increases. In this way a funnel-like potential distribution is created, as can be seen in figure 4.2a, which confines the discharge towards the axis of symmetry of the setup and can be an important effect to maintain and stabilize the discharge. The second effect is the already mentioned potential gradient in the PC region. While in reduced pressure GDs the electrical potential in the plasma bulk is often slightly positive without any gradient, in this APGD setup there is clearly still a potential gradient in the plasma bulk. This provides for a weak electric field that pushes the electrons towards the anode. Since there is no strong electric field at that location, a population of electrons with rather low energies is accumulated, as can be seen in figure 4.3. Hence, there is a significant population of electrons near the anode in order to ionize the  $\text{He}_m^*$  metastable levels, but the population of electrons with enough energy to ionize ground state He is rather small. This explains the two maxima for the ionization rate of  $\text{He}_m^*$  and the single maximum for the ionization rate of ground state He.

Comparing the absolute values of the electron number density between the APGD and reduced pressure GDs where values of  $10^{17}$ - $10^{20} \text{ m}^{-3}$  are commonly reported [167,155], tells us that the electron density is in the same order of magnitude, in spite of the higher gas pressure in the APGD. From the ideal gas law the He background gas density at 1 atm and 1350 K can be estimated in the order of  $10^{25} \text{ m}^{-3}$ . This indicates that the ionization degree in the APGD is very low, i.e., in the order of  $10^{-7}$ , compared to  $10^{-5}$ - $10^{-3}$  for reduced pressure GDs [155,171].

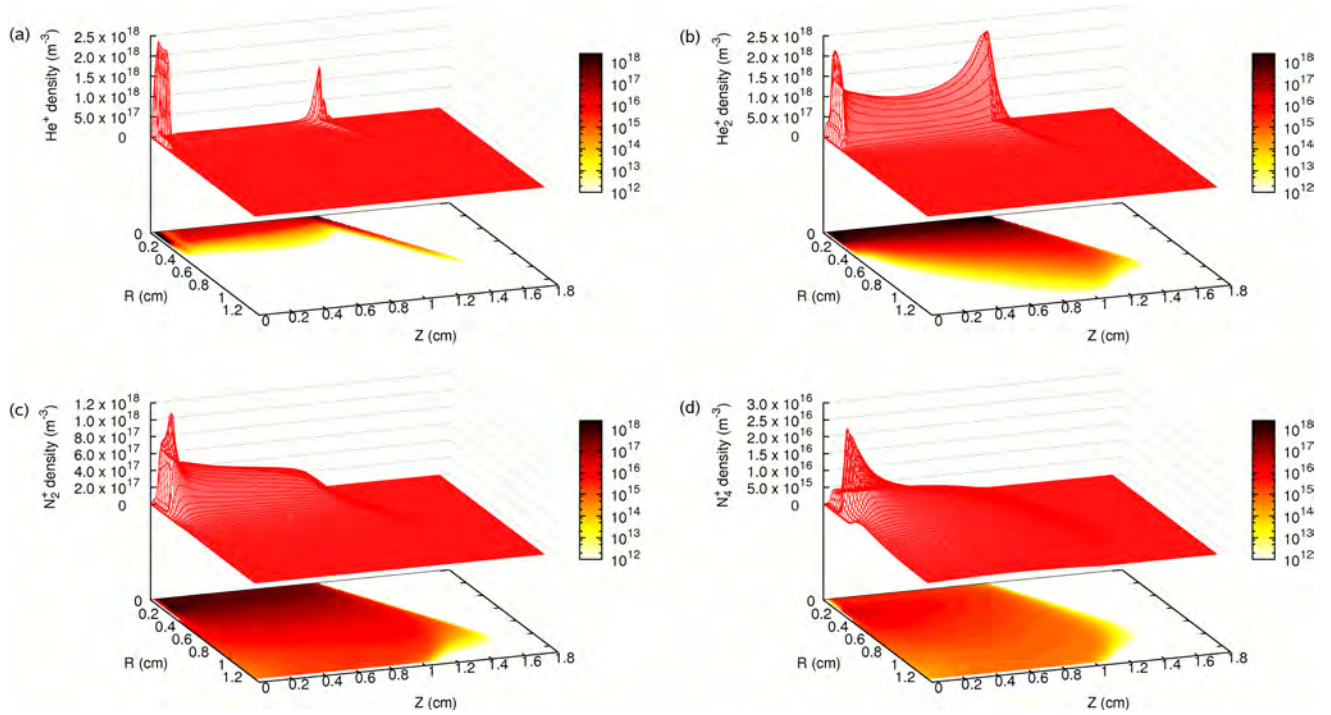


**Figure 4.6:** Calculated 2D number density profiles of the  $\text{He}^+$  (a),  $\text{He}_2^+$  (b),  $\text{N}_2^+$  (c) and  $\text{N}_4^+$  (d) ions.

Figure 4.6 presents the 2D number density profiles of the various ions in the plasma. The  $\text{He}^+$  density (figure 4.6a) reaches a pronounced maximum of  $2.3 \times 10^{18} \text{ m}^{-3}$  near the cathode and a second maximum of about  $10^{18} \text{ m}^{-3}$  near the anode tip, but in between the density is virtually zero in most of the plasma region. This is different from the  $\text{He}_2^+$  density (figure 4.6b), which exhibits also two maxima in the same order of magnitude as the  $\text{He}^+$  density, but the second maximum is clearly higher (up to  $2.5 \times 10^{18} \text{ m}^{-3}$ ) and broader, and more importantly, the density does not drop to zero in between these maxima, but remains in the order of  $10^{18} \text{ m}^{-3}$  throughout the discharge, at least for radial distances up to 2.5 mm from the discharge axis. Therefore, the  $\text{He}_2^+$  density is characterized by a similar profile as the electron density (cf. figure 4.5).

Hence, from parts a and b of figure 4.6 it can be concluded that the  $\text{He}_2^+$  ions are present at a higher density in the plasma than the  $\text{He}^+$  ions. At first sight this might be a bit unexpected, as the  $\text{He}^+$  ions are directly formed by electron impact ionization from the He background gas, whereas the  $\text{He}_2^+$  ions can only be formed by secondary reactions (i.e., reactions 9, 17 and 20 of Table 4.1; see also Section 4.3.5). Nevertheless, it is quite common in APGDs that the molecular ions are more important than the atomic ions [157, 172, 34].

Parts c and d of figure 4.6 illustrate the  $\text{N}_2^+$  and  $\text{N}_4^+$  number density profiles.

These ions are not characterized by a second maximum near the anode, but the first maximum near the cathode is followed by a gradual decrease in density throughout the discharge. It is also apparent from these figures that the maximum is shifted slightly off-axis. Comparing the absolute values tells us that the  $N_2^+$  ion density is only slightly lower than the  $He^+$  and  $He_2^+$  densities, in spite of the fact that the  $N_2$  gas density is 5 orders of magnitude lower than the He gas density. This is because the  $N_2^+$  ions are easily produced by secondary reactions (i.e., reactions 10, 13, 14, 18 and 21 from Table 4.1), as will also be explained later. Hieftje and coworkers also observed intense emission from the APGD, attributed to  $N_2^+$  bands [142]. For the  $N_4^+$  ions, on the other hand, our calculations predict a density about two orders of magnitude lower than the other ion densities and hence, it does not really contribute to the space charge.

In our calculated results for DBDs that will be presented in Chapter 5, the effect of  $N_2$  impurities in an atmospheric pressure He DBD was investigated [157,173]. It was demonstrated that the  $He^+$  ions were negligible for all  $N_2$  impurity levels investigated (0-2000 ppm). The  $He_2^+$  ions were only dominant for impurity levels below 1 ppm. In the region between 1 and 17 ppm of  $N_2$ , the  $N_2^+$  ions appeared to have the highest density, whereas for higher impurity levels, the  $N_4^+$  ions became predominant [157]. Naturally, the operating conditions were different in that study (i.e., a parallel plate DBD with a sinusoidal applied voltage of 2.6 kV amplitude and 10 kHz frequency), but it illustrates that it is indeed not so unexpected that the  $N_2^+$  and even the  $N_4^+$  ions can play an important role in dc powered He APGDs, even with small  $N_2$  impurity levels.

Comparing the  $N_2^+$  ion density with the  $N_2$  gas density of about  $10^{20} \text{ m}^{-3}$  at 10 ppm impurity level, tells us that the ionization degree of  $N_2$  is significantly higher than the He ionization degree, i.e., in the order of  $10^{-3}$ - $10^{-2}$ . This finding is important for analytical applications, because it suggests that the APGD in He can also in general efficiently ionize gaseous analytes or aerosols, for detection with mass spectrometry [142].

Figure 4.7 depicts the total positive ion density (i.e., sum of all ions from figure 4.6), as well as the electron density, as a function of distance from the cathode on the axis of symmetry. It is observed that the total ion density is more or less equal to the electron density, so that there exists charge neutrality in most of the discharge region, except in the CDS where only the ions are present and the electron density is virtually zero, leading to a positive space charge region. This characteristic is typical for a (reduced pressure) GD. Figure 4.7 explains the potential distribution on the axis of symmetry of the setup. Since the positively charged sheath is very small and the region with charge neutrality is very big, the cathode potential is not able to rise up to a zero or slightly positive value. Since the rest of the discharge has charge neutrality and cannot disturb the electric field, the electric potential continues to rise linearly up to the grounded anode. These features are typical for a glow

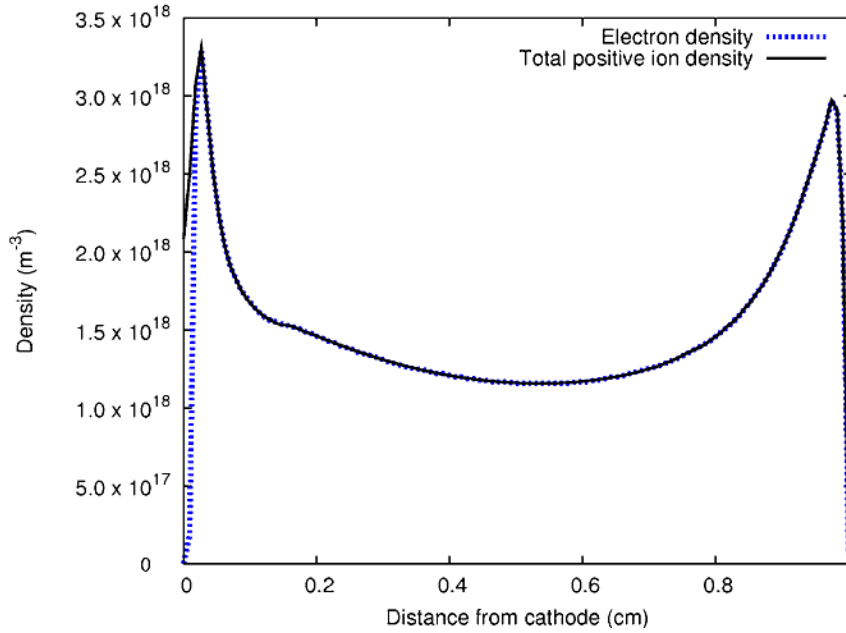


**Figure 4.7:** Calculated 1D profiles of the total positive ion number density (i.e. sum of  $\text{He}^+$ ,  $\text{He}_2^+$ ,  $\text{N}_2^+$ , and  $\text{N}_4^+$  ions; solid line) and electron density (dashed line) taken at the discharge axis.

discharge. Indeed, if we compare this result with an atmospheric pressure DBD in the Townsend regime, where the total positive ion density is typically significantly higher than the electron density (even up to two orders of magnitude [174,17,21]), we can conclude that the discharge under study in this chapter is definitely in the glow mode.

Finally, in figure 4.8, the 2D density profiles of the excited He species (i.e., the  $\text{He}_m^*$  metastable atoms in part a and the  $\text{He}_2^*$  excimers in part b) are plotted. The  $\text{He}_m^*$  density reaches a pronounced maximum near the cathode and a second smaller maximum near the anode. It has a considerably lower density in the bulk, but this value is still quite high in the order of  $10^{19} \text{ m}^{-3}$ , as can be seen on the logarithmic scale in figure 4.8a. This is in correspondence with the electron impact excitation rate (cf. figure 4.4b above). The  $\text{He}_2^*$  excimers are characterized by a similar profile as the electrons and  $\text{He}_2^+$  ions, with a pronounced maximum near the cathode, but still fairly high values in the gap and rising again to a second (broader but smaller) maximum near the anode. The maximum in the  $\text{He}_m^*$  density is 5 orders of magnitude lower than the He gas density (which is about  $10^{25} \text{ m}^{-3}$  at 1 atm and 1350 K, see above), but the overall fraction of metastables is of course lower, because the density is almost zero in the rest of the discharge, whereas the He gas has a nearly constant density distribution. The  $\text{He}_m^*$  metastables are in the sheath clearly

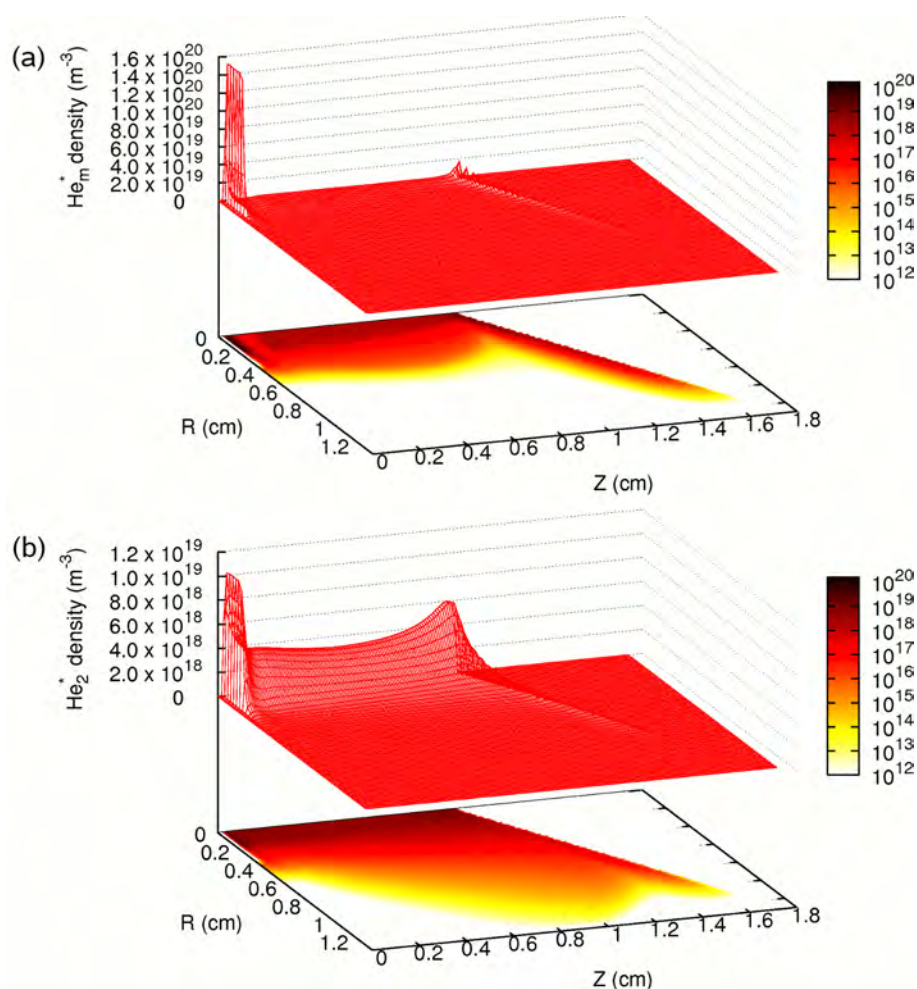


**Figure 4.8:** Calculated 2D number density profiles of the  $\text{He}_m^*$  metastable atoms (a) and the  $\text{He}_2^*$  excimers (b).

dominant over the excimer molecules, while in the plasma bulk their densities are of the same order, as can be seen by comparing the logarithmic surfaces in parts a and b of figure 4.8.

### 4.3.5 Production and loss processes of the plasma species

As stated by Andrade and coworkers [142], quantitative models for analytical APGDs have not yet been developed and the authors found it difficult to provide detailed explanations for the results they obtained, more specifically about the role of various processes and mechanisms [142]. For instance, it is generally established

[14,175] that  $\text{N}_2^+$  ions in He discharges can be formed through Penning ionization by  $\text{He}_m^*$  metastable atoms, as well as by asymmetric charge transfer of  $\text{He}_2^+$  ions, but it is not possible to determine a priori which of these reactions will be dominant in the APGD under study [142]. Therefore, Table 4.2 presents the calculated relative contributions of the most important production and loss processes for the different plasma species, obtained by integrating over the entire discharge region.

The  $\text{He}^+$  ions are mainly formed by electron impact ionization of He ground state atoms, as well as from the  $\text{He}_m^*$  metastable levels. Hornbeck-Molnar ionization, by collisions of two  $\text{He}_m^*$  atoms contributes for about 10%. The major loss mechanism is conversion into  $\text{He}_2^+$  ions, although electron-ion recombination, leading to either He ground state or excited atoms, also contributes for about 12%. All these production and loss rates are characterized by a maximum near the cathode and a second maximum near the anode tip, but virtually zero values in between.

**Table 4.2:** Calculated relative contributions (in %) of the production and loss processes for the various plasma species, taken into account in the model. The numbers between parentheses correspond to the reactions given in Table 4.1.

He <sup>+</sup> production processes	%	He <sup>+</sup> loss processes	%
Electron impact ionization from He (2)	63	Conversion into He <sub>2</sub> <sup>+</sup> (9)	88
Electron impact ionization from He <sub>m</sub> <sup>*</sup> (3)	27	Recombination with electrons (4,5)	12
Hornbeck-Molnar ionization from 2 He <sub>m</sub> <sup>*</sup> (16)	10		
He <sub>2</sub> <sup>+</sup> production processes	%	He <sub>2</sub> <sup>+</sup> loss processes	%
Hornbeck-Molnar associative ionization (17)	57	Charge transfer with N <sub>2</sub> (10)	99.9
Conversion from He <sup>+</sup> (9)	41	Recombination with electrons (6)	0.1
Ionization from 2 He <sub>2</sub> <sup>*</sup> (20)	2		
N <sub>2</sub> <sup>+</sup> production processes	%	N <sub>2</sub> <sup>+</sup> loss processes	%
Charge transfer between He <sub>2</sub> <sup>+</sup> and N <sub>2</sub> (10)	77	Recombination with electrons (7)	89
Penning ionization of N <sub>2</sub> by He <sub>m</sub> <sup>*</sup> (18)	13	Conversion into N <sub>4</sub> <sup>+</sup> ions (12)	11
Penning ionization of N <sub>2</sub> by He <sub>2</sub> <sup>*</sup> (21)	9		
Conversion from N <sub>4</sub> <sup>+</sup> ions (14)	2		
N <sub>4</sub> <sup>+</sup> production processes	%	N <sub>4</sub> <sup>+</sup> loss processes	%
Conversion from N <sub>2</sub> ions (12)	100	Recombination with electrons (8)	81
		Conversion into N <sub>2</sub> <sup>+</sup> ions (14)	19
He <sub>m</sub> <sup>*</sup> production processes	%	He <sub>m</sub> <sup>*</sup> loss processes	%
Electron impact excitation (1)	99	Hornbeck-Molnar associative ionization (17)	41
Electron-He <sup>+</sup> recombination (5)	1	Hornbeck-Molnar ionization (16)	24
		Electron impact ionization (3)	32
		Conversion into He <sub>2</sub> <sup>*</sup> (15)	2
		Penning ionization of N <sub>2</sub> (18)	1
He <sub>2</sub> <sup>*</sup> production processes	%	He <sub>2</sub> <sup>*</sup> loss processes	%
Charge transfer between He <sub>2</sub> <sup>+</sup> and N <sub>2</sub> (10)	73	Dissociation upon collision with third body (19)	58
Conversion from He <sub>m</sub> <sup>*</sup> (15)	27	Collision between two He <sub>2</sub> <sup>*</sup> (20)	33
		Penning ionization of N <sub>2</sub> (21)	9

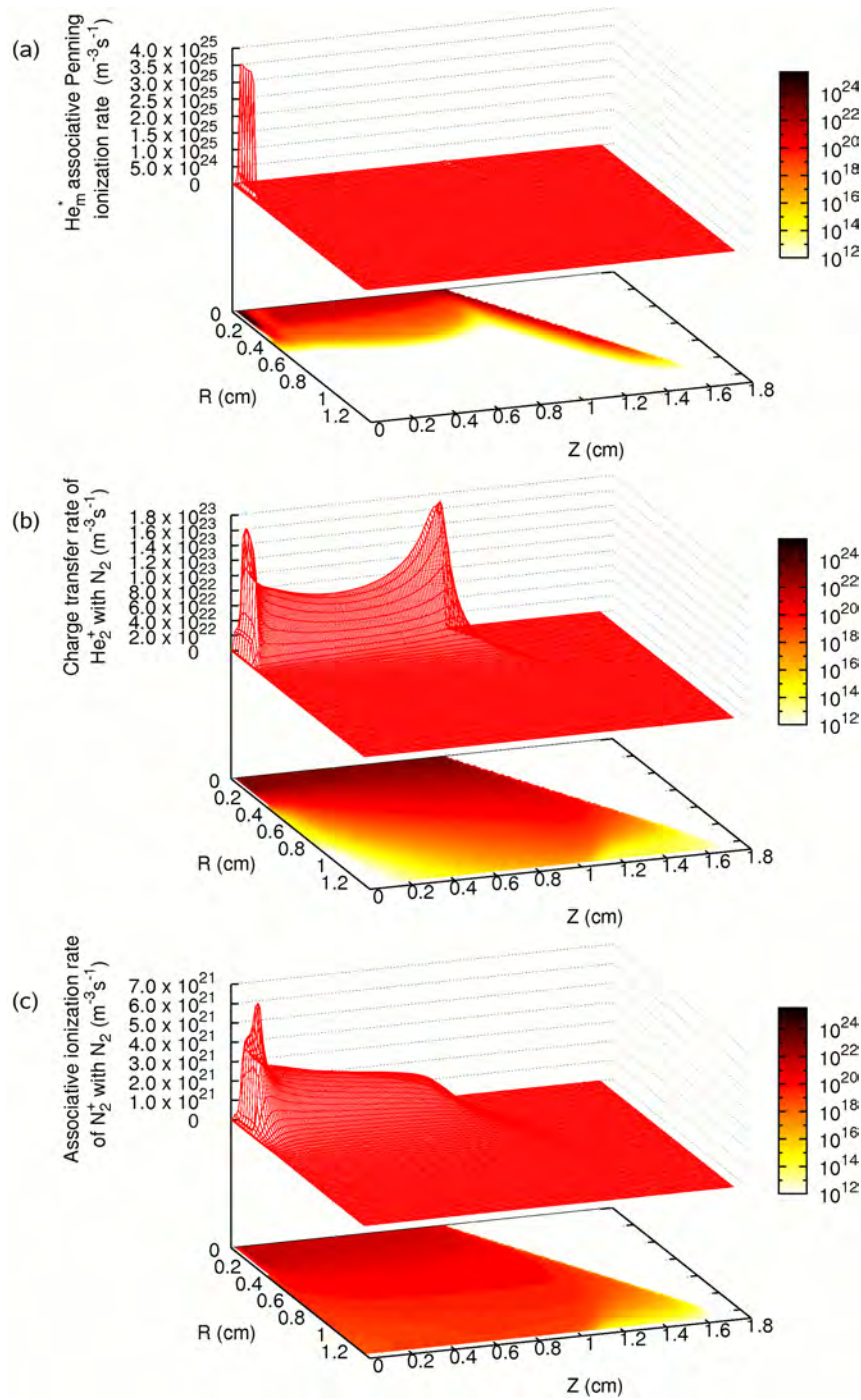


**Figure 4.9:** Calculated 2D reaction rate profiles of the dominant production mechanisms of (a) the  $\text{He}_m^+$  ions (i.e. Hornbeck-Molnar associative ionization), (b) the  $\text{N}_2^+$  ions and  $\text{He}_2^*$  excimers (i.e. charge transfer between  $\text{He}_2^+$  and  $\text{N}_2$ ) and (c) the  $\text{N}_4^+$  ions (i.e. conversion from  $\text{N}_2^+$  ions). The dominant production mechanisms for the  $\text{He}^+$  ions and  $\text{He}_m^*$  metastable atoms are electron induced ionization and excitation respectively, for which the rates were presented in figure 4.4a and b.

The  $\text{He}_2^+$  ions are mainly created by Hornbeck-Molnar associative ionization, i.e., due to collisions of two  $\text{He}_m^*$  atoms, although conversion out of  $\text{He}^+$  ions is also quite important. The rate of Hornbeck-Molnar associative ionization is plotted in 2D in figure 4.9a. It is clear that this rate exhibits a pronounced maximum near the cathode, but the values in the entire gap between cathode and anode are still rather high (see logarithmic scale). This explains why the  $\text{He}_2^+$  ions are also characterized by fairly high density values in the entire region between cathode and anode (see figure 4.6b above), in contrast to the  $\text{He}^+$  ions (cf. figure 4.6a), for which the dominant production process (i.e., electron impact ionization) showed a pronounced maximum near the cathode and was almost zero in the gap between cathode and anode (see figure 4.4 parts a and c).

The loss of  $\text{He}_2^+$  ions is almost exclusively due to charge transfer with  $\text{N}_2$  giving rise to  $\text{N}_2^+$  ions, as appears from Table 4.2. This is also the dominant production mechanism for the  $\text{N}_2^+$  ions. Other important production processes are Penning ionization of  $\text{N}_2$ , due to collisions with either  $\text{He}_m^*$  atoms or  $\text{He}_2^*$  excimers, which both contribute for roughly 10%. The rate of this dominant production process is depicted in figure 4.9b. It is characterized by two (nearly equal) maxima near the cathode and the anode and fairly high values in between, explaining the  $\text{N}_2^+$  density profile shown in figure 4.6c, except for the maximum near the anode, which has disappeared in the  $\text{N}_2^+$  ion density profile as a result of the loss processes. The loss of  $\text{N}_2^+$  ions is mainly attributed to recombination with electrons, although conversion into  $\text{N}_4^+$  ions upon collision with He gas atoms also contributes for 11%.

The latter process is entirely responsible for the creation of  $\text{N}_4^+$  ions, as is clear from Table 4.2. The rate of this process is presented in figure 4.9c. It exhibits the same profile as the  $\text{N}_2^+$  ion density and can also explain the  $\text{N}_4^+$  ion density profile. The  $\text{N}_4^+$  ions mainly get lost by recombination with electrons, although conversion into  $\text{N}_2^+$  ions upon collision with He gas atoms (i.e., the opposite from the production process) also contributes for nearly 20%.

Figure 4.9 illustrates that not all reaction mechanisms exhibit a pronounced peak near the cathode and a smaller peak near the anode, with very low values in between like the electron induced reaction rates, but can also be characterized by fairly high values in the entire PC region. This is in qualitative agreement with emission maps presented by Andrade and coworkers [142] for some molecular species.

As far as the excited species are concerned, the  $\text{He}_m^*$  metastable atoms are almost exclusively created by electron induced excitation from the ground state, whereas they get lost by several mechanisms, the most important being Hornbeck-Molnar (associative) ionization, giving rise to both  $\text{He}_2^+$  and  $\text{He}^+$  ions, as well as electron induced ionization from the metastable level.

Finally, the  $\text{He}_2^*$  excimers are mainly formed by charge transfer between  $\text{He}_2^+$  ions and  $\text{N}_2$  (which also appeared to be the dominant production process for the

$\text{N}_2^+$  ions; see above), as well as by conversion of  $\text{He}_m^*$  metastables into  $\text{He}_2^*$  excimers in a three-body collision with He gas atoms. The most important loss mechanisms for the  $\text{He}_2^*$  excimers are dissociation upon collision with a third body, as well as the collision among two  $\text{He}_2^*$  excimers, yielding ionization of one and dissociation of the other excimer. Finally, dissociation due to the collision with  $\text{N}_2$  molecules also contributes for about 10%.

## 4.4 Conclusion

Fluid and MC simulations are applied to characterize quantitatively an atmospheric pressure glow discharge (APGD) in He used for analytical spectrometry. The calculation results include the potential and electric field distributions in the plasma, the density profiles of the various plasma species throughout the discharge, the mean electron energy, as well as the rates of the various collision processes in the plasma and the relative importance of the different production and loss rates for the various species. The similarities and differences with low pressure glow discharge are discussed.

From the potential distribution, as well as from the electron impact excitation rate profile, the different spatial regions in the discharge can be distinguished. The positive column is dominating the discharge, in agreement with experimental observations [142]. Electron impact ionization is only occurring near the cathode, i.e., in the small CDS and NG regions and it becomes negligible at further distances, when the electron energy has dropped to too low values. This is important to limit the amount of ionization and to prevent the transition into an arc discharge. The  $\text{He}_2^+$  ions appear to be the dominant positive ions. They are present in the entire discharge gap, in contrast to the  $\text{He}^+$  ions, which are almost only observed near the cathode and anode. The  $\text{N}_2^+$  ion density is only slightly lower than the  $\text{He}_2^+$  and  $\text{He}^+$  ion densities, in spite of the much lower  $\text{N}_2$  density (i.e., assumed to be present as impurity of 10 ppm). This indicates that  $\text{N}_2$  gas molecules are more efficiently ionized, mainly by asymmetric charge transfer of  $\text{He}_2^+$  ions, as well as by Penning ionization due to  $\text{He}_m^*$  metastable atoms and  $\text{He}_2^*$  excimers. This suggests that the APGD has good potential as an ionization source for the analysis of gaseous compounds.



## Part III

# Fundamental investigations of the atmospheric pressure dielectric barrier discharge



# Chapter 5

## The influence of impurities

### 5.1 Introduction

The atmospheric pressure glow discharge (APGD) in a dielectric barrier discharge setup (DBD) has the very important advantage that it does not need robust vacuum chambers and it automatically avoids arc formation, due to the charge accumulation on the dielectrics [30].

The dielectric barrier APGD is most easily generated in a noble gas such as helium. For these noble gases it is recognized that generally at least some gas impurity is present and that these impurities play crucial roles in the generation mechanism of the atmospheric plasmas [14,34,9,176].

The influence of different levels of impurity in gas discharges is important in both experimental and simulation research efforts. In experimental research one automatically encounters different levels of gas (im)purity since two experimental setups are seldom completely the same, because of the different reactor designs and because not always the same quality grade gas is being used [8,175]. In simulations this purity level is sometimes derived from estimations [8,177] or sometimes used as a fitting parameter to match a fundamental parameter such as gas voltage to the experimental value [34] or match the experimental current profile [178]. Therefore, it is important to investigate the influence of different levels of impurity in order to obtain a more general insight in this matter.

It is well known that the charged particle densities in low temperature gas discharges are generally of the order of  $10^{16}$  -  $10^{17}$  particles per  $\text{m}^3$  [179]. This range is typical for both low and high pressure discharges. If a high purity grade feeding gas is being used, impurities of only ppm levels are present in the gas. When working at atmospheric pressure with an operating temperature of about 350 K, it can be estimated from the ideal gas law that the background gas has a density of about  $2.1 \times 10^{25} \text{ m}^{-3}$ . Considering that high purity gas is being used, an impurity of 1 ppm

will attain a density of about  $2.1 \times 10^{19} \text{ m}^{-3}$ . This is about two orders of magnitude higher than the charged particle densities and hence, can have a considerable influence on the discharge behavior.

In this chapter it will be shown that even at very low relative concentrations the impurities have a great influence on the composition of the atmospheric discharge. This will be discussed specifically for the ionic composition of an atmospheric helium plasma with nitrogen impurities. Moreover, it will be demonstrated how different levels of impurity have an influence on the electrical performance of the discharge. In this respect it will first be studied how the time profiles of the current and gap voltage are influenced. Subsequently, it is investigated how many charged species are produced in relation with the required amount of power for different impurity levels. Based on these studies we can obtain a clear understanding of the governing mechanisms.

## 5.2 Description of the simulations

### 5.2.1 Description of the model

All presented results are obtained with the fluid model presented in Chapter 2, Section 2.3. It is a two-dimensional fluid description included in the Plasimo modeling framework [180,57] and is based on the continuity equations for mass, momentum and electron energy coupled with solving the Poisson equation for the electric field. The model has already been successfully applied for the numerical simulations of discharge cells used in, among others, display technology [43], breakdown phenomena in fluorescent lamps [181], pulsed capillary discharges [182] and sputtering hollow cathode discharges [59]. More information on the physics and numerical methods used to solve these equations iteratively and time dependently can be found elsewhere [43,181].

### 5.2.2 Description of the chemistry

The chemistry considered in the model is slightly different from the chemistries used in Chapters 3 and 4, because it was chosen to stay very consistent with the chemical descriptions of DBDs in atmospheric helium of Mangolini and coworkers [8] and Golubovskii and coworkers [9], because the operating conditions are almost identical. Moreover, it was possible to base the description on a previous application of the same model to describe atmospheric pressure helium carried out by Brok and coworkers [165].

In this study we considered either pure helium or helium gas with a certain amount of nitrogen present. The modeled species are the background gases He and N<sub>2</sub>, the electrons, the ions He<sup>+</sup>, He<sub>2</sub><sup>+</sup>, N<sub>2</sub><sup>+</sup> and N<sub>4</sub><sup>+</sup>, the metastable helium atoms He<sub>m</sub><sup>\*</sup> and the helium excimers He<sub>2</sub><sup>\*</sup>. The ions N<sup>+</sup> and N<sub>3</sub><sup>+</sup> and the chemically related atomic N are not taken into account, for matters of simplicity. These species are of minor importance in the ionic composition of the atmospheric plasma, because N<sup>+</sup> is very quickly converted into N<sub>2</sub><sup>+</sup> through  $N^+ + N + He \rightarrow N_2^+ + He$  and the degradation of N<sub>3</sub><sup>+</sup> by  $N_3^+ + N \rightarrow N_2^+ + N_2$  is about 6.5 times faster [160] than the equivalent degradation reaction of N<sub>4</sub><sup>+</sup>, i.e.  $N_4^+ + N \rightarrow N^+ + 2N_2$ . Inclusion of these species would only lead to a possible amplification of the impurity effects. The energy dependent transport data and reaction coefficients of the electrons were calculated using Bolsig [183] and the transport data for the other species were obtained from literature [164,60]. The chemical reaction set used in the model is composed from publications on discharge modeling found in literature [158,9,8] and consists of 18 chemical reactions which are shown in Table 5.1 and an extra electron energy loss term [165] associated with the rotational and vibrational excitation of N<sub>2</sub>, which is calculated from the excitation rates to a rotational level at 0.02 eV and to two vibrational levels at 0.29 and 0.291 eV, as was also done in Chapter 4.

**Table 5.1:** Reactions included in the model with their reaction rate coefficients. The first three reaction rate coefficients are calculated using Bolsig. In reaction 16, M denotes a heavy collision partner and the destruction frequency is taken from Golubovskii and coworkers [9].

No.	Reaction	Rate Coeff.	Ref.
1	$e^- + He \rightarrow e^- + He_m^*$	$f(\sigma)$	[6]
2	$e^- + He \rightarrow 2 e^- + He^+$	$f(\sigma)$	[6]
3	$e^- + He_m^* \rightarrow 2 e^- + He^+$	$f(\sigma)$	[6]
4	$e^- + He_2^+ \rightarrow He_m^* + He$	$8.9 \times 10^{-9} (T_g/T_e)^{1.5} \text{ cm}^3 \text{ s}^{-1}$	[9]
5	$e^- + N_2^+ \rightarrow N + N \rightarrow N_2$	$4.8 \times 10^{-7} (T_g/T_e)^{0.5} \text{ cm}^3 \text{ s}^{-1}$	[9]
6	$e^- + N_4^+ \rightarrow N_2 + N_2$	$2 \times 10^{-6} (T_g/T_e)^{0.5} \text{ cm}^3 \text{ s}^{-1}$	[160]
7	$He^+ + 2 He \rightarrow He_2^+ + He$	$1.1 \times 10^{-31} \text{ cm}^6 \text{ s}^{-1}$	[9]
8	$He_2^+ + N_2 \rightarrow He_2^* + N_2^+$	$1.4 \times 10^{-9} \text{ cm}^3 \text{ s}^{-1}$	[9]
9	$N_2^+ + 2 N_2 \rightarrow N_4^+ + N_2$	$1.9 \times 10^{-29} \text{ cm}^6 \text{ s}^{-1}$	[161]
10	$N_2^+ + N_2 + He \rightarrow N_4^+ + He$	$1.9 \times 10^{-29} \text{ cm}^6 \text{ s}^{-1}$	[161]
11	$N_4^+ + N_2 \rightarrow N_2^+ + 2 N_2$	$2.5 \times 10^{-15} \text{ cm}^3 \text{ s}^{-1}$	[160]
12	$N_4^+ + He \rightarrow N_2^+ + N_2 + He$	$2.5 \times 10^{-15} \text{ cm}^3 \text{ s}^{-1}$	[160]
13	$He_m^* + 2 He \rightarrow He_2^* + He$	$2 \times 10^{-34} \text{ cm}^6 \text{ s}^{-1}$	[9]
14	$He_m^* + He_m^* \rightarrow He_2^+ + e^-$	$1.5 \times 10^{-9} \text{ cm}^3 \text{ s}^{-1}$	[9]
15	$He_m^* + N_2 \rightarrow He + N_2^+ + e^-$	$5 \times 10^{-11} \text{ cm}^3 \text{ s}^{-1}$	[9]
16	$He_2^* + M \rightarrow 2 He + M$	$10^{-4} \text{ s}^{-1}$	[9]
17	$He_2^* + He_2^* \rightarrow He_2^+ + 2 He + e^-$	$1.5 \times 10^{-9} \text{ cm}^3 \text{ s}^{-1}$	[9]
18	$He_2^* + N_2 \rightarrow 2 He + N_2^+ + e^-$	$3 \times 10^{-11} \text{ cm}^3 \text{ s}^{-1}$	[9]

### 5.2.3 Operating conditions and validation

The experimental setup under study is exactly the same as the one used by Mangolini and coworkers [8] and is very similar to the setup used in many other atmospheric pressure discharge investigations [14, 9, 34, 184, 176, 185] for the sake of comparison with experiment and other numerical investigations.

The configuration consists of 2 parallel electrodes both covered with alumina dielectrics ( $\epsilon_r = 9$ ) of 1 mm thickness. The distance between the dielectric surfaces is 5 mm. One electrode is kept at ground potential and at the other a sinusoidal voltage is applied with a frequency of 10 kHz and an amplitude of 2.6 kV. These conditions have been chosen as such, because they allow us to obtain discharge breakdown for every purity level under study.

In order to first validate our model an electric potential is applied on the powered electrode with a frequency of 10 kHz and an amplitude of 2 kV, which is exactly the same as used by Mangolini and coworkers [8]. In order to stay consistent with their research we used an impurity of 100 ppm of  $N_2$ , as they estimated from their setup analysis [8]. In figure 5.1 our calculated profiles for current, gap voltage and applied voltage are illustrated together with the experimental results of Mangolini. Very good agreement is obtained in the manifestation of a single narrow current peak with an amplitude of several mA/cm<sup>2</sup> every half period when the gap voltage reaches exactly the same value of 1.5 kV, as was also obtained by Mangolini [8]. For this configuration, however, it was not possible in the model to reach breakdown when no nitrogen impurities were present. On the other hand, periodic discharge behavior was successfully obtained in pure helium when an applied voltage amplitude of 2.6 kV or higher is used. This result confirms that the presence of nitrogen impurities in helium gas has a decreasing effect on the breakdown voltage [31].

## 5.3 Influence of the impurities

The range of impurity levels under consideration is based on literature. The reported range in literature is quite large with a bottom value of 0.5 ppm [34] and an upper value of 0.5% [184]. To our knowledge, all reported values of nitrogen impurities in atmospheric helium are always situated in this range. A very important effect of these impurity levels such as the influence on the breakdown voltage is more or less understood [31], but concerning the influence on the plasma composition, the reaction chemistry and the electrical consequences some questions remain unanswered. In this chapter we try to provide answers to these questions.

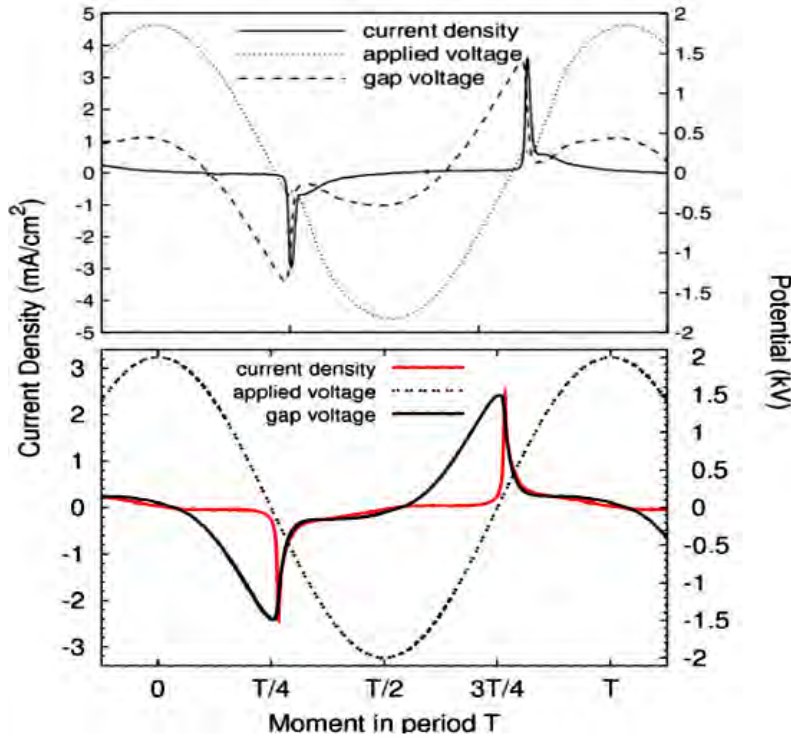


**Figure 5.1:** Top frame: Experimental results for the discharge current density, gap voltage and applied voltage as a function of time obtained by Mangolini and coworkers [8]. Bottom frame: Our calculated results using the same conditions (see text).

### 5.3.1 Influence on the composition

In order to illustrate the significant influence of even small amounts of impurity on the composition, the time and spatial average of the charged particle densities in the discharge are presented in figure 5.2 for impurity levels ranging from 0 to 5 ppm. First of all, note that the total positive ion density is about 10 to 20 % higher than the electron density. As is well known, this can be attributed to the spatial structure due to plasma sheath formation (cf. Chapter 1), since the sheath is positively charged and the plasma bulk is quasi neutral, the spatially averaged charge will be slightly positive. Moreover, both the total ion density and the electron density gradually rise with increasing  $N_2$  impurity level for the range shown in figure 5.2. The densities of  $He^+$  are omitted because these do not achieve values higher than  $5 \times 10^{13} \text{ m}^{-3}$ . It is also worth to mention that at the instant of maximum current the electron and ion densities in the plasma bulk and presheath are typically in the range from  $10^{16} \text{ m}^{-3}$  to  $6 \times 10^{17} \text{ m}^{-3}$ . This maximum value lies much higher than the values shown in figure 5.2, because the values in figure 5.2 are averaged in time and, as can be seen in figure 5.1, the APG DBD is a pulsed discharge. This range is

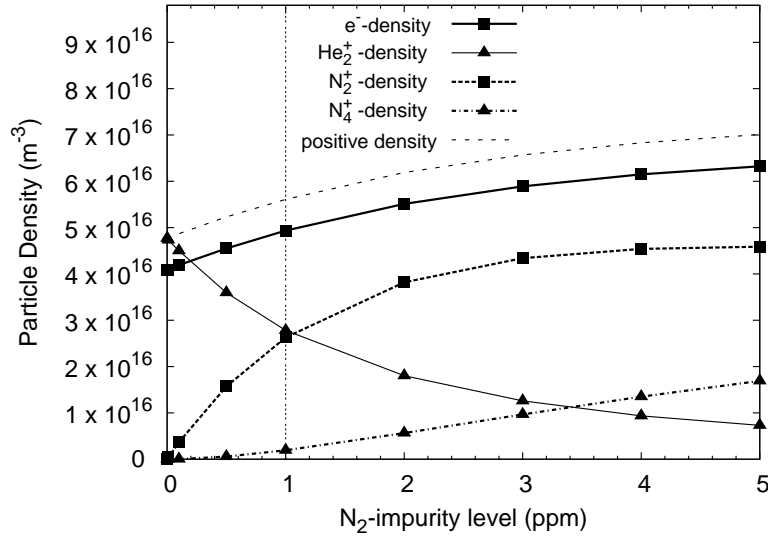


**Figure 5.2:** Calculated time and spatially averaged densities of the important charged particles in an atmospheric DBD in helium with different levels of N<sub>2</sub> impurity. The vertical dotted line indicates the boundary between the He<sub>2</sub><sup>+</sup> governed part and the N<sub>2</sub><sup>+</sup> governed part. The upper dotted curve indicates the sum of the positive ion densities.

in good agreement with the results of similar numerical studies reported in literature [14,9,8] which range from  $10^{16} \text{ m}^{-3}$  to  $5 \times 10^{17} \text{ m}^{-3}$ .

It is clear that only for discharges with less than 1 ppm of nitrogen impurity the positive charge is determined by the He<sub>2</sub><sup>+</sup> ions. Already at 1 ppm of nitrogen the time and spatially averaged densities of He<sub>2</sub><sup>+</sup> and N<sub>2</sub><sup>+</sup> ions are the same. At about 3.5 ppm of nitrogen also the N<sub>4</sub><sup>+</sup> ion density attains a value of the same magnitude as the He<sub>2</sub><sup>+</sup> ion densities. This proves that even small impurity levels have a great effect on the composition of the plasma, since already in the limited range of 0 to 5 ppm of nitrogen impurity, the He<sub>2</sub><sup>+</sup> densities drop from most important ion in the discharge to third-rate ion.

To investigate the effect of impurity levels higher than 5 ppm, the time and spatially averaged values of the charged particle densities are plotted in figure 5.3 for the entire range of impurity levels under study. Since the largest variations occur with the smallest impurity levels, we use a logarithmic scale for the nitrogen levels, ranging from the lowest non-zero value of 0.5 ppm to the highest value of 0.5%. Figure 5.3 shows that the He<sub>2</sub><sup>+</sup> density drops over the entire range when the relative level of nitrogen in helium gas increases. The He<sub>2</sub><sup>+</sup> ions become negligible in comparison with the nitrogen ions for impurity levels of about 17 ppm or higher. As indicated using Roman numerals and vertical dotted lines in figure 5.3 we divide the plot in four separate regions based on which ions are responsible for the positive

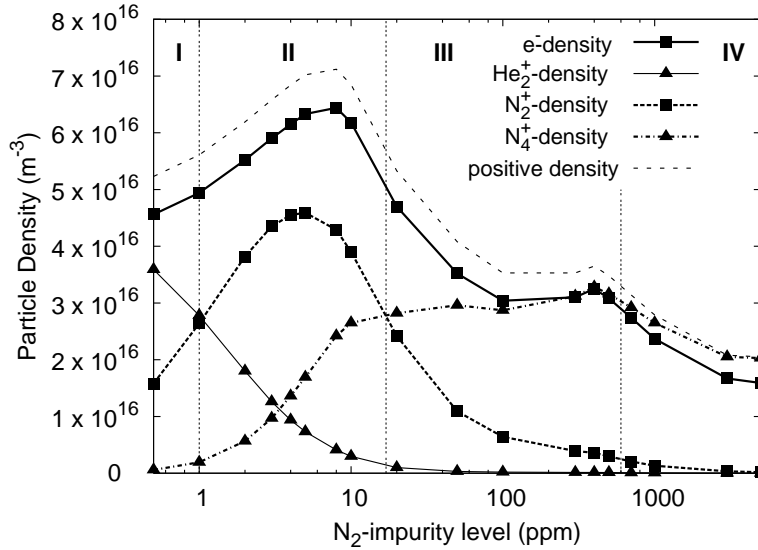


**Figure 5.3:** Calculated time and spatially averaged densities of the important charged particles in an atmospheric pressure helium DBD with nitrogen impurity levels ranging from 0.5 ppm to 0.5% . Region **I** denotes the  $\text{He}_2^+$  governed part, region **II** the  $\text{N}_2^+$  governed part, region **III** the  $\text{N}_4^+$  governed part with significant  $\text{N}_2^+$  contribution and region **IV** is completely governed by  $\text{N}_4^+$  ions.

charge.

The first region (indicated by **I**, shown fully in figure 5.2) ranges from zero to 1 ppm. In this region  $\text{He}_2^+$  is dominating the positive charge, while  $\text{N}_2^+$  has an important role, but it is still secondary.

The second region (indicated by **II**) ranges from 1 to about 17 ppm and shows two important features. First the ionization degree of the discharge gas reaches a time and spatially averaged maximum of about  $3 \times 10^{-9}$  at an impurity degree of 8 ppm. Secondly in this range the  $\text{N}_2^+$  ion determines the positive charge in the discharge, while  $\text{He}_2^+$  decreases in this region from a secondary role to almost negligible and  $\text{N}_4^+$  rises from an unimportant position to a secondary role in the discharge.

The third region (indicated by **III**) ranges from about 17 to about 600 ppm. The positive charge is now completely governed by the nitrogen ions and  $\text{N}_4^+$  has become the most important positive ion in the discharge. The  $\text{He}_2^+$  ion densities do not attain values higher than  $10^{15} \text{ m}^{-3}$  anymore. We have chosen to designate the boundary of the third region to 600 ppm, because for impurity levels higher than this value (i.e., region **IV**) the  $\text{N}_2^+$  densities also have become negligible and the positive charge is completely governed by the  $\text{N}_4^+$  ions.

### 5.3.2 Influence on the reaction rates

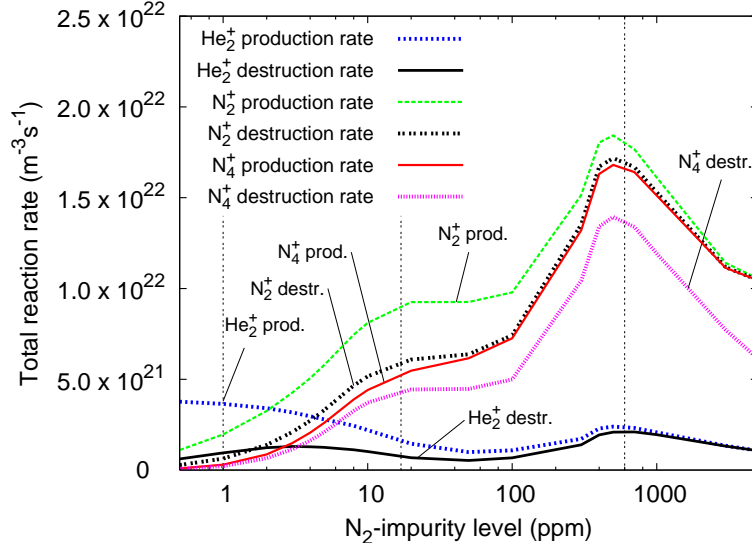


**Figure 5.4:** Calculated sum of total production and destruction rates for  $\text{He}_2^+$ ,  $\text{N}_2^+$  and  $\text{N}_4^+$ .

To provide more insight in the underlying mechanisms we plot in figure 5.4 the time and spatially averaged total production and destruction rates of the  $\text{He}_2^+$ ,  $\text{N}_2^+$  and  $\text{N}_4^+$  ions. Figure 5.4 shows that the reason for the decrease in  $\text{He}_2^+$  densities in the second region lies in the decrease of the production rate. Our calculations predict that the most important  $\text{He}_2^+$  production process at low  $\text{N}_2$  levels, namely the self-Penning ionization of  $\text{He}_2^*$  (reaction 17, table 5.1), becomes unimportant through the loss of  $\text{He}_2^*$  by its Penning ionization of  $\text{N}_2$  (reaction 18, table 5.1), since the time and spatially averaged density of  $\text{N}_2$  is at 5 ppm already about 150 times bigger than the  $\text{He}_2^*$  density and the ratio keeps increasing with rising  $\text{N}_2$  levels. This causes the drop in the  $\text{He}_2^+$  production from 0 to 50 ppm as shown in figure 5.4 and explains the decrease of the  $\text{He}_2^+$  density in region **II** in figure 5.3.

In region **II** in figure 5.3,  $\text{N}_2^+$  determines the positive charge, because the  $\text{He}_2^+$  density has already dropped significantly, for reasons mentioned above, and the  $\text{N}_2$  level is still relatively low. The production of  $\text{N}_2^+$  in the second region is for more than 80% determined by three reactions which are directly depending on the nitrogen partial pressure, namely the Penning ionizations of  $\text{N}_2$  by  $\text{He}_m$  and  $\text{He}_2^*$  and the charge exchange reaction of  $\text{He}_2^+$  with  $\text{N}_2$  (reactions 8, 15 and 18 in table 5.1). Also the destruction of  $\text{N}_2^+$  is directly influenced by the nitrogen partial pressure, since it is increasingly determined by the association of  $\text{N}_2^+$  with  $\text{N}_2$  and He as a third collision partner (reaction 10, table 5.1), which is responsible for about 50% of the

$N_2^+$  destruction at 1 ppm of nitrogen impurity and already for 87% at 17 ppm of  $N_2$ . Consequently, both the production and destruction rise significantly with increasing nitrogen content. However, since the above mentioned associative reaction is very fast ( $k = 1.9 \times 10^{-29} \text{ cm}^6 \text{ s}^{-1}$ ) and depends directly on both background gases, the conversion of  $N_2^+$  to  $N_4^+$  is increasingly promoted, which causes the  $N_2^+$  fraction in the discharge to decrease again.

Our calculations show that the production of  $N_4^+$  is almost completely determined by the associative collision of  $N_2^+$  with  $N_2$  with He as a third partner (reaction 10, table 5.1) for every impurity level. This reaction is directly related to the partial pressure of nitrogen. The destruction of  $N_4^+$  is completely governed by the dissociative electron recombination reaction (reaction 6, table 5.1) and the dissociative collision with He (reaction 12, table 5.1), which are not directly related to the partial pressure of nitrogen. Since the above mentioned  $N_4^+$  production reaction is directly related to the nitrogen content and the two destruction reactions are not directly related to the nitrogen content, the  $N_4^+$  fraction in the discharge always increases with rising nitrogen levels.

### 5.3.3 Influence on the electrical profiles

In order to demonstrate how the impurities influence the general electrical characteristics of the discharge, the calculated current density and the gap and applied voltage profiles are plotted in figure 5.5 for a pure He discharge, a He discharge containing 8, 100, 1000, 3850 and 4000 ppm of  $N_2$  impurity. Figure 5.5 illustrates that for a pure He discharge one narrow current peak with an amplitude of about  $2.5 \text{ mA/cm}^2$  is obtained in each half period. Increasing the  $N_2$  content with a few ppm leads to current pulses which are lower in amplitude, but last longer in time, so that the transferred charge remains about the same. This trend continues up to an impurity level of 8 ppm, where current pulses of only  $0.6 \text{ mA/cm}^2$  occur (see figure 5.5). A further increase of the  $N_2$  content in the discharge makes the breakdown stronger again. This causes the current amplitude to increase and the peakwidth to decrease again, which can be seen in figure 5.5, where the profiles at 100 ppm and 1000 ppm show current amplitudes of  $3 \text{ mA/cm}^2$  and  $11 \text{ mA/cm}^2$  respectively. Further increasing the  $N_2$  content in the discharge leads to multiple breakdown behavior. Indeed the additional  $N_2$  in the discharge stimulates Penning ionization, which facilitates volume ionization and hence, multiple breakdowns can occur with the same applied voltage [31]. Figure 5.5 illustrates a second breakdown at 3850 ppm and for 4000 ppm of  $N_2$  also a third breakdown occurs.

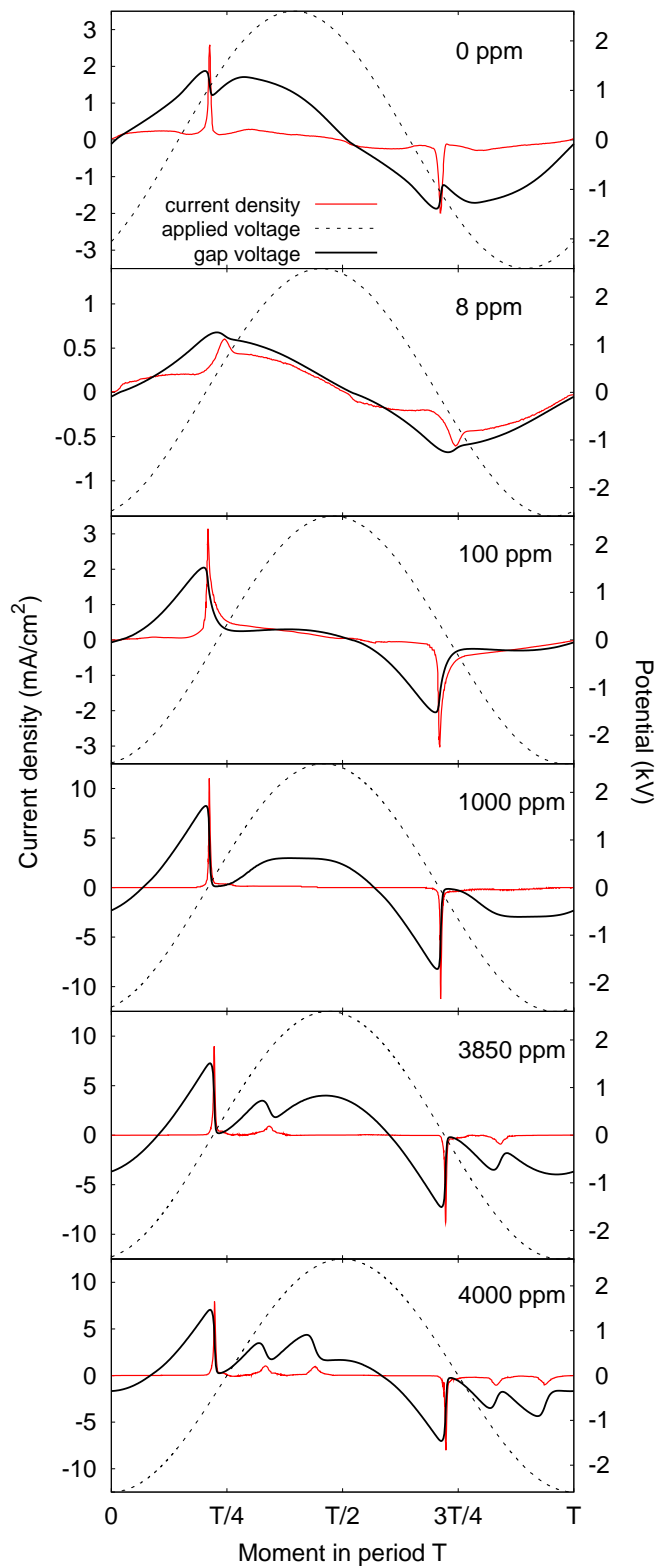


**Figure 5.5:** Calculated results for the discharge current density and gap voltage as a function of time, shown together with the applied voltage. Each frame corresponds with a different level of impurity.

### 5.3.4 Influence on the discharge performance

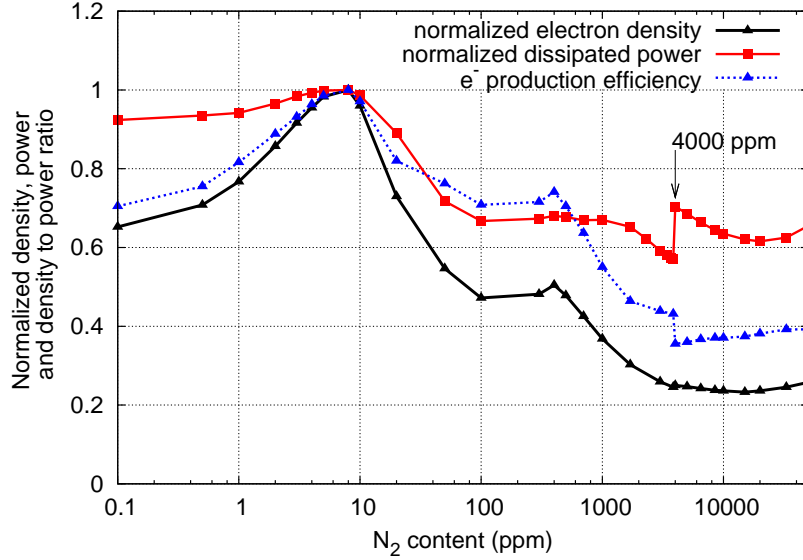


**Figure 5.6:** Normalized calculated electron density, dissipated power and electron production efficiency as a function of N<sub>2</sub> content.

These impurities also affect the performance of the discharge. Figure 5.6 illustrates the time and space averaged electron densities, dissipated power and the ratio of the electron density to the dissipated power as a function of N<sub>2</sub> content. All values are normalized to their highest value. For the electron density this value is  $6.4 \times 10^{16} \text{ m}^{-3}$ , for the dissipated power  $0.66 \text{ Wcm}^{-3}$  and their maximum ratio is  $9.7 \times 10^{10} \text{ W}^{-1}$ . The degree of ionization is very often a good indication of how active a plasma can be in, for example, dissociating molecules for plasma chemistry purposes. In the present description the electrons are the only negatively charged species. Therefore, their density is a direct measure for the degree of ionization. Figure 5.6 demonstrates that at a concentration of 8 ppm of N<sub>2</sub> in He the electron density is maximal and by increasing the N<sub>2</sub> concentration the electron density and therefore also the degree of ionization decrease. As a consequence, a high purity plasma will have a higher degree of ionization, although the calculated amplitude of the current density is lower (see figure 5.5). This is because the electron density value integrated in time is higher. Indeed, at low levels of N<sub>2</sub> there is much more continuous generation of charged particles during one period of applied voltage than with high levels of N<sub>2</sub>. This is reflected in the peak width of the current profiles in figure 5.5 and will be clarified later.

Figure 5.5 illustrates that increasing the N<sub>2</sub> content in the discharge can make

the discharge pulse stronger or weaker and can make it last longer or shorter. This behavior affects the power consumption of the discharge, which is determined by the volume integral  $\int_{vol} \bar{J} \cdot \bar{E} dV$ , where  $\bar{J}$  is the current density and  $\bar{E}$  the electric field calculated using Poisson's law  $\nabla \cdot (\epsilon \bar{E}) = \rho$ . Figure 5.6 illustrates that also the dissipated power is maximal at a  $N_2$  content of 8 ppm. For higher levels of  $N_2$  first the dissipated power drops and for levels of 100 ppm and higher it remains more or less constant, except for an anomaly at 3850 ppm. The dissipated power decreases more steeply between 1700 ppm and 3850 ppm, whereafter it jumps sharply to a much higher value at 4000 ppm. The reason for this will be discussed below.

The ratio of the electron density to the dissipated power provides for an indication whether a lot of energy is needed to obtain a certain degree of ionization. This ratio is illustrated in figure 5.6 and it also shows a very clear maximum at 8 ppm. For higher levels of  $N_2$  the ratio keeps decreasing, except for a very small bump at 400 ppm. After this the ratio decreases faster and has a very sharp drop at 3850 ppm, due to the steep jump of the dissipated power, which leads to the lowest density to power ratio. This shows that the discharge with the highest degree of ionization, composed of 8 ppm of  $N_2$  in He, also has the highest ratio of electron density to dissipated power and hence, is most efficiently dissipating this power to generate electrons.

### 5.3.5 Pulse shape analysis

Due to the pulsed nature of DBDs (cf. figures 5.1 and 5.5), the shape of the discharge current profiles is very often used to characterize the discharge. In this context we wish to obtain additional information on which types of profiles are responsible for the minima and maxima in electron density, dissipated power and density to power ratio plotted in figure 5.6. Therefore, the top frame of figure 5.7 illustrates the maximum value of the current density pulse together with its integrated value during the positive half of a period, which provides for the charge density on the electrode. In the bottom frame the ratio of this integrated value to the maximum current density is shown. We call this value the 'equivalent peak width', because it provides for the peak width in case the peak would have a rectangular shape. This is a good approximation when the current pulse is very narrow, as for 0, 100 and 1000 ppm of  $N_2$  in figure 5.5. However, it is merely an indicative value for deviating profiles, such as at 8 ppm of  $N_2$ , when the current profile is very flat and broad, thus there is not really a peak anymore. Also for  $N_2$  levels of 1700 ppm and up, the value is more an indication because secondary discharge pulses arise, as can be seen for 3850 ppm and 4000 ppm in figure 5.5. Therefore, in these situations the obtained value is not really a peak width, but it does provide valuable information whether the current profile is flat and broad or sharp and narrow.

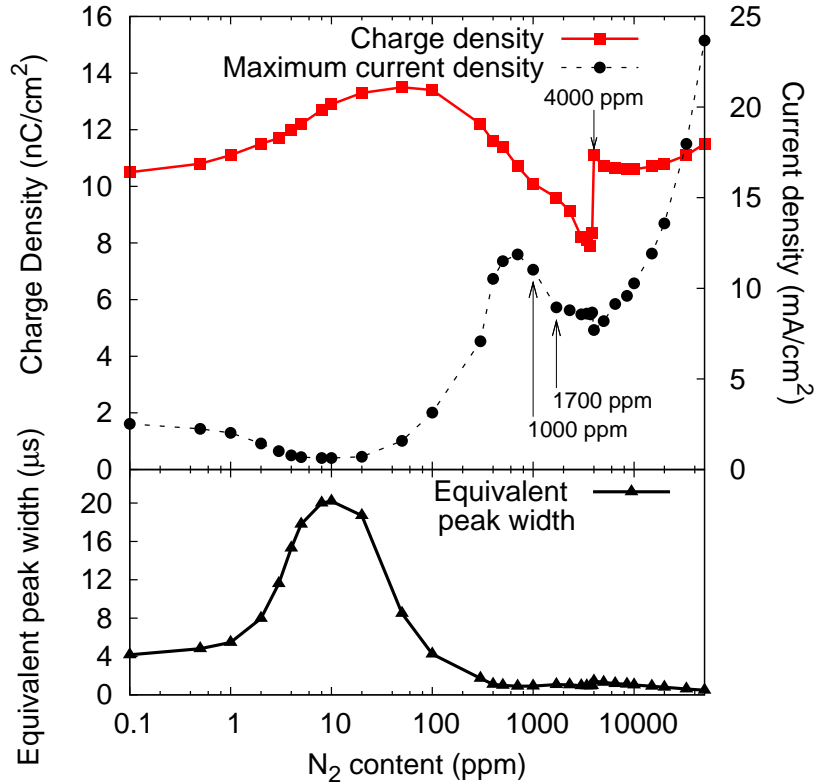


**Figure 5.7:** Top frame: Charge density transferred during the positive part of the current pulse and the maximum value of the discharge current as a function of the N<sub>2</sub> content. Bottom frame: Equivalent peak width determined by dividing the integrated positive part of the current pulse by the maximum value of the discharge current.

Figure 5.7 demonstrates that with 8 ppm of N<sub>2</sub>, which exhibited the highest ionization and efficiency in figure 5.6, the profile with the lowest maximum current density and the second largest peak width is obtained. This means that a very flat and broad current profile is associated with the highest degree of ionization and it is most efficiently using the dissipated power to ionize the gas. The performance of the typical narrow current pulses obtained with N<sub>2</sub> levels ranging from 100 to 1000 ppm, on the other hand, is only mediocre, as can be seen in figure 5.6.

### 5.3.6 The interplay between chemistry and electrics

The reason for the manifestation of narrow and broad current profiles does not lie in spatial variations, but in the time resolution of the ionization processes. Increas-

ing the  $N_2$  content in the discharge promotes the  $N_2$  depending ionization pathways. Detailed reaction analysis has shown that at very low impurity levels ( $< 3$  ppm) most electrons are produced by Penning ionization of  $He_2^*$  by  $He_2^*$  and by electron induced ionization of He, while at 3 ppm of  $N_2$  impurity the Penning ionization of  $N_2$  by  $He_2^*$  becomes the most important electron production reaction. This takeover is responsible for the increase in current peak width displayed in the bottom frame in figure 5.7. The peak width increases because the most important ionization reaction is determined by the  $He_2^*$  excimers and their densities do not change much in time, because they are not directly related to the electric field. As a consequence, also the rate of this Penning ionization does not change much in time. This provides for a more or less constant supply of charged species, which is responsible for the broad current profiles.

A further increase of  $N_2$  in the discharge causes Penning ionization of  $N_2$  by  $He_m^*$  to become very important. At 10 ppm of  $N_2$  it is already more important than the reactions depending solely on He. This reaction attains a narrow maximum right after gas breakdown, because it is determined by the  $He_m^*$  density, which is related to the electron energy via its production by the electron induced excitation of He. Because the electron energy is maximal at breakdown, the Penning ionization of  $N_2$  by  $He_m^*$  is maximal right after breakdown. A further increase of  $N_2$  also makes  $N_4^+$  the most important positive species in the discharge (cf. figure 5.3). As a consequence, the fast recombination of the electrons with  $N_4^+$  becomes very important. This process is most efficient when the electron energy is low (cf. reaction rate coefficient in Table 5.1), which occurs when the gap voltage is low. These last two processes cause that the ionization level becomes very high right after breakdown and that the electrons are quickly lost again due to recombination with  $N_4^+$ , which makes the current peaks narrow again.

The above processes are responsible for the transition region from about 2 to 50 ppm (cf. figure 5.7) in which the current profiles change from narrow to broad and back to narrow and where the  $N_2$  depending ionization rates become gradually more important than the rates depending solely on He.

The discontinuity in the dissipated power at 4000 ppm, as shown in figure 5.6, originates from a sudden change in the transferred charge on the electrode, which is displayed in figure 5.7. The discontinuity originates from the formation of a tertiary breakdown pulse. Indeed, it was demonstrated in figure 5.5 that for 3850 ppm of  $N_2$  there are two current pulses, while for 4000 ppm also a third pulse appeared. Analysis of the reaction chemistry and current profiles tells us that this tertiary discharge pulse is formed out of a tail of the previous current peak, which gradually transforms into a new current peak. Indeed, as the  $N_2$  content in the discharge increases, also the  $N_4^+$  concentration rises and consequently, the recombination of electrons with  $N_4^+$  right after the first current pulse eliminates the charge carriers faster and faster.

The elimination of charged species allows the gap voltage to increase again, because they are not able to compensate the governing electric field anymore by charging the dielectrics. This process is also responsible for the transition from one to two peaks, but because the  $N_2$  content and, hence, the  $N_4^+$  ion density are both still lower, the process is not yet so dominant. Hence, the transition occurs now gradually, explaining why for the formation of the secondary pulse no jump is observed in figure 5.6 and 5.7.

## 5.4 Conclusion

We have demonstrated in this chapter that the influence of common molecular impurities such as nitrogen in helium gas, is very important even at impurity levels of about 1 ppm. The calculations predict that the molecular  $N_4^+$  ion, which is often neglected in this kind of studies, becomes even the most important ion in the discharge, if the impurity level is higher than approximately 17 ppm. It was addressed how the chemical balances shift, which creates the different regions in figure 5.3, characterized by different dominating ions and it was explained how the  $N_4^+$  fraction in the discharge increases when the nitrogen level rises.

It was also shown how the impurities alter the electrical performance of the atmospheric He discharge. Increasing the impurity level changes the plasma chemistry, which affects the generation of charged particles and consequently, changes the electrical properties. Additionally, we have illustrated that not the narrow, intense current peaks, but the flat and broad current profiles prove to have the best gas ionization efficiency and power transfer to the discharge.



# Chapter 6

## The regime transitions during operation

### 6.1 Introduction

The atmospheric pressure dielectric barrier discharge (DBD) in helium is a pulsed discharge in nature. If during the electrical current pulse a glow discharge is reached, then this pulse will last only a few microseconds in operating periods of sinusoidal voltage with lengths of about 10 to 100 microseconds [14,9,8].

In this chapter it is demonstrated that right before a glow discharge is reached, the discharge very closely resembles the commonly assumed Townsend discharge structure [14], but actually contains some significant differing features and hence should not be considered as a Townsend discharge. In order to clarify this, calculation results are presented of high time and space resolution of the pulse formation. The results indicate that indeed a maximum of ionization is formed at the anode, but that the level of ionization remains high and that the electric field at that time is significantly disturbed. Our results also show where this intermediate structure comes from.

### 6.2 Operating modes in the atmospheric pressure DBD

The atmospheric pressure dielectric barrier discharge (DBD) can be operated in many different modes. The most common mode is the filamentary mode. Such discharge usually consists of many narrow discharge channels or filaments with diameters of about 200  $\mu\text{m}$ , which can be distributed randomly in space or can perform

self-organization in regular patterns with for example hexagon or square regularity [186]. Atmospheric DBDs can, however, also operate with a discharge homogeneously distributed over the electrode. In such case the discharge can be in Townsend mode, glow mode or an intermediate mode [13, 14, 9]. The Townsend mode is characterized by a very low space charge in the gap, so that the electric field is hardly disturbed, while there is only weak radiation near the anode. The glow mode is characterized by a similar structure as the low pressure glow discharges, with as most visible features a positive column, a Faraday dark space and a cathode glow with a clear maximum of radiation.

The dielectric barrier glow discharge is pulsed in nature, because the charged particles formed in the gas accumulate on the dielectrics, which causes the discharge to extinguish again [187, 30]. As a result, there is periodical breakdown and extinction behavior. This also allows that different types of applied voltage can be used, such as sinusoidal, rectangular or even pulsed DC voltages [188] (cf. Chapter 7).

The frequency at which these voltages are applied and the product of pressure with gap width ( $pd$ ) greatly determine the discharge characteristics. When using a low  $pd$  product ( $< 500$  Torr mm) and a high frequency of applied voltage ( $\geq 100$  kHz), a Townsend breakdown mechanism occurs leading to very regularly distributed filaments. Although filamentation occurs, still one current pulse each half period is observed. The mechanism has been studied in detail using two-dimensional simulations by Brauer and coworkers [187]. They demonstrate that even when neglecting plasma chemistry, gas heating and field emission effects, filamentation will still occur, which shows a direct dependency on the particle transport and the charging of the dielectric barriers.

When using a low  $pd$  product ( $< 500$  Torr mm) and a low frequency of applied voltage ( $< 100$  kHz), discharges are obtained with homogeneous distributions over the surface of the dielectric barriers. If on the gas gap a voltage is applied which is slightly above breakdown voltage, a discharge is obtained which produces regular current pulsations during each half period of applied voltage. Akishev and coworkers [189] have demonstrated using experiments and one-dimensional simulations that in this so-called multi-peak discharge the first current pulse corresponds with the gas breakdown and cathode sheath formation and that the following current pulses are the result of damped oscillations in the cathode sheath.

The use of a high  $pd$  product ( $\geq 500$  Torr mm) together with high frequencies ( $\geq 100$  kHz) in DBDs is limited. Increasing the applied frequency has the risk that the charge carriers in the discharge become too much trapped in the gas gap in order to guarantee stable behavior. This was demonstrated by Deng and Kong for atmospheric pressure DBDs in He and N<sub>2</sub> [32], where stability disruptions were observed when frequencies of 100 and 700 kHz for respectively He and N<sub>2</sub> were reached. Recently, however, Shi, Liu and Kong demonstrated that it is possible to

generate homogeneous, streamer-free discharges in an atmospheric pressure DBD at frequencies of 6.78 MHz and above [190,191]. This provides for a homogeneous discharge with higher current densities and higher ionization degree than both the rf discharge with naked electrodes and the low frequency DBD, but consequently the power consumption for this discharge is much higher than for the low frequency DBD, since at such high frequencies it is not a pulsed discharge anymore.

If a high  $pd$  product ( $\geq 500$  Torr mm) and a low frequency of applied voltage ( $< 100$  kHz) are being used, diffusive and homogeneous discharges can be obtained. These conditions correspond with the typical parameters for the atmospheric pressure DBD where mostly a gas gap of a few mm is being used. As mentioned above, such discharges can operate in Townsend, glow or an intermediate mode of which the pulsed character of the glow mode is very useful, since it greatly reduces the amount of power that is consumed, while still producing ion and electron densities of the order of  $10^{17} \text{ m}^{-3}$  [14,9,8]. In order to better understand the glow discharge formation in the discharges generated with a high  $pd$  product and a low frequency of applied voltage, we present in this chapter calculated results of high time and space resolution and present new information on the plasma structure during discharge pulse formation.

In the work of Massines and coworkers [17] it has been suggested and calculated that when the breakdown occurs, the electric field is uniform as in a Townsend discharge, so that the discharge actually transforms from a Townsend discharge into a glow discharge. Recently Luo and coworkers [185] demonstrated with high time resolution images of their glow discharge setup, that prior to the strong glow discharge radiation near the cathode, first a weak radiation near the anode occurs, which is typical for the Townsend discharge and confirms the results of Massines and coworkers. In this chapter it will be demonstrated that not a Townsend discharge is formed, but a subnormal discharge.

## 6.3 Description of the simulations

### 6.3.1 Description of model and chemistry

We make again use of the two-dimensional fluid model that was described in Chapter 2, Section 2.3, which is included in the PLASIMO [180,57] modeling framework. The model is based on numerically solving the continuity equations for mass, momentum and electron energy coupled with solving the Poisson equation for the electric field.

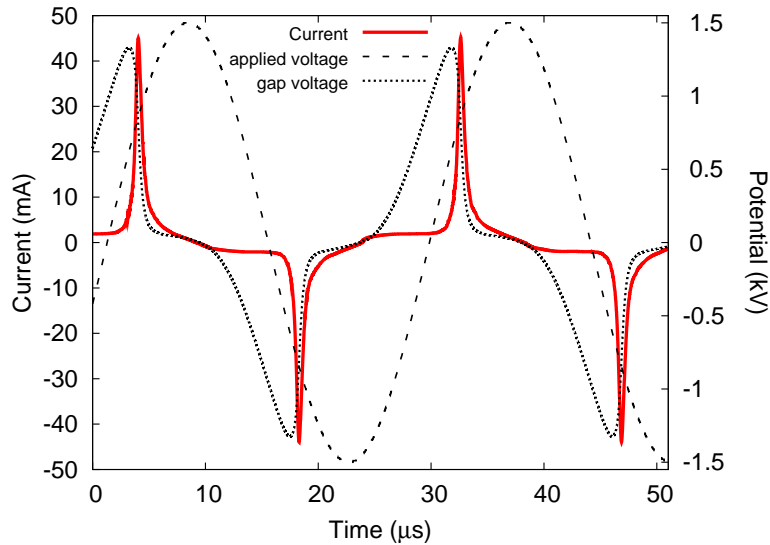
The described discharge gas is atmospheric pressure helium with some nitrogen impurities and it is described using 9 different species and 18 different chemical re-

actions of which the details are described in Chapter 5.

The setup under study is exactly the same as used by Luo and coworkers [185]. The reactor consists of two parallel electrodes covered with quartz dielectrics with a relative permittivity of 3.9 and a thickness of 1 mm. The gap between the surfaces of the dielectrics is 5 mm. One electrode is kept at ground potential, while on the other a sinusoidal potential with an amplitude of 1.5 kV and a frequency of 35 kHz is applied. For the discretization in time and space we used a maximum time step of 1 ns and a grid cell width of 25  $\mu\text{m}$ .

In order to obtain the best agreement with the measured electrical current profile, an impurity level of 300 ppm of  $\text{N}_2$  in He was used. Furthermore, the reaction rate coefficient that was reported in Chapter 5 for the  $\text{He}_2^*$  loss reaction  $\text{He}_2^* + \text{N}_2 \rightarrow 2\text{He} + \text{N}_2^+ + e^-$ , which is quite uncertain for this kind of discharge [9], was increased from  $3 \times 10^{-11} \text{ cm}^3 \text{ s}^{-1}$  to  $45 \times 10^{-11} \text{ cm}^3 \text{ s}^{-1}$  in order to improve the agreement with the experimental discharge current profile even more.

### 6.3.2 Validation of the model



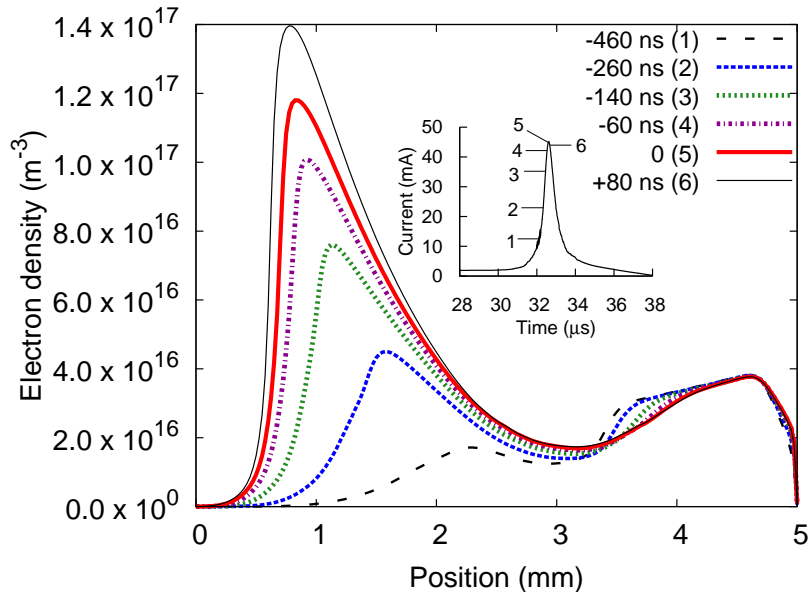
**Figure 6.1:** Calculated results for the discharge current and gap voltage as a function of time, shown together with the applied voltage.

Figure 6.1 illustrates our calculated discharge current profile as a function of time, as well as the applied voltage and calculated gap voltage. Our calculations predict one rise of a very narrow current peak each half of a period with an amplitude of 45 mA, assuming that the discharge is homogeneously distributed over

the 19.63 cm<sup>2</sup> large electrodes. This is in very good agreement with the measured results of Luo and coworkers [185], where also one narrow current peak each half of a period and a current amplitude of 45 mA was observed.

## 6.4 The regime transitions during operation

### 6.4.1 The charge and electric field distributions



**Figure 6.2:** Calculated electron density distributions at six different moments in time relative to the maximum of discharge current. The subfigure indicates the exact positions of these six moments in time on the discharge current peak.

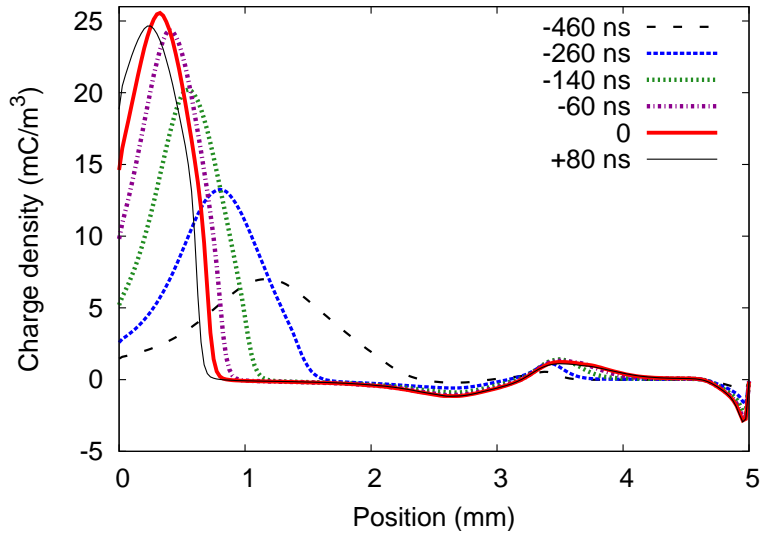
In order to demonstrate that the same anode-cathode behavior as in the experiment [185] is obtained, the spatial distributions of the electron density at six different moments in time are plotted in figure 6.2. These moments are at the maximum of discharge current (0 ns), as well as at 460, 260, 140 and 60 ns before the maximum of discharge current and at 80 ns after. Figure 6.2 also shows in a small subfigure the exact locations of these 6 moments in time on the discharge current peak. Note that the anode is located on the right and the cathode on the left in the figure. This provides an idea about the emission of light, since the maximum in electron density and the maximum in light emission are closely related [13,17]. The figure clearly illustrates that at 460 ns before the maximum of discharge current, the maximum

in electron density is located near the anode, which is indeed typical for a Townsend discharge [17]. As the charge builds up in the gap, the electron density starts to rise in the vicinity of the cathode. At 260 ns before the maximum of discharge current, the electron density near the cathode has already become higher than the value near the anode. Subsequently, the electron density near the cathode continues to rise, while the density near the anode remains the same, so that the typical glow discharge structure is formed.

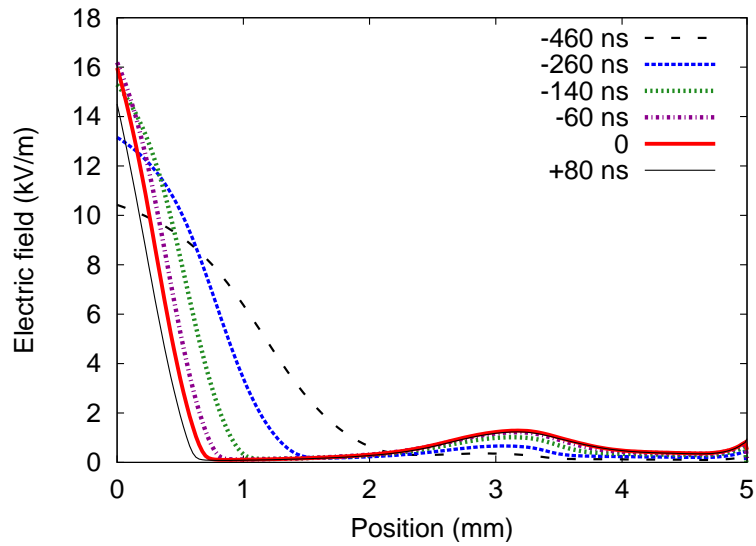
It appears also from figure 6.2 that the electron density has not yet attained its maximum value at the maximum of the current, but continues to rise even after the current pulse. The discharge does, however, extinguish itself by charging the dielectric barrier, so that the charged particles are redistributed and the negative and positive charges compensate each other. This is illustrated in figure 6.3, which displays the net charge density distributions across the gap at the same moments in time as in figure 6.2. It is clear that the maximum of discharge current coincides with the maximum in positive charge near the cathode. Consequently, when the current density drops, also the charge in the plasma sheath region decreases.

Figure 6.3 clearly demonstrates that at the instant of maximum current a discharge is obtained with a positively charged sheath at the cathode, together with only small disturbances in the bulk and a narrow negatively charged region near the anode. This is a structure typical for a glow discharge [18,13,1].

Furthermore, it is also observed that at 460 ns before the maximum of discharge current, the charge density in the gap is non-negligible. Note that a characteristic of Townsend discharges is that the ionization degree remains rather low and that the electron densities only attain maximum values of about  $10^{15} \text{ m}^{-3}$  [17,9]. However, at 460 ns before the instant of maximum current both the electrons and the positive ions have reached maximum values of about  $4 \times 10^{16} \text{ m}^{-3}$  in the gap. These values are not low for the conditions under investigation and they are able to disturb the electric field significantly. This refers to a second important characteristic of Townsend discharges, i.e., that the electric field is rather homogeneous and remains to have a high value across the discharge gap [13,185,17] (see Chapter 1, Section 1.3). In figure 6.4 the axial electric field component across the gap is depicted at the same moments in time as discussed above. At 460 ns before the maximum of discharge current the electric field is clearly disturbed by the present charges. This suggests that this regime should not be classified as a Townsend discharge, but as a subnormal glow discharge, because the maximum electron density is located at the anode and the glow discharge structure is not yet reached.



**Figure 6.3:** Calculated net charge density distributions at six different moments in time relative to the maximum of discharge current.



**Figure 6.4:** Calculated axial component of the electric field at six different moments in time relative to the maximum of discharge current.

### 6.4.2 The influence of the previous discharge pulse

It should be realized that at 460 ns before the instant of maximum current, the maximum of electron density is located at the anode because it is the remainder of the previous discharge pulse. In figure 6.5 the time evolution of the spatial profiles of the electron density is plotted. The evolution from one discharge pulse to the next discharge pulse at the opposite electrode is illustrated. It is clear that when the next discharge pulse is formed, a maximum in electron density appears and the discharge extinguishes itself again. As shown in figure 6.1, when the gap voltage reaches its maximum value again, i.e., the breakdown voltage, another breakdown occurs at the opposite electrode, which is clearly illustrated in figure 6.5. From figure 6.5 it can be qualitatively observed that right before this breakdown occurs, there is still a remainder of electrons of the previous pulse at the other electrode present. This causes the maximum in electron density at the anode at 460 ns before the maximum of discharge current.

In order to provide quantitative details on the amplitudes of the maxima in electron density, the positions of these maxima as well as their values from right before the pulse at the top electrode in figure 6.5 until the time of the pulse at the bottom electrode in figure 6.5 are plotted in figure 6.6. The full lines correspond with the first pulse and the dashed lines correspond with the second pulse. The red lines represent the positions of the maxima and the black lines their values. After the first pulse there remains an accumulation of electrons at the same spot which then gradually decreases until a value of about  $4 \times 10^{16} \text{ m}^{-3}$  at  $13.8 \mu\text{s}$ . This value corresponds with the local maximum near the anode, as shown in figure 6.2, which indeed demonstrates that the accumulation of electrons near the anode originates from the previous discharge pulse. The dashed lines in figure 6.6 illustrate that right after  $13.8 \mu\text{s}$  the density at the cathode has become higher than at the anode and that exactly the same starts to happen at the opposite electrode.

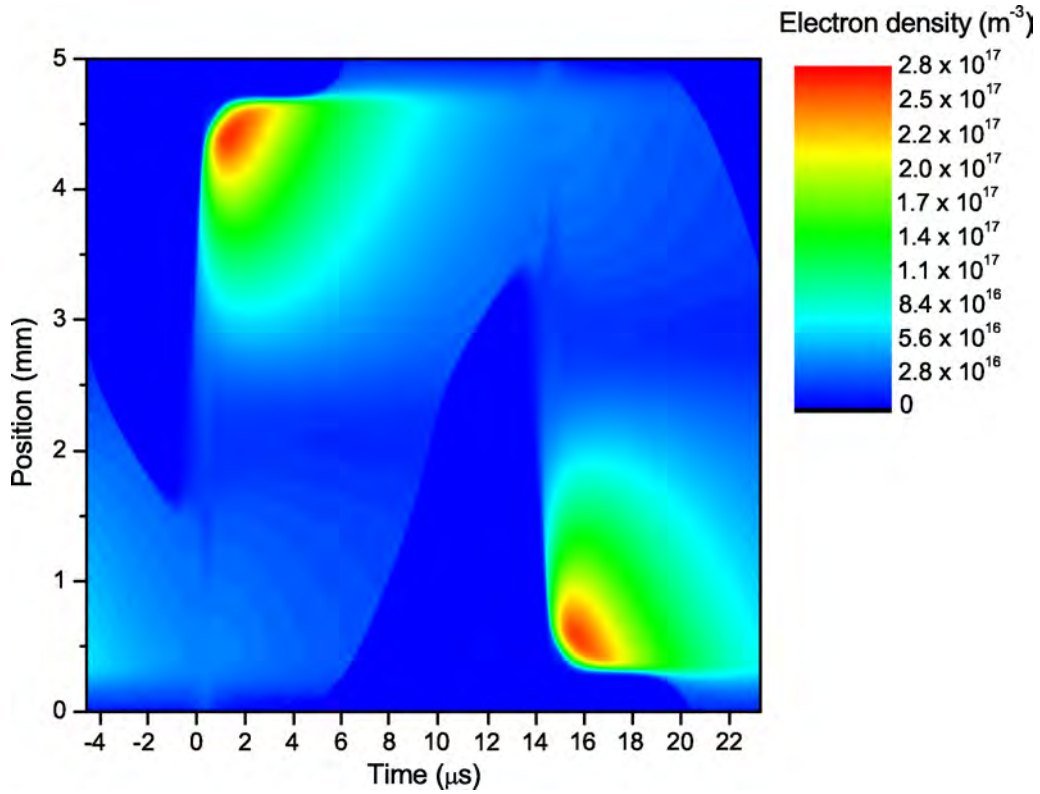


**Figure 6.5:** Calculated contour plot of the time evolution of the electron density distribution. At 0 and 14.26  $\mu\text{s}$  respectively the first and second maximum of discharge current occur.

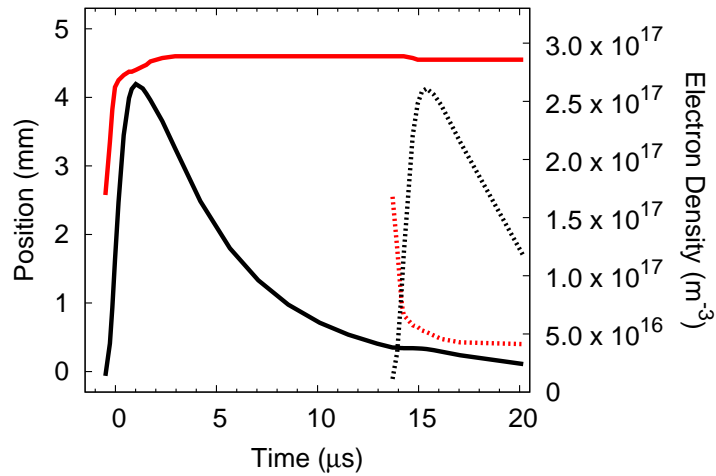


**Figure 6.6:** Calculated positions (red) and values (black) of the maximum electron density from the first pulse (full lines) and the second pulse (dashed lines) illustrated in figure 6.5. At 0 and 14.26  $\mu\text{s}$  respectively the first and second maximum of discharge current occur.

## 6.5 Conclusion

In this chapter it was demonstrated that the atmospheric pressure DBD in helium right before the discharge pulse is not in a Townsend mode, but it is a subnormal glow type of discharge, because the electric field is clearly distorted by the space charge. The maximum electron density, however, is located near the anode, but this accumulation of electrons is simply a result of the previous discharge pulse at the opposite electrode. We believe that the frequency of 35 kHz prevents the discharge to extinguish any further, so that the discharge always remains to be a glow or subnormal glow.

# Chapter 7

## The influence of the applied voltage profile

### 7.1 Introduction

The shape of the applied voltage profile is a crucial factor in generating cold atmospheric pressure plasmas [184]. When generating such plasmas a current limiting mechanism needs to be used. A very effective method is covering the electrodes with an insulating layer or dielectric. These dielectrics charge when the gas is ionized and hence, create an electric field compensating the original one and therefore quenching the discharge again [187], which keeps the temperature low. By charging the dielectric barriers, potential energy is stored on the surface. Different shapes of applied voltage profiles use this energy in a different way, which has an enormous influence on the power consumption of these dielectric barrier discharges (DBDs). In the present chapter we first compare four typical applied voltage profiles and investigate which has the best performance concerning electron production and power consumption. The applied profiles under study are a radio-frequency sine, a low frequency sine and rectangular and pulsed dc voltage profiles. In order to obtain a better understanding of the synergy between the power applied to the electrodes and the energy stored on the surfaces of the dielectric barriers we subsequently study the best performing setup in detail using calculated potential distributions of high time and space resolution.

### 7.2 Description of the simulations

We use again the same two-dimensional fluid model as presented in Chapter 2, Section 2.3 and used in the previous chapters.

The experimental setup under study is very similar to the setup used by Luo and coworkers [185] and is commonly used in atmospheric pressure discharge experiments [14, 9, 34, 184, 8, 176]. It is a DBD with both electrodes covered with an alumina dielectric ( $\epsilon_r = 9$ ) of 1 mm thickness. The spacing between the dielectric surfaces is 5 mm and on the top electrode a sinusoidal voltage is applied while the bottom electrode is grounded. The operating gas is atmospheric pressure helium with 100 ppm of nitrogen impurity and it is described using exactly the same nine different species and 18 different chemical reactions described in Chapter 5.

The validity of our model for this setup has previously been assessed by comparing the discharge current and gap voltage characteristics together with the spatial evolution of the discharge in time. In this way a very good agreement was obtained with the results of Mangolini and coworkers [8] in Chapter 5 and an almost perfect agreement was obtained with the results of Luo and coworkers [185] in Chapter 6.

### 7.3 Electrical characterization

In order to obtain a better insight in the electron generation and power consumption costs of different types of applied voltage profiles, four distinct setups were chosen which all interact very differently with the deposited charge on the dielectrics. Figure 7.1 illustrates the applied voltage and the calculated gap voltage and current density of the four voltage profiles. All setups use a 4 kV peak-to-peak voltage. Setup 1 is a radio-frequency (rf) discharge operating at 13.56 MHz, setup 2 a sinusoidal applied voltage at 10 kHz, setup 3 a rectangular voltage at 10 kHz and setup 4 is a pulsed dc discharge operating at 10 kHz. For the rectangular voltage and the pulsed dc discharge rise times of 50 ns are used. This value is based on the setups of Liu, Laroussi and Lu [192, 33, 193]. Note that the difference between setups 3 and 4 is that the rectangular voltage has both positive and negative values, whereas the pulsed dc discharge has only a positive applied voltage.

The rf setup (1) produces a very powerful discharge with a maximum current density of about 300 mA/cm<sup>2</sup>. The quenching effect of the charges accumulated on the dielectrics is very limited for this profile, because at such a high frequency the charged species are too much trapped in the discharge to quickly compensate the electric field before the polarity on the powered electrode has changed. As a consequence, an almost sinusoidal profile is obtained for the discharge current which is slightly more than one eighth of a period out of phase with the applied voltage. Indeed, due to the charges on the dielectric barriers the current profile is not one fourth of a period out of phase with the applied voltage, as for an rf discharge with bare electrodes [194].

The 10 kHz sinusoidal voltage (2) is the most typical profile for this kind of

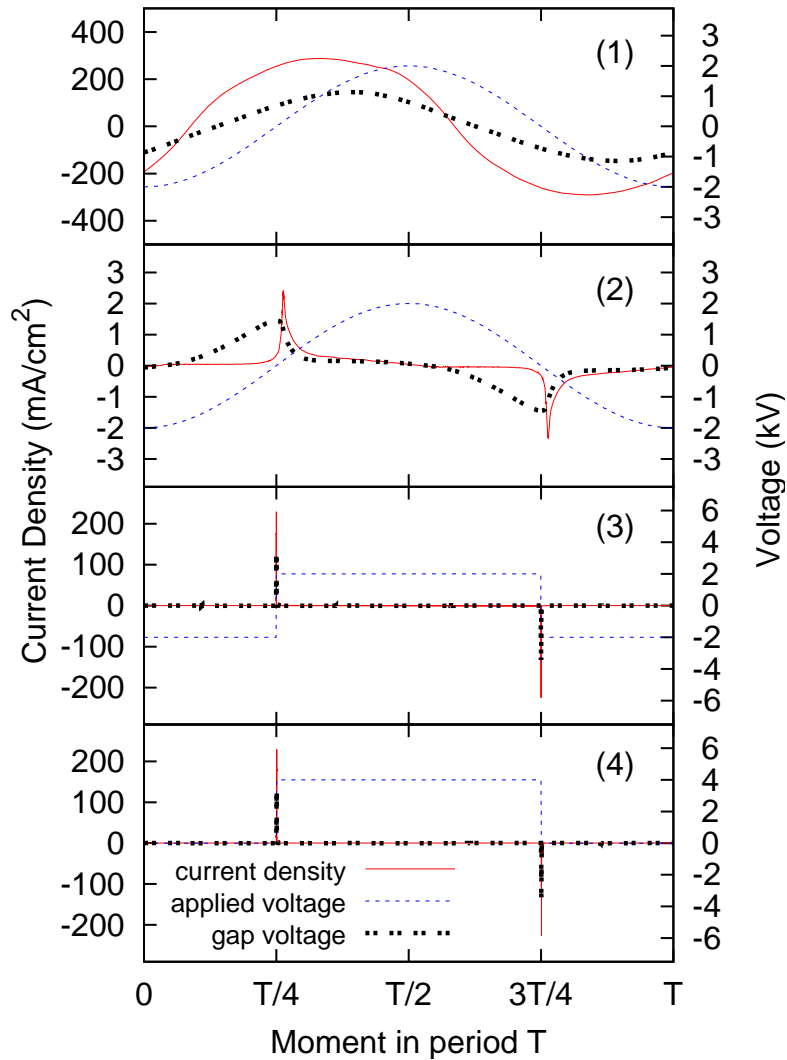


**Figure 7.1:** Calculated current density and gap voltage as well as applied voltage during one period of applied voltage. Setup (1) uses a rf voltage, (2) a 10 kHz sinusoidal profile, (3) a rectangular voltage and (4) a pulsed dc profile.

setup. It can be seen in fig. 7.1 that the gap voltage increases until a value of 1.5 kV is reached and then gas breakdown occurs, whereafter the discharge is quickly quenched again due to the accumulation of charges on the dielectrics. This creates a self-sustained pulsed discharge system, although powered by a continuous sinus, which is low in power consumption because it is a short current pulse, with an amplitude 100 times smaller than for the rf discharge [195].

Figure 7.1 demonstrates that generating a DBD plasma with a rectangular voltage (3) or with a pulsed DC profile (4) using frequencies of 10 kHz and peak-to-peak

voltages of 4 kV generates the same plasma which exhibits a current pulse of 230 mA/cm<sup>2</sup> right after a gap voltage of 3.4 kV is reached.

## 7.4 The efficiency of the setups

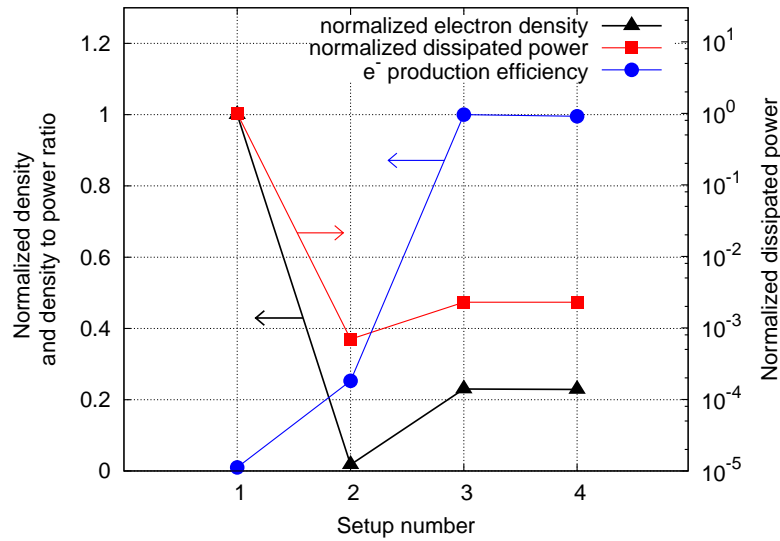


**Figure 7.2:** Normalized electron density, plasma power and electron production efficiency for the rf voltage (1), the 10 kHz sinusoidal voltage (2), rectangular (3) and pulsed dc voltage (4).

In order to assess the use of the different types of power supply an estimation for the power consumption is needed. The time averaged power dissipated in the discharge can be determined by  $\langle P_{diss} \rangle = (\int_T P_{diss} dt) / (\int_T dt)$  where  $T$  is the length of one period and  $P_{diss}$  is the dissipated power determined by  $P_{diss} = (\int_{vol} \vec{J} \cdot \vec{E} dV) / (\int_{vol} dV)$ , which is an integration over the volume of the product of plasma current density and electric field.

The calculated dissipated power of the four setups is plotted in figure 7.2 together with the time and space averaged electron density, as well as the ratio of this electron density to the dissipated power in order to obtain an idea of electron production efficiency. Since the focus lies on the comparison between the setups and in order to show all information in one plot, all values in figure 7.2 are normalized to their highest value. For the electron density this value is  $2.0 \times 10^{18} \text{ m}^{-3}$ , for the dissipated power  $517 \text{ Wcm}^{-3}$  and their maximum ratio is  $3.8 \times 10^9 \text{ W}^{-1}$ . The electron density and the electron production efficiency are plotted to the linear axis on

the left, while the dissipated power is plotted to the logarithmic axis on the right.

Figure 7.2 demonstrates that the rf discharge (1) very clearly has the highest electron production, but in comparison with the other setups requires an enormous amount of power, hence the logarithmic power scale. Due to this enormous power consumption, the rf discharge clearly has the lowest efficiency in the electron production. The other three setups all give rise to a discharge pulsed in nature, which can be seen in figure 7.1. Since the current in a pulsed discharge only flows for a limited amount of time, also the power consumption is limited in time. As a consequence, the dissipated power of setups 2, 3 and 4 is almost three orders of magnitude lower than for setup 1, as is illustrated in figure 7.2.

Figure 7.2 also shows that the efficiency of the rectangular profiles (3) and (4) is about four times higher than the sinusoidal profile. This increased efficiency is obtained because the rectangular voltage (3) and the pulsed dc voltage (4) are characterized by a change in the applied voltage on the electrodes during only 50 ns in half a period, which makes 100 ns in an entire period. A change of 4 kV during 50 ns provides for a voltage growth rate of  $8 \times 10^{10} \text{ Vs}^{-1}$ . This is about 300 times higher than the voltage growth rate at the point of breakdown when using a sinusoidal profile with an amplitude of 4 kV and a frequency of 10 kHz, i.e.,  $2.5 \times 10^8 \text{ Vs}^{-1}$ . As has been demonstrated by Golubovskii and coworkers [196], increasing the voltage growth rate in an atmospheric pressure DBD significantly increases the maximal current density and the space charge. Therefore, the rectangular profile (3) and the pulsed dc voltage (4) provide for a much higher electron density than the sinusoidal voltage (2), as can be seen in figure 7.2. Figure 7.2 also demonstrates that the increased pulse strength requires a greater amount of power, but the increased demand of power remains limited because the discharge pulse lasts only for 150 ns, while for the sinusoidal profile the discharge pulse lasts for  $6.05 \mu\text{s}$ , which is about 40 times longer. Therefore, the increased voltage growth rate, which causes the discharge pulse to be stronger, in combination with the restricted pulse width, which causes the power consumption to be limited in time, are responsible for the superior efficiency of the rectangular voltage (3) and the pulsed dc voltage (4).

Figure 7.2 illustrates that the same results are obtained for the rectangular voltage (3) and the pulsed dc discharge (4). It is indeed to be expected that the same discharge is obtained when the same peak-to-peak voltage is used in a DBD, because as can be seen in figure 7.1 due to the charge accumulation on the dielectrics, the same gap voltages are obtained. The real power consumption, however, will be different. Our model describes only the dissipated power calculated from the equations mentioned above. In order to obtain a full estimation of the power consumption, the supplied power needs to be calculated, i.e.,  $P_{supp} = (\int_{vol} I_{total} \cdot \phi_{app} dV) / (\int_{vol} dV)$ , where  $I_{total}$  is the total electric current and  $\phi_{app}$  is the applied potential [33]. The total electric current comprises the discharge current as well as the external current

flowing through the electrical circuit. Hence, to calculate the latter, a description of the electrical circuit is needed and this is currently not yet present in our model. An estimation, however, can be made, because the total current and the discharge current will always possess the same positive or negative sign [33].

Figure 7.1 demonstrates that for both setup 3 and 4 one positive and one negative current pulse is obtained within one period. The most important difference between setup 3 and 4 is that the rectangular applied voltage (3) has both positive and negative values, whereas the pulsed dc discharge (4) has only a positive applied voltage. Hence, for the rectangular voltage the supplied power in one period is determined by first a product of positive current and positive voltage and second by a product of negative current and negative voltage (setup 3, figure 7.1). Therefore, it gives twice a positive contribution for the supplied power. For the pulsed dc voltage, on the other hand, the supplied power in one period is determined by first a product of a positive current and a positive applied voltage and second by a product of a negative current and a positive voltage very quickly going to zero (setup 4, figure 7.1). Therefore, it is first a positive value, but the second contribution is a small negative value, because the second discharge pulse is generated simply by turning the power source off. This small negative value provides for a so-called power recuperation effect [33], which will always make the power consumption of the pulsed dc discharge (4) lower than for the rectangular voltage (3). Therefore, of all studied profiles the pulsed dc discharge will have the highest electron generation efficiency.

These calculations were not only carried out for the electron production efficiency, but also for the electron energy density. It is a good measure for the energy transfer to the discharge, because it is a combination of the energy used in order to generate electrons and the energy that is used to heat up the electrons. Using this parameter to assess the efficiency gave the same results.

## 7.5 The mechanism of the pulsed DC discharge

In order to obtain a better insight in the phenomenon of the secondary discharge pulse due to power deactivation (setup 4 figure 7.1) we have studied the origins of the discharge pulses by means of calculated potential distribution profiles of very high time and space resolution. The spatial emission behavior during these breakdown phenomena has been captured by Lu and Laroussi [188] by using a high speed ICCD camera. The images showed that for the first breakdown the plasma emission starts in the bulk region, while for the second breakdown this emission starts at the momentary anode and then moves towards the cathode.

In figures 7.3 and 7.4 the calculated spatial profiles of the electric potential throughout the discharge, including the dielectrics and electrodes are illustrated.

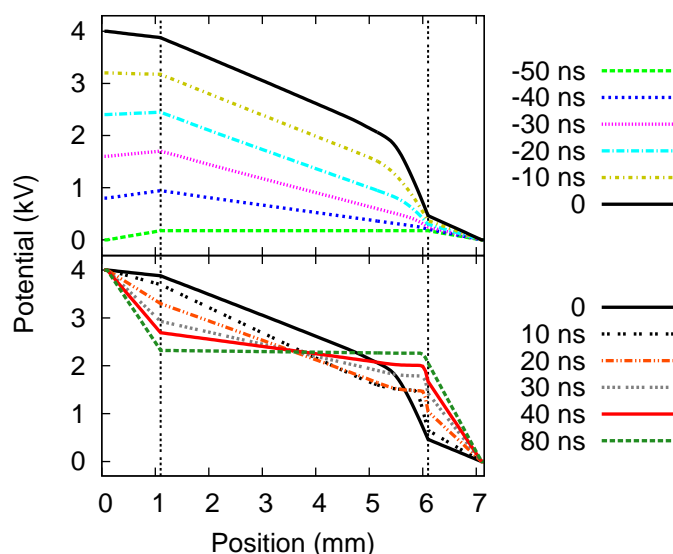


**Figure 7.3:** Spatial profiles of the calculated electric potential from the powered electrode on the left to the grounded electrode on the right. The vertical lines illustrate the surfaces of the dielectrics on the electrodes. The profiles are shown from 50 ns before the maximum gap voltage of 3.4 kV is reached (0), until 80 ns after the maximum gap voltage.

The powered electrode is on the left and the grounded electrode is on the right. In the top frame of figure 7.3 the transition is shown from zero gap voltage (-50 ns) evolving in six steps to maximum gap voltage (0). At that point there is breakdown in the gas and 20 ns later the maximum current density is reached. This very quick uprise in both current and charge density causes the ionized gas to charge both dielectrics. The latter compensates the potential difference between the electrodes so that the gap voltage gradually becomes zero again. The compensation of applied voltages by the surface charges is shown in the bottom frame of figure 7.3 in six consecutive profiles. Here it can be seen that although the potential difference between the electrodes is 4 kV, the difference between the dielectric surfaces becomes negligible within 80 ns. Afterwards a potential of about 2.2 kV is upheld at both dielectrics during 50  $\mu$ s. This is the potential energy that is stored on the surfaces.

Indeed, the potential distribution illustrated by the last profile in figure 7.3, at 80 ns after the maximum gap voltage, barely changes for about 50  $\mu$ s. Therefore, the difference with the first profile in figure 7.4, at 50 ns before the minimum gap voltage, is negligible. Figure 7.4 clarifies the creation of the secondary pulse. When the applied potential is set to zero on the powered electrode, the decrease of this potential pushes the potential on the adjacent dielectric downwards. Since there are still charges stored on the dielectric, the potential is pushed far below zero until

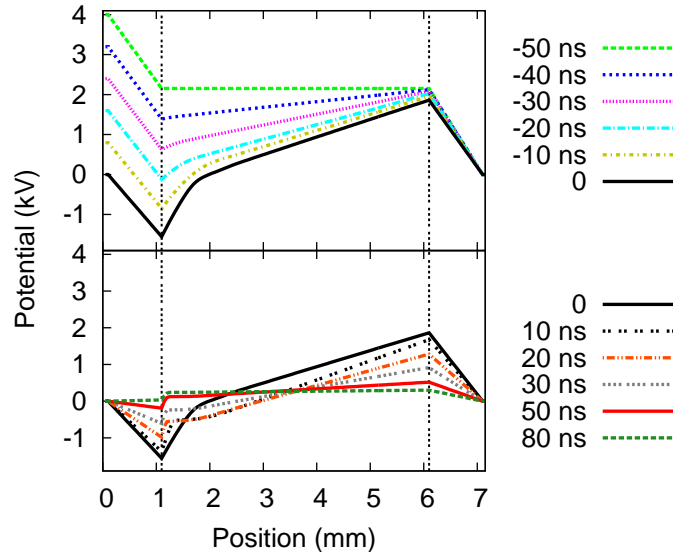


**Figure 7.4:** Similar profiles as in figure 7.3. The profiles are shown from 50 ns before the minimum gap voltage of  $-3.4$  kV is reached (0), until 80 ns after the minimum gap voltage. Note that the green dashed line in the upper frame ( $-50$  ns) has exactly the same shape as the green dashed line in the bottom frame of fig 3 ( $80$  ns), demonstrating that the potential distribution does not change for about 50 microseconds between the times of maximum and minimum gap voltage.

a value of  $-1.3$  kV is reached. The other electrode is grounded and therefore not much happens on the adjacent dielectric on whose surface a potential of about  $2$  kV is upheld. This creates a very large gap voltage and a second breakdown occurs. Hence, this explains the responsible mechanism for the secondary discharge pulse by deactivating the power supply. This mechanism can be followed in figure 7.4 where, similar as in figure 7.3, the spatial potential profiles are plotted. The top frame shows the profiles from zero gap voltage ( $-50$  ns) to maximum gap voltage (0) in six steps and the bottom frame illustrates the similar evolution from maximum gap voltage to a negligible gap voltage.

## 7.6 Conclusion

We have compared in this chapter four different voltage profiles in their capacity to generate electrons. It was shown that using rectangular voltages or pulsed dc voltages together with a DBD substantially increases the electron production efficiency. We have also demonstrated by means of spatial voltage profiles of high time and space resolution how deactivating the power source in a pulsed dc discharge

generates secondary discharge pulses. This mechanism is very important for future applications, because it causes that by using a pulsed dc power source together with a DBD a considerable reduction in energy cost can be obtained.



# Summary

Dielectric barrier discharges are already more than 150 years old. It is only during the last decades that the realization has grown that it is a remarkably good method to generate atmospheric pressure plasmas with highly energetic electrons in a background gas which is still near room temperature. This has created a boost in the number of new applications of these plasmas as gas conversion systems, surface modification setups, lighting sources and as ionization sources for spectrometry purposes. In order for these applications to be successful, the generated discharges need to be controllable and reliable and therefore they need to be well understood. Accurately measuring electron energy and electric potential has become very difficult for these setups, because the dimensions become too small. In such case numerical modeling of the plasma is indispensable to obtain detailed information. Moreover, using simulations specific parameters such as applied voltage, reflection coefficients or small changes in gas purity can be studied independently from the rest, which is experimentally almost never possible.

The research in this work consists of two separate parts. The first part contributes to the characterization of plasma sources which are used as an ionization or excitation source in order to do analytical spectrometry. The second part contributes to the general understanding of the operation of the classical atmospheric pressure dielectric barrier discharge setup.

The first ionization source that is characterized is a dielectric barrier discharge developed to be used as a microchip source for very small and portable analytical devices. It is operated with helium at pressures ranging from 10 to 180 mbar, however, the pressure range in which a merely stable discharge can be obtained appears to be much larger in our calculations, ranging from 15 to 1113 mbar.

The plasma source is operated with a rectangular potential in the kHz-range. This type of DBD is characterized by a dielectric layer on each of the electrodes. The dielectric constant and thickness of the dielectric determine the amount of displacement current that can be passed through the dielectric. In most applications, the dielectric limits the average current density in the gas space, which also limits

the operating power and it guarantees that no spark or arc can occur in the discharge gap.

In order to characterize the discharge first the evolution of the electrical potential in the discharge in time and space is calculated. The results show that the potential difference applied between both electrodes drops not only inside the plasma, but also across the dielectrics. Hence, the so-called gap voltage (or potential difference across the plasma) is clearly different from the applied voltage. It is the gap voltage, which determines the plasma characteristics. Consequently, the electrical current profile follows more closely the gap voltage profile than the applied voltage profile.

Beside the electrical characteristics also the spatial and temporal number density profiles of the various plasma species are calculated. It is found that, besides the He ground state atoms, the He atoms in metastable levels ( $\text{He}_m^*$ ) are the plasma species with the highest number density, with densities of at least an order of magnitude higher than the other plasma species densities. Moreover, the  $\text{He}_m^*$  atoms exhibit a different temporal behavior than the other plasma species. Indeed, the electrons, ions and  $\text{He}^{**}$  highly excited atoms reach a maximum density when the applied voltage switches polarity and their density drops again rapidly as a function of time. The  $\text{He}_m^*$  metastable atoms, on the other hand, exhibit a very slow decay as a function of time. Finally, the density of the  $\text{He}_2^*$  dimers appears to be roughly time-independent, but of lower importance than the other plasma species. This situation becomes different when the DBD is operated at higher pressures.

The following part of the microchip plasma source characterization deals with the influence of the background gas pressure. Our results show that for this configuration in the region from 50 to 140 mbar the plasma current density is three times as high as outside this pressure range and that the electrons, the ions and the excited species, except for the  $\text{He}_2^*$  excimers, also have a distinctly higher density. This shows that for pressures from 50 to 140 mbar there is a higher plasma activity. This appears to be in agreement with the typical operating conditions of 10 to 180 mbar used in the experimental investigations.

Our calculated stability range is, however, larger than 50 to 140 mbar. Stable discharges were obtained at pressures ranging from 15 to 1113 mbar. The lower pressure limit is due to the lack of background gas atoms available for collision in the discharge. The upper pressure limit is due to the loss of the electron energy in collisions with the background gas, resulting in too low electron energies to sustain the plasma.

In order to determine the discharge regime also the spatial distributions of the potential and the charge densities is investigated. For two very different cases glow-like profiles with distinct positively charged sheaths and quasi-neutral plasma bulks were obtained.

The high plasma activity in the pressure range from 50 to 140 mbar has been

---

found to be closely related to the Hornbeck-Molnar associative ionization reaction  $He^{**} + He \rightarrow He_2^+ + e^-$ . Our calculations show that this reaction clearly has the highest rate in the pressure range from 50 to 140 mbar. The two most important charge carriers  $He_2^+$  and the electrons are directly formed by this reaction and subsequently, these species determine the formation of the other plasma species. Therefore, the calculations show that, although  $He^{**}$  has a low density in the discharge, it is an important source for the governing Hornbeck-Molnar associative ionization.

The second analytical spectrometry ionization source that is characterized is a glow discharge maintained in atmospheric pressure He between a tubular cathode covered with electrical insulator at the sides and a rod-shaped anode. The anode was characterized by a conical end, which appeared to help in the experiments in stabilizing the discharge in the high-pressure regime for an electrode separation of 1 cm.

To describe the atmospheric pressure glow discharge, we make use of both fluid and Monte Carlo (MC) simulations. The MC calculations are used as an extra description for the non-equilibrium electrons.

From the potential distribution, as well as from the electron induced excitation rate profile, the different spatial regions in the discharge characteristic for a glow discharge can be distinguished. The positive column is dominating the discharge in agreement with the experimental observations. Electron impact ionization is only occurring near the cathode, i.e., in the energetic cathode dark space and negative glow regions and it becomes negligible at farther distances, when the electron energy has dropped to too low values. This is important to limit the amount of ionization and to prevent the transition into an arc discharge.

The  $He_2^+$  ions appear to be the dominant positive ions in the discharge. They are present in the entire discharge gap in contrast with the  $He^+$  ions, which are almost only observed near the cathode and anode. The  $N_2^+$  ion density is only slightly lower than the  $He_2^+$  and  $He^+$  ion densities, in spite of the much lower  $N_2$  density (i.e., assumed to be present as impurity of 10 ppm). This indicates that  $N_2$  gas molecules are more efficiently ionized, mainly by asymmetric charge transfer of  $He_2^+$  ions, as well as by Penning ionization due to  $He_m^*$  metastable atoms and  $He_2^*$  excimers. This suggests that the APGD has good potential as an ionization source for the analysis of gaseous compounds.

The second part of the research in this thesis contributes to the understanding of the classical atmospheric pressure dielectric barrier discharge in helium. The first investigation deals with the influence of impurities on the composition and on the electrical performance of the discharge. Understanding this influence is important, because in simulations it is used as an adjustable parameter to match the experimental data and since two experimental setups are seldom completely the same, one

automatically encounters different levels of gas purity. Therefore, it is important to obtain a more general insight in the effect of the impurities on the electrical behavior and the composition.

It is demonstrated that the influence of common molecular impurities such as nitrogen in helium gas, is very important even at impurity levels of about 1 ppm. The calculations predict that the molecular  $N_4^+$  ion, which is often neglected in this kind of studies, becomes even the most important ion in the discharge, if the impurity level is higher than approximately 17 ppm.

It is also addressed how the chemical balances shift, which makes that different ions become the principal positive charge carrier at different concentrations of  $N_2$ . The most important positive charge carrier below an  $N_2$  level of 1 ppm is  $He_2^+$ , from 1 to about 17 ppm is this  $N_2^+$  and for higher levels of  $N_2$  in the discharge is  $N_4^+$  the most important positive ion.

It is also demonstrated how increasing the impurity level changes the plasma chemistry, which affects the generation of charged particles and consequently, changes the electrical properties. This mechanism can be summarized as follows. The impurities change which chemical reaction contributes the most at a specific moment in time. This influence is directly responsible for the widening and narrowing of the current peaks and is indirectly responsible for the formation of secondary and tertiary current pulses.

Finally, efficiency analysis calculations show that not the narrow, intense current peaks, but the flat and broad current profiles prove to have the best gas ionization efficiency and power transfer to the discharge.

In the second fundamental atmospheric pressure dielectric barrier discharge investigation the regime transitions of this discharge are studied during the recurring gas breakdown. It is demonstrated that right before a glow discharge is reached, the discharge resembles very closely the commonly assumed Townsend discharge structure, but actually contains some significant differing features and hence should not be considered as a Townsend discharge. In order to clarify this, calculation results are presented of high time and space resolution of the pulse formation. The results indicate that indeed a maximum of ionization is formed at the anode, but that the level of ionization remains high and that the electric field at that time is significantly disturbed, which is a characteristic of a glow discharge.

It is also shown that the maximum electron density right before the discharge pulse, which is located near the anode and which is a characteristic of a Townsend discharge, is merely a concentration resulting from the previous discharge pulse at the opposite electrode. This illustrates that the frequency of 35 kHz prevents the discharge to extinguish any further, so that the discharge always remains to be a glow or subnormal glow.

---

The third fundamental investigation on the atmospheric pressure DBD concerns the influence of the shape of the applied voltage profile on the power consumption. The shape is a crucial factor, because the dielectrics covering the electrodes charge when the gas is ionized and hence, create an electric field compensating the original one and therefore quenching the discharge again.

By charging the dielectric barriers, potential energy is stored on the surface. Different shapes of applied voltage profile use this energy in a different way, which has an enormous influence on the power consumption of the DBD. In the present investigation first four typical applied voltage profiles are compared and it is investigated which has the best performance concerning electron production and power consumption. The applied profiles under study are a radio-frequency sine, a low frequency sine and rectangular and pulsed dc voltage profiles. In order to obtain a better understanding of the synergy between the power applied to the electrodes and the energy stored on the surfaces of the dielectric barriers we subsequently study the best performing setup in detail using calculated potential distributions of high time and space resolution.

The investigation shows that using rectangular voltages or pulsed dc voltages together with a DBD substantially increases the electron production efficiency. It is also demonstrated by means of spatial voltage profiles of high time and space resolution how deactivating the power source in a pulsed dc discharge generates secondary discharge pulses by using the charges that are stored on the dielectric barriers.

The research presented in this work mainly contributes to the understanding of plasmas at elevated pressures and in reactors where dielectrics are present. These dielectrics accumulate charges under influence of the plasma and generate an electric field of their own, which changes in its turn the plasma properties. The presented research contributes in the understanding of these mechanisms and can hopefully be the base for new or improved applications and technologies.



# Samenvatting

Diëlektrische barrière ontladingen (DBDs) zijn ondertussen al meer dan 150 jaar oud. Pas gedurende de afgelopen twintig jaar is het besef gegroeid dat het een opmerkelijk goede methode is om atmosferedrukplasma's te genereren met hoogenergetische elektronen, terwijl het achtergrondgas bij kamertemperatuur blijft. Dit inzicht heeft tot een enorme expansie gezorgd in de hoeveelheid nieuwe toepassingen van deze plasma's als gasomzettingssystemen, oppervlaktebehandelingsopstellingen, lichtbronnen en als ionisatiebronnen voor spectrometrie. Maar al deze toepassingen kunnen pas succesvol zijn als de ontladingen goed controleerbaar en betrouwbaar zijn en daarom is het onontbeerlijk dat hun werking goed begrepen is. Het meten van de elektronenenergie en de elektrische potentiaal met hoge precisie is erg moeilijk in deze opstellingen, omdat de dimensies zeer klein zijn. In zulk geval zijn numerische simulaties een uitzonderlijk handig hulpmiddel om gedetailleerde informatie over de ontlading te bekomen. Daarenboven is het door middel van simulaties mogelijk om specifieke parameters zoals de opgelegde spanning, reflectiecoëfficiënten of zeer kleine veranderingen in de zuiverheid van het gas onafhankelijk te bestuderen van de rest, wat experimenteel vrijwel nooit mogelijk is.

Het gepresenteerde onderzoek bestaat uit twee grote delen. Het eerste deel draagt bij tot de karakterisatie van plasmabronnen die gebruikt worden als ionisatie - of excitatiebron voor de analytische spectrometrie. Het tweede deel draagt bij tot het algemene begrip van de werking van de klassieke DBD-opstelling bij atmosferedruk.

De eerste ionisatiebron die gekarakteriseerd wordt is een DBD die ontwikkeld is om gebruikt te worden als een microchip-bron voor zeer kleine en draagbare analyse-apparaten. Het gebruikte plasma wordt typisch opgewekt in helium bij drukken die variëren van 10 tot 180 mbar.

Het plasma wordt opgewekt door gebruik te maken van een rechthoekige opgelegde spanning met een frequentie in het kHz-gebied. Bij dit type van DBD zijn allebei de elektrodes bedekt met een elektrische isolator. De diëlektrische constante en de dikte van de isolator bepalen de hoeveelheid van verplaatsingsstroom die door het diëlektricum kan passeren. Het diëlektricum beperkt de hoeveelheid aan gemiddelde

stroomdichtheid in de ontlading, met als gevolg dat ook het aandrijvingsvermogen beperkt blijft en dat er geen boogontlading of een vonk kan optreden in de ontladingsruimte.

Om deze ontlading te karakteriseren wordt eerst het plasma in detail bekeken dat bekomen wordt bij een druk van 80 mbar, wat pal in het typische werkingsgebied ligt van 10 tot 180 mbar. De eerste eigenschap die bekeken wordt is de evolutie van elektrische potentiaal berekend zowel in de ruimte als in de tijd. De resultaten tonen aan dat het potentiaalverschil tussen de elektrodes niet enkel een belangrijke val kennen in het plasma, maar dat ze ook een heel grote potentiaalval vertonen over het diëlektricum. Met als gevolg is het potentiaalverschil over de ontladingsruimte opmerkelijk verschillend van de opgelegde spanning. Het is wel het potentiaalverschil over de ontladingsruimte die in contact staat met het gas en deze bepaalt bijgevolg de eigenschappen van het plasma. Bijgevolg volgt de elektrische stroom veel meer het spanningsverschil over de ontladingsruimte dan deze tussen de elektrodes.

Naast de elektrische karakteristieken is ook de variatie in de ruimte en de tijd van de dichtheidsprofielen van de verschillende soorten deeltjes in het plasma. Deze berekeningen tonen aan dat naast het achtergrondgas He in de grondtoestand, de metastabiele He-atomen ( $\text{He}_m^*$ ) de plasmacomponent is met de hoogste dichtheid, met dichtheden die zeker een grootteorde groter zijn dan al de andere componentdichtheden. Daarenboven vertonen de  $\text{He}_m^*$ -dichtheden een verschillend verloop in de tijd dan de andere componentdichtheden. De elektronen, de ionen en de hoogaangeslagen  $\text{He}^{**}$  deeltjes bereiken een maximum op het moment dat de opgelegde spanning van polariteit verandert, waarna hun dichtheden weer snel sterk afnemen in de tijd. Daarnaast vertoont de dichtheid van de  $\text{He}_m^*$  metastabielen een zeer langzaam verval in de tijd. Tenslotte vertonen de dichtheden van de  $\text{He}_2^*$  dimeren een vrijwel tijdsafhankelijk gedrag en zijn deze opmerkelijk minder belangrijk in de ontlading dan de andere componenten. Deze situatie verandert sterk als de druk van het ontladingsgas wordt verhoogd.

De volgende stap in de karakterisatie van de microchip-bron betreft het onderzoek van de invloed van de druk van het achtergrondgas. De berekeningen tonen aan dat voor deze configuratie de stroomdichtheid in het plasma voor drukken van 50 tot 140 mbar drie keer zo hoog is dan voor al de andere drukken en dat de elektronen, de ionen en de geëxciteerde deeltjes, uitgezonderd de  $\text{He}_2^*$  excimeren, ook opmerkelijk hogere dichtheden vertonen. Dit toont aan dat voor drukken van 50 tot 140 mbar de plasma-activiteit aanzienlijk hoger ligt. Dit komt vrij goed overeen met het typische werkingsregime van 50 tot 140 mbar dat in het experimentele onderzoek wordt gebruikt.

Het stabiliteitsbereik dat in de berekeningen bekomen wordt is eigenlijk veel groter dan 50 tot 140 mbar. Stabiele ontladingen worden verkregen bij drukken gaande van 15 tot 1113 mbar. De limiet bij lage druk komt door het gebrek aan

---

achtergrondgasdeeltjes waarmee gebotst moet worden om de ontlading te kunnen onderhouden. De limiet bij hoge druk wordt veroorzaakt door het verlies aan elektronenenergie door te veel botsing met het achtergrondgas, wat er toe leidt dat er te weinig elektronenenergie overblijft om de ontlading te onderhouden.

Om het werkingsregime te bepalen worden de ruimtelijke verdelingen van de elektrische potentiaal en van de ladingsdichtheden onderzocht. Voor de twee uiterste gevallen met de hoogste en de laagste stroomdichtheid kan gezien worden dat structuren gelijkaardig aan de gloeiontlading verkregen worden, aangezien er duidelijk positief geladen sheaths zijn gevormd samen met een bulk die vrijwel neutraal van lading is.

De verhoogde activiteit van het plasma bij de drukken van 50 tot 140 mbar blijken sterk gerelateerd te zijn aan de Hornbeck-Molnar associatieve ionisatie  $He^{**} + He \rightarrow He_2^+ + e^-$ . De berekeningen tonen aan dat deze reactie duidelijk de hoogste reactiesnelheid heeft voor de drukken van 50 tot 140 mbar. De twee belangrijkste ladingsdragers  $He_2^+$  en de elektronen worden rechtstreeks gevormd door dit proces en bijgevolg bepalen ze de vorming van de andere plasmacomponenten. Hieruit blijkt dat hoewel  $He^{**}$  een lage dichtheid in de ontlading heeft, het wel een belangrijke bron is voor de bepalende Hornbeck-Molnar associatieve ionisatie.

The tweede ionisatiebron voor analytische spectrometrie die gekarakteriseerd wordt is een gloeiontlading die in atmosferisch helium wordt onderhouden tussen een tube-vormige cathode waarvan de zijkant volledig met elektrische isolator bedekt is en een vrij dikke staaf als anode. De anode is gekarakteriseerd door een conisch uiteinde dat in de experimenten erg belangrijk blijkt te zijn om de ontlading te kunnen stabiliseren bij zulke hoge druk met een interelektrode afstand van 1 cm.

Om de atmosferedruk gloeiontlading te beschrijven, maken we gebruik van zowel fluid als Monte Carlo (MC) simulaties. De MC berekeningen worden gebruikt om een extra en betere beschrijving te hebben van de elektronen die niet in evenwicht zijn met het elektrisch veld.

Zowel de berekende potentiaalverdelingen als de verdeling van de reactiesnelheid van de elektronen-geïnduceerde excitatie tonen aan dat de verschillende ruimtelijke onderverdelingen die typisch zijn voor een gloei-ontlading onderscheid kunnen worden. De positief geladen bulk domineert de ontlading in overeenstemming met de experimentele observaties. De elektronen-geïnduceerde ionisatie vindt enkel plaats naast de cathode, nl. in de erg energetische ‘cathode dark space’ en in de ‘negative glow’ en de reactie wordt verwaarloosbaar op grotere afstand waar de elektronenenergie te laag is geworden. Deze afname is erg belangrijk, aangezien dan de ionisatie beperkt blijft en de transitie naar een boogontlading vermeden wordt.

De  $He_2^+$  ionen blijken de dominante positieve ionen in de ontlading te zijn. Ze zijn belangrijk in de ganse ontladingsruimte in tegenstelling tot de  $He^+$  ionen, dewelke enkel naast de cathode en anode grote hoeveelheden hebben. De  $N_2^+$  ionendichtheid

ligt beetje onder de  $\text{He}_2^+$  en de  $\text{He}^+$  dichtheden, ondanks de zeer lage  $\text{N}_2$  dichtheid (beschouwd als een onzuiverheid van 10 ppm). Dit wijst erop dat de  $\text{N}_2$  gasmolekulen meer efficiënt geïoniseerd worden, voornamelijk door de asymmetrische ladingsoverdracht met de  $\text{He}_2^+$  ionen en de Penning ionisatie door  $\text{He}_m^*$  metastabielen en  $\text{He}_2^*$  excimeren. Dit wijst erop dat deze atmosferedruk gloeiontlading veel potentieel heeft om een goede ionisatiebron te zijn om gasvormige componenten te analyseren.

Het tweede deel in het onderzoek van deze thesis draagt bij tot het begrip van de klassieke DBD van atmosferisch helium. Het eerste onderzoek in dit kader betreft de invloed van onzuiverheden op de samenstelling en de elektrische performantie van de ontleding. Goed inzicht in deze invloed is belangrijk, aangezien dit een parameter is die in simulaties zeer vaak gebruikt wordt om overeenstemming te krijgen met de experimentele resultaten en aangezien twee experimentele opstellingen nooit hetzelfde zijn komt men automatisch verschillende niveau's van de zuiverheid van het gas tegen. Daarom is het erg belangrijk om een meer algemeen inzicht te krijgen in het effect van de onzuiverheden op de samenstelling en de elektrische karakteristieken.

Het wordt aangetoond dat de invloed van een courante onzuiverheid zoals stikstof in helium heel belangrijk is, zelfs bij niveau's rond de 1 ppm. De berekeningen wijzen erop dat het moleculaire  $\text{N}_4^+$  ion, dewelke erg vaak niet wordt beschouwd in dit soort studies, het meest belangrijke ion in de ontleding wordt, als het onzuiverheidsniveau hoger wordt dan ongeveer 17 ppm.

Daarnaast wordt er duidelijk gemaakt hoe de chemische evenwichten verschuiven zodat verschillende ionen de belangrijkste drager van positieve lading worden in het plasma bij verschillende concentraties van  $\text{N}_2$ . De belangrijkste drager van positieve lading bij onzuiverheden onder de 1 ppm van  $\text{N}_2$  is  $\text{He}_2^+$ , van 1 tot ongeveer 17 ppm is dit  $\text{N}_2^+$  en voor hogere niveau's aan  $\text{N}_2$  is  $\text{N}_4^+$  het belangrijkste ion.

De berekeningen tonen ook hoe een toename van de onzuiverheidsgraad de plasmachemie verandert, wat een invloed heeft op de aanmaak van geladen deeltjes en wat bijgevolg de elektrische eigenschappen verandert. Het mechanisme kan samengevat worden als volgt. De onzuiverheden veranderen welke chemische reactie het belangrijkste wordt op een bepaald moment in de tijd. Deze invloed is rechtstreeks verantwoordelijk voor het verbreden en versmallen van de stroompieken en is onrechtstreeks verantwoordelijk voor de vorming van de secundaire en tertiaire stroompieken.

Tenslotte toont een efficiëntie-analyse dat niet de smalle, intense stroompieken, maar de vlakke en brede profielen het meest efficiënt zijn in het ionizeren van het gas en de beste vermogensoverdracht naar de ontleding kennen.

In het tweede fundamentele onderzoek van de DBD bij atmosferedruk worden

---

de regime-overgangen van de ontlading bestudeerd tijdens de wederkerende gasdoorslag. Het wordt aangetoond dat net voordat de gloeiontlading wordt bereikt, de ontlading zeer sterk lijkt op de vaakst veronderstelde Townsend ontlading, maar dat de ontlading enkele belangrijke verschillen vertoont en daarom niet geclassificeerd mag worden als een Townsend ontlading. Om dit te verduidelijken zijn ruimtelijke profielen berekend van de belangrijkste parameters met hoge tijds - en ruimteresolutie tijdens de vorming van de puls. De resultaten tonen aan dat er inderdaad net voor de doorslag een ionisatiemaximum is aan de anode, maar dat dit ionisatieniveau relatief hoog blijft en dat bijgevolg het elektrisch veld op dat moment aanzienlijk verstoord is, wat net een eigenschap is van een gloeiontlading.

Het wordt eveneens aangetoond dat het maximum in elektronendichtheid net voor de ontladingspuls, dat zich aan de anode bevindt en wat een eigenschap is van de Townsend ontlading, slechts een resulterende concentratie is van de vorige ontladingspuls aan de tegengestelde elektrode. Dit toont aan dat de frequentie van 35 kHz verhindert dat de ontlading verder uitdooft, zodat de ontlading steeds een gloeiontlading is of een subnormale gloei.

Het derde fundamentele onderzoek van de DBD bij atmosferedruk betreft de invloed van de vorm van de opgelegde spanning op het verbruikte vermogen. Deze vorm is een zeer bepalende factor, aangezien de diëlektrica opgeladen worden wanneer het gas ioniseert en zodoende een elektrische veld genereren dat tegengesteld is aan het oorspronkelijke en bijgevolg de ontlading terug uitdooft.

Door het opladen van de diëlektrica wordt er ook potentiële energie op het oppervlak opgeslagen. Verschillende vormen van opgelegde spanning kunnen deze energie op een verschillende manier gebruiken, wat een enorme invloed heeft op het verbruikte vermogen. Het onderzoek vergelijkt eerst vier verschillende typische profielen van opgelegde spanning qua efficiëntie in het genereren van elektronen ten opzichte van het verbruikte vermogen. De onderzochte profielen zijn een radiofrequente sinus, een lage frequentie sinus en een rechthoekige en een gepulste gelijkstroom potentiaal. Om de synergie tussen de opgelegde spanning en de energie die opgeslagen is op de oppervlaktes van de diëlektrica beter te begrijpen wordt vervolgens de opstelling met de beste efficiëntie in detail bestudeerd door gebruik te maken van berekende potentiaalverdelingen met hoge tijds - en ruimteresolutie.

Het onderzoek toont aan dat het gebruik van rechthoekige potentiaalprofielen of gepulste gelijkstroomontladingen in combinatie met de DBD aanzienlijk de elektronenproductie-efficiëntie verhoogt. Het wordt eveneens aangetoond door gebruik te maken van ruimtelijke profielen van hoge tijds - en ruimteresolutie hoe het deactiveren van de stroombron in de gepulste gelijkstroomontlading secundaire ontladingspulsen genereert door de lading vrij te maken die opgeslagen was op het oppervlak van de diëlektrica.

Het gepresenteerde onderzoek draagt voornamelijk bij tot het inzicht in de chemische en fysische werking van plasmas bij gematigde en verhoogde drukken en in reactoren waar elektrische isolatoren in contact zijn met het plasma. Deze diëlektrica accumuleren ladingen op hun oppervlak onder invloed van het plasma, wat een eigen elektrisch veld genereert, wat op zijn beurt de plasmakarakteristieken weer verandert. Het gepresenteerde onderzoek draagt bij tot het inzicht in deze mechanismen en vormt hopelijk de basis voor nieuwe of verbeterde toepassingen en technologieën.

## Publications related to this work

1. **T. Martens**, A. Bogaerts, W.J.M. Brok, J.J.A.M. van der Mullen. Modeling study on the influence of the pressure on a dielectric barrier discharge microplasma. *J. Anal. Atom. Spectrom.*, 22(9):1003-1042, 2007.
2. **T. Martens**, A. Bogaerts, W.J.M. Brok, J. van Dijk. Computer simulations of a dielectric barrier discharge used for analytical spectrometry. *Anal. Bioanal. Chem.*, 388(8):1583-1594, 2007.
3. **T. Martens**, A. Bogaerts, W.J.M. Brok, J. van Dijk. The dominant role of impurities in the composition of high pressure noble gas plasmas. *Appl. Phys. Lett.*, 92(4):041504, 2008.
4. D. Petrović, **T. Martens**, J. van Dijk, W.J.M. Brok, A. Bogaerts. Modeling of a dielectric barrier discharge used as a flowing chemical reactor. *J. Phys. Conf. Ser.*, 133:012023, 2008.
5. **T. Martens**, W.J.M. Brok, J. van Dijk, A. Bogaerts. On the regime transitions during the formation of an atmospheric pressure dielectric barrier glow discharge. *J. Phys. D: Appl. Phys. Fast Track Comm.*, 42:122002, 2009.
6. **T. Martens**, D. Mihailova, J. van Dijk, and A. Bogaerts. Theoretical Characterization of an Atmospheric Pressure Glow Discharge Used for Analytical Spectrometry. *Anal. Chem.*, 81:9096-9108, 2009.
7. D. Petrović, **T. Martens**, J. van Dijk, W.J.M. Brok and A. Bogaerts. Fluid modelling of an atmospheric pressure dielectric barrier discharge in cylindrical geometry. *J. Phys. D: Appl. Phys.*, 42:205206, 2009.
8. **T. Martens**, W.J.M. Brok, J. van Dijk, A. Bogaerts. The influence of impurities on the performance of the dielectric barrier discharge. *Appl. Phys. Lett.*, 96(9):091501, 2010.
9. **T. Martens**, A. Bogaerts, J. van Dijk. Pulse shape influence on the atmospheric barrier discharge. *Appl. Phys. Lett.*, 96(13):131503, 2010.

10. S. Paulussen, B. Verheyde, X. Tu, C. De Bie, **T. Martens**, D. Petrović, A. Bogaerts and B. Sels. Plasma-assisted conversion of greenhouse gases to value-added chemicals. *Plasma Sources Sci. Technol.*, 2010, in press
11. A. Bogaerts, C. De Bie, M. Eckert, V. Georgieva, **T. Martens**, E. Neyts and S. Tinck. Modeling of the plasma chemistry and plasma-surface interactions in reactive plasmas. *Pure Appl. Chem.*, 2009, accepted for publication

# List of conference contributions

1. **T. Martens**, A. Bogaerts, W.J.M. Brok, J. van Dijk. Computer simulations of dielectric barrier discharges used for analytical spectrometry. *Poster presentation at the Plasma Winter Conference*, Taormina, Italy, February 2007.
2. **T. Martens**, A. Bogaerts, W.J.M. Brok, J.J.A.M. van der Mullen. Numerical simulations of atmospheric pressure dielectric barrier discharges in He with N<sub>2</sub> impurities at different operating conditions. *Poster presentation at the Meeting of the Belgian Physical Society en de Belgian Biophysical Society*, Antwerp, Belgium, May 2007.
3. **T. Martens**, A. Bogaerts. Modeling of atmospheric pressure dielectric barrier discharges in He with N<sub>2</sub> impurities. *Oral presentation at the 3<sup>rd</sup> International Congress on Cold Atmospheric Pressure Plasmas: Sources and Applications*, Ghent, Belgium, July 2007.
4. **T. Martens**, A. Bogaerts, W.J.M. Brok, J.J.A.M. van der Mullen. Numerical simulations of atmospheric pressure dielectric barrier discharges in He with N<sub>2</sub> impurities at different operating conditions. *Poster presentation at the XXVIII<sup>th</sup> International Conference on Phenomena in Ionized Gases*, Prague, Czech Republic, July 2007.
5. **T. Martens**, A. Bogaerts, W.J.M. Brok, J. van Dijk. De dominante rol van onzuiverheden in het chemisch evenwicht van atmosferische plasma's. *Oral presentation at the 9<sup>th</sup> Flemish Youth Conference on Chemistry*, Antwerp, Belgium, April 2008.
6. **T. Martens**, A. Bogaerts, W.J.M. Brok, J.J.A.M. van der Mullen. The Influence of impurities on the behavior of high pressure noble gas plasmas. *Poster presentation at the 19<sup>th</sup> Europhysics Conference on the Atomic and Molecular Physics of Ionized Gases*, Granada, Spain, July 2008.
7. C. De Bie, **T. Martens**, A. Bogaerts, W.J.M. Brok, J. van Dijk. Description of the detailed plasma chemistry of a DBD in a mixture of CH<sub>4</sub> and O<sub>2</sub> using a

- 2D fluid model. *Poster presentation at the 19<sup>th</sup> Europhysics Conference on the Atomic and Molecular Physics of Ionized Gases*, Granada, Spain, July 2008.
8. D. Petrović, **T. Martens**, A. Bogaerts, W.J.M. Brok, J. van Dijk. Numerical parameter study on a cylindrical DBD used as a chemical reactor. *Poster presentation at the 19<sup>th</sup> Europhysics Conference on the Atomic and Molecular Physics of Ionized Gases*, Granada, Spain, July 2008
  9. D. Petrović, **T. Martens**, J. van Dijk, W.J.M. Brok, A. Bogaerts. Modeling of a dielectric barrier discharge used as a flowing chemical reactor. *Invited oral presentation at the 24<sup>th</sup> Summer School and International Symposium on the Physics of Ionized Gases*, Novi Sad, Serbia, August 2008.
  10. **T. Martens**, A. Bogaerts, W.J.M. Brok, J. van Dijk. The influence of impurities on the electrical behavior of high pressure noble gas plasmas. *Poster presentation at the 61<sup>st</sup> Annual Gaseous Electronics Conference*, Dallas, USA, October 2008.
  11. **T. Martens**, D. Petrović, C. De Bie, A. Bogaerts, W.J.M. Brok, J. van Dijk. The gas conversion of methane with oxygen at atmospheric pressure using a cylindrical dielectric barrier discharge. *Oral presentation at the 61<sup>st</sup> Annual Gaseous Electronics Conference*, Dallas, USA, October 2008.
  12. C. De Bie, **T. Martens**, A. Bogaerts, W.J.M. Brok, J. van Dijk. Description of the plasma chemistry in an atmospheric pressure CH<sub>4</sub> dielectric barrier discharge using a two dimensional fluid model. *Oral presentation at the 4<sup>th</sup> International Congress on Cold Atmospheric Pressure Plasmas: Sources and Applications*, Ghent, Belgium, June 2009.
  13. D. Petrović, **T. Martens**, C. De Bie, J. van Dijk, W.J.M. Brok, A. Bogaerts. Numerical study on energy efficiency of a cylindrical dielectric barrier discharge plasma chemical reactor. *Oral presentation at the 4<sup>th</sup> International Congress on Cold Atmospheric Pressure Plasmas: Sources and Applications*, Ghent, Belgium, June 2009.
  14. **T. Martens**, W.J.M. Brok, J. van Dijk, A. Bogaerts. Improving dielectric barrier efficiency by optimizing voltage profiles. *Poster presentation at the 4<sup>th</sup> International Congress on Cold Atmospheric Pressure Plasmas: Sources and Applications*, Ghent, Belgium, June 2009.
  15. C. De Bie, **T. Martens**, A. Bogaerts, W.J.M. Brok, J. van Dijk. The plasma chemistry in an atmospheric pressure CH<sub>4</sub> dielectric barrier discharge described using a two dimensional fluid model. *Oral presentation at the 19<sup>th</sup>*

---

*International Symposium on Plasma Chemistry*, Bochum, Germany, July 2009,  
Best paper award finalists

16. **T. Martens**, W.J.M. Brok, J. van Dijk, A. Bogaerts. The influence of the voltage profiles on the efficiency of the dielectric barrier discharge. *Poster presentation at the 19<sup>th</sup> International Symposium on Plasma Chemistry*, Bochum, Germany, July 2009.
17. A. Bogaerts, C. De Bie, M. Eckert, V. Georgieva, **T. Martens**, E. Neyts and S. Tinck. Modeling of the plasma chemistry and plasma-surface interactions in reactive plasmas. *Invited oral presentation at the 19<sup>th</sup> International Symposium on Plasma Chemistry*, Bochum, Germany, July 2009.
18. A. Bogaerts, **T. Martens.**, C. De Bie, E. Bultinck, S. Tinck, F. Gou. Modeling of low-temperature plasmas: some case studies of different modeling approaches. *Invited oral presentation at the Workshop of the 62<sup>nd</sup> Gaseous Electronics Conference: Advances in the Kinetic Description of Low-Temperature Plasmas: Applications to Modeling and Simulation*, Saratoga Springs, USA, October 2009.
19. **T. Martens**, W.J.M. Brok, J. van Dijk, A. Bogaerts. Efficiently generating cold atmospheric plasmas. *Lecture at the 10th Flemish Youth Conference on Chemistry*, Blankenberge, Belgium, March 2010.
20. **T. Martens**, J. van Dijk, A. Bogaerts. Efficient use of the dielectric barrier discharge setup. *Lecture at the International Workshop on Diagnostics of Microplasmas*, Bochum, Germany, March 2010.



# Bibliography

- [1] M A Lieberman and A J Lichtenberg. *Principles of Plasma Discharges and Materials Processing*. John Wiley & Sons, Inc., Hoboken, New Jersey, second edition.
- [2] A Fridman. *Plasma Chemistry*. Cambridge University Press, New York, 2008.
- [3] H-E Wagner, R Brandenburg, K V Kozlov, A Sonnenfeld, P Michel, and J F Behnke. The barrier discharge: basic properties and applications to surface treatment. *Vacuum*, 71:417–436, 2003.
- [4] W Siemens. Ueber die elektrostatische induction und die verzögerung des stroms in flaschendrähnten. *Ann. Phys. Chem.*, 178(9):66–122, 1857.
- [5] <http://optics.phys.spbu.ru/golub/english/group.html>, accessed 27th of November 2009.
- [6] The Siglo Database, CPAT and Kinema Software, <http://www.siglo-kinema.com>.
- [7] R K Janev, W D Langer, D E Jr Post, and K Jr Evans. *Elementary processes in hydrogen-helium plasmas: Cross sections and reaction rate coefficients*. Springer-Verlag (Berlin, Heidelberg, New York), 1987.
- [8] L Mangolini, C Anderson, J Heberlein, and U Kortshagen. Effects of current limitation through the dielectric in atmospheric pressure glows in helium. *J. Phys. D: Appl. Phys.*, 37(7):1021–1030, 2004.
- [9] Y. B. Golubovskii, V. A. Maiorov, J. Behnke, and J. F. Behnke. Modelling of the homogeneous barrier discharge in helium at atmospheric pressure. *J. Phys. D: Appl. Phys.*, 36(1):39–49, 2003.
- [10] I Langmuir. The interaction of electron and positive ion space charges in cathode sheaths. *Phys. Rev.*, 33(6):954–989, 1929.
- [11] A Grill. *Cold Plasma in Materials Fabrication: from Fundamentals to Applications*. IEEE Press, New York, 1994.
- [12] F Paschen. Ueber die zum funkenübergang in luft, wasserstoff und kohlendioxid bei verschiedenen drucken erforderliche potentialdifferenz. *Ann. Phys.*, 273(5):69–96, 1889.

- [13] Y P Raizer. *Gas Discharge Physics*. Springer-Verlag, Berlin Heidelberg New York, 1991.
- [14] F Massines, A Rabehi, P Decomps, R B Gadri, P Ségur, and C Mayoux. Experimental and theoretical study of a glow discharge at atmospheric pressure controlled by dielectric barrier. *J. Appl. Phys.*, 83(6):2950–2957, 1998.
- [15] M Laroussi, I Alexeff, J P Richardson, and F F Dyer. The resistive barrier discharge. *IEEE Trans. Plasma Sci.*, 30(1):158–159, 2002.
- [16] D Staack, B Farouk, A Gutsol, and A Fridman. Dc normal glow discharges in atmospheric pressure atomic and molecular gases. *Plasma Sources Sci. Technol.*, 17:025013, 2008.
- [17] F Massines, P Ségur, N Gherardi, C Khamphan, and A Ricard. Physics and chemistry in a glow dielectric barrier discharge at atmospheric pressure: diagnostics and modelling. *Surf. Coat. Technol.*, 174:8–14, 2003.
- [18] B Chapman. *Glow discharge processes*. John Wiley & Sons Inc., New York, 1980.
- [19] F Massines, N Gherardi, N Naudé, and P Ségur. Recent advances in the understanding of homogeneous dielectric barrier discharges. *Eur. Phys. J. Appl. Phys.*, 47:22805, 2009.
- [20] D Šijačić. *Spatio-temporal pattern formation in a semiconductor-gas-discharge system*. PhD thesis, Technische Universiteit Eindhoven, 2004.
- [21] Y B Golubovskii, V A Maiorov, P Li, and M Lindmayer. Effect of the barrier material in a townsend barrier discharge in nitrogen at atmospheric pressure. *J. Phys. D: Appl. Phys.*, 39(8):1574–1583, 2006.
- [22] Yu B Golubovskii, V A Maiorov, J F Behnke, J Tepper, and M Lindmayer. Study of the homogeneous glow-like discharge in nitrogen at atmospheric pressure. *J. Phys. D: Appl. Phys.*, 37:1346–1356, 2004.
- [23] E Warburg. Über die ozonisierung des sauerstoffs durch stille elektrische entladugen. *Ann. Phys.*, 13(4):464–476, 1904.
- [24] M P Otto. L’ozone et ses applications. *Bull. Soc. Franc. Électr.*, 9(90):66, 1929.
- [25] H Becker. *Wiss. Veröff. Siemens-Konzern*, 1:76, 1920.
- [26] K Buss. Die elektrodenlose entladung nach messung mit dem kathodenszillographen. *Arch. Elektrotech.*, 26:261, 1932.
- [27] K G Donohoe. *The development and characterization of an atmospheric pressure non-equilibrium plasma chemical reactor*. PhD thesis, California Institute of Technology, 1976.

- 
- [28] S Okazaki, M Kogoma, M Uehara, and Y Kimura. Appearance of stable glow discharge in air, argon, oxygen and nitrogen at atmospheric pressure using a 50 hz source. *J. Phys. D: Appl. Phys.*, 26:889–892, 1993.
- [29] J R Roth, P P Tsai, C Liu M Laroussi, and P D Spence. One atmosphere, uniform glow discharge plasma. United States Patent US5414324, 1995.
- [30] F Massines. Décharge à barrière diélectrique pour le traitement de films. *Vide*, 56:55–65, 2001.
- [31] I Radu, R Bartnikas, and M R Wertheimer. Frequency and voltage dependence of glow and pseudoglow discharges in helium under atmospheric pressure. *IEEE Transactions on plasma science*, 31(6):1363–1378, 2003.
- [32] X.T. Deng and M.G. Kong. Frequency range of stable dielectric-barrier discharges in atmospheric He and N<sub>2</sub>. *IEEE Transactions on Plasma Science*, 32(4):1709–1715, 2004.
- [33] M Laroussi, X Lu, V Kolobov, and R Arslanbekov. Power consideration in the pulsed dielectric barrier discharge at atmospheric pressure. *J. Appl. Phys.*, 96(5):3028–3030, 2004.
- [34] X H Yuan and L L Raja. Role of trace impurities in large-volume noble gas atmospheric-pressure glow discharges. *Appl. Phys. Lett.*, 81(5):814–816, 2002.
- [35] E Aldea, P Peeters, H de Vries, and M C M van de Sanden. Atmospheric glow stabilization. do we need pre-ionization? *Surf. Coat. Technol.*, 200:46–50, 2005.
- [36] E Aldea, J B Bouwstra, M C M Van de Sanden, and H W De Vries. Method and apparatus for stabilizing a glow discharge plasma under atmospheric conditions. European Patent EP1697961, 2006.
- [37] U Kogelschatz. Dielectric-barrier discharges: Their history, discharge physics and industrial applications. *Plasma Chem. Plasma P.*, 23(1):1–46, 2003.
- [38] B Eliasson, M Hirth, and U Kogelschatz. Ozone synthesis from oxygen in dielectric barrier discharges. *J. Phys. D: Appl. Phys.*, 20:1421–1437, 1987.
- [39] L M Zhou, B Xue, U Kogelschatz, and B Eliasson. Partial oxidation of methane to methanol with oxygen or air in a nonequilibrium discharge plasma. *Plasma Chem. Plasma Process.*, 18(3):375–393, 1998.
- [40] O Goossens, E Dekempeneer, D Vangeneugden, R Van de Leest, and C Leys. Application of atmospheric pressure dielectric barrier discharges in deposition, cleaning and activation. *Surf. Coat. Technol.*, 142:474–481, 2001.
- [41] K Yasui, M Kuzumoto, S Ogawa, M Tanaka, and S Yagi. Silent-discharge excited tem<sub>00</sub> 2.5 kw co<sub>2</sub> laser. *IEEE J. Quant. Electron.*, 25(4):836–840, 1989.

- [42] X Xu. Dielectric barrier discharge - properties and applications. *Thin Solid Films*, 30:237–242, 2001.
- [43] G Hagelaar. *Modeling of microdischarges for display technology*. PhD thesis, Technical University of Eindhoven, 2000. (<http://alexandria.tue.nl/extra2/200013466.pdf>).
- [44] M Miclea, K Kunze, G Musa, J Franzke, and K Niemax. The dielectric barrier discharge – a powerful microchip plasma for diode laser spectrometry. *Spectrochim. Acta: Part B*, 56:37–43, 2001.
- [45] F A Haas and N St J Braithwaite. Simple analysis of a capacitive discharge with a bi-maxwellian electron distribution. *Plasma Sources Sci. Technol.*, 9:77–81, 2000.
- [46] W J M Brok. *Modelling of Transient Phenomena in Gas Discharges*. PhD thesis, Technical University of Eindhoven, 2005.
- [47] T J M Boyd and J J Sanderson. *Plasma Dynamics*. Thomas Nelson and Sons Ltd London, 1969.
- [48] T J Sommerer, W N G Hitchon, R E P Harvey, and J E Lawler. Self-consistent kinetic calculations of helium rf glow-discharges. *Physical Review A*, 43(8):4452–4472, 1991.
- [49] G J M Hagelaar and L C Pitchford. Solving the boltzmann equation to obtain electron transport coefficients and rate coefficients for fluid models. *Plasma Sources Sci. Technol.*, 14:722–733, 2005.
- [50] E Neyts. *Mathematical Simulation of the Deposition of Diamond-like carbon (DLC) Films*. PhD thesis, University of Antwerp, 2006.
- [51] J-P Boeuf. Numerical model of rf glow discharges. *Phys. Rev. A*, 36(6):2782–2792, 1987.
- [52] D Passchier. *Numerical fluid models for RF discharges*. PhD thesis, University of Utrecht, 1994.
- [53] I Kolev. *Particle-in-cell-Monte Carlo Collisions Simulations for a Direct Current Planar Magnetron Discharge*. PhD thesis, University of Antwerp, 2007.
- [54] E Bultinck. *Numerical simulation of a magnetron discharge utilized for the reactive sputter deposition of titanium nitride and oxide layers*. PhD thesis, University of Antwerp, 2009.
- [55] A Bogaerts. *Mathematical modeling of a direct current glow discharge in argon*. PhD thesis, University of Antwerp, 1996.
- [56] J van Dijk. *Modelling of Plasma Light Sources - an object-oriented approach*. PhD thesis, Technical University of Eindhoven, 2001.

- 
- [57] <http://plasimo.phys.tue.nl>.
- [58] A Salabaş. *Fluid model for charged particle transport in capacitively coupled radio-frequency discharges*. PhD thesis, Technical University of Lisbon, 2003.
- [59] D Mihailova, M Grozeva, G J M Hagelaar, J van Dijk, W J M Brok, and J J A M van der Mullen. A flexible platform for simulations of sputtering hollow cathode discharges for laser applications. *J. Phys. D: Appl. Phys.*, 41:245202, 2008.
- [60] H W Ellis, R Y Pai, E W McDaniel, E A Mason, and L A Viehland. Transport properties of gaseous ions over a wide energy range. *At. Data Nucl. Data Tables*, 17:177–210, 1976.
- [61] H W Ellis, M G Thackston, E W McDaniel, and E A Mason. Transport properties of gaseous ions over a wide energy range. part iii. *At. Data Nucl. Data Tables*, 31(1):113–151, 1984.
- [62] S Patankar. *Numerical Heat Transfer and Fluid Flow*. McGraw-Hill, New York, 1980.
- [63] J C T Eijkel, H Stoeri, and A Manz. An atmospheric pressure dc glow discharge on a microchip and its application as a molecular emission detector. *J. Anal. Atom. Spectrom.*, 15(3):297–300, 2000.
- [64] J C Eijkel, H Stoeri, and A Manz. A dc microplasma on a chip employed as an optical emission detector for gas chromatography. *Anal. Chem.*, 72(11):2547–2552, 2000.
- [65] H J Kim, Y A Woo, J S Kang, S S Anderson, and E H Piepmeier. Development of an atmospheric pressure glow discharge detector for capillary column gas chromatography. *Microchim. Acta*, 143(1-2):1–7, 2000.
- [66] F G Bessoth, O P Naji, J C T Eijkel, and A Manz. Towards an on-chip gas chromatograph: the development of a gas injector and a dc plasma emission detector. *J. Anal. At. Spectrom.*, 17(8):794–799, 2002.
- [67] D C Liang and M W Blades. Atmospheric-pressure capacitively coupled plasma spectral lamp and source for the direct analysis of conducting solid samples. *Spectrochim. Acta B*, 44(10):1049–1057, 1989.
- [68] M W Blades. Atmospheric-pressure, radio-frequency, capacitively coupled helium plasmas. *Spectrochim. Acta B*, 49(1):47–57, 1994.
- [69] S D Anghel, T Frentiu, E A Cordos, A Simon, and A Popescu. Atmospheric pressure capacitively coupled plasma source for the direct analysis of non-conductive solid samples. *J. Anal. At. Spectrom.*, 14(4):541–545, 1999.
- [70] S Y Lu, C W LeBlanc, and M W Blades. Analyte ionization in the furnace atomization plasma excitation spectrometry source - spatial and temporal observations. *J. Anal. At. Spectrom.*, 16(3):256–262, 2001.

- [71] A Bass, C Chevalier, and M W Blades. A capacitively coupled microplasma (cc mu p) formed in a channel in a quartz wafer. *J. Anal. At. Spectrom.*, 16(9):919–921, 2001.
- [72] H Yoshiki and Y Horiike. Capacitively coupled microplasma source on a chip at atmospheric pressure. *Jpn. J. Appl. Phys., Part 2*, 40(4A):L360–L362, 2001.
- [73] R E Sturgeon, V T Luong, S N Willie, and R K Marcus. Impact of bias voltage on furnace atomization plasma emission-spectrometry performance. *Spectrochim. Acta B*, 48(6-7):893–908, 1993.
- [74] V Pavski, C L Chakrabarti, and R E Sturgeon. Spatial imaging of the furnace atomization plasma emission-spectrometry source. *J. Anal. At. Spectrom.*, 9(12):1399–1409, 1994.
- [75] R E Sturgeon and R Guevremont. Analyte ionization in a furnace atomization plasma emission source. *J. Anal. Atom. Spectrom.*, 13(4):229–233, 1998.
- [76] F Sun and R E Sturgeon. Influence of plasma gas composition on analyte ionization in furnace atomization plasma emission spectrometry. *J. Anal. At. Spectrom.*, 14(6):901–912, 1999.
- [77] F Sun and R E Sturgeon. Furnace atomization plasma emission spectrometry with he/ar mixed gas plasmas. *Spectrochim. Acta B*, 54(14):2121–2141, 1999.
- [78] R Guevremont and R E Sturgeon. Atmospheric pressure helium rf plasma source for atomic and molecular mass spectrometry. *J. Anal. At. Spectrom.*, 15(1):37–42, 2000.
- [79] A M Bilgic, E Voges, U Engel, and J A C Broekaert. A low-power 2.45 ghz microwave induced helium plasma source at atmospheric pressure based on microstrip technology. *J. Anal. At. Spectrom.*, 15(6):579–580, 2000.
- [80] A M Bilgic, U Engel, E Voges, M Kuckelheim, and J A C Broekaert. A new low-power microwave plasma source using microstrip technology for atomic emission spectrometry. *Plasma Sources Sci. Technol.*, 9(1):1–4, 2000.
- [81] J Hopwood and F Iza. Ultrahigh frequency microplasmas from 1 pascal to 1 atmosphere. *J. Anal. At. Spectrom.*, 19(9):1145–1150, 2004.
- [82] Y Yin, J Messier, and J A Hopwood. Miniaturization of inductively coupled plasma sources. *IEEE T. Plasma Sci.*, 27(5):1516–1524, 1999.
- [83] J A Hopwood. Microfabricated inductively coupled plasma generator. *J. Microelectromech. Syst.*, 9(3):309–313, 2000.
- [84] F Iza and J Hopwood. Influence of operating frequency and coupling coefficient on the efficiency of microfabricated inductively coupled plasma sources. *Plasma Sources Sci. Technol.*, 11(3):229–235, 2002.

- 
- [85] T Cserfalvi, P Mezei, and P Apai. Emission studies on a glow-discharge in atmospheric pressure air using water as a cathode. *J. Phys. D: Appl. Phys.*, 26(12):2184–2188, 1994.
- [86] P Mezei, T Cserfalvi, and M Janossy. Pressure dependence of the atmospheric electrolyte cathode glow discharge spectrum. *J. Anal. At. Spectrom.*, 12(10):1203–1208, 1997.
- [87] P Mezei, T Cserfalvi, M Janossy, K Szocs, and H J Kim. Similarity laws for glow discharges with cathodes of metal and an electrolyte. *J. Phys. D: Appl. Phys.*, 31(20):2818–2825, 1998.
- [88] T Cserfalvi and P Mezei. Subnanogram sensitive multimetal detector with atmospheric electrolyte cathode glow discharge. *J. Anal. At. Spectrom.*, 18(6):596–602, 2003.
- [89] H J Kim, J H Lee, M Y Kim, T Cserfalvi, and P Mezei. Development of open-air type electrolyte-as-cathode glow discharge-atomic emission spectrometry for determination of trace metals in water. *Spectrochim. Acta B*, 55(7):823–831, 2000.
- [90] W C Davis and R K Marcus. An atmospheric pressure glow discharge optical emission source for the direct sampling of liquid media. *J. Anal. Atom. Spectrom.*, 16(9):931–937, 2001.
- [91] R K Marcus and W C Davis. An atmospheric pressure glow discharge optical emission source for the direct sampling of liquid media. *Anal. Chem.*, 73(13):2903–2910, 2001.
- [92] W C Davis and R K Marcus. Role of powering geometries and sheath gas composition on operation characteristics and the optical emission in the liquid sampling-atmospheric pressure glow discharge. *Spectrochim. Acta B*, 57(9):1473–1486, 2002.
- [93] M R Webb, F J Andrade, G Gamez, R McCrindle, and G M Hieftje. Spectroscopic and electrical studies of a solution-cathode glow discharge. *J. Anal. At. Spectrom.*, 20(11):1218–1225, 2005.
- [94] K Kunze, M Miclea, G Musa, J Franzke, C Vadla, and K Niemax. Diode laser-aided diagnostics of a low-pressure dielectric barrier discharge applied in element-selective detection of molecular species. *Spectrochim. Acta: Part B*, 57:137–146, 2002.
- [95] M Miclea, K Kunze, J Franzke, and K Niemax. Plasmas for lab-on-the-chip applications. *Spectrochim. Acta: Part B*, 57:1585–1592, 2002.
- [96] K Kunze, M Miclea, J Franzke, and K Niemax. The dielectric barrier discharge as a detector for gas chromatography. *Spectrochim. Acta: Part B*, 58:1435–1443, 2003.

- [97] Z Zhu, S Zhang, J Xue, and X Zhang. Application of atmospheric pressure dielectric barrier discharge plasma for the determination of se, sb and sn with atomic absorption spectrometry. *Spectrochim. Acta B*, 61(8):916–921, 2006.
- [98] J Franzke, K Kunze, M Miclea, and K Niemax. Microplasmas for analytical spectrometry. *J. Anal. Atom. Spectrom.*, 18(7):802–807, 2003.
- [99] C Penache, M Miclea, A Bräning-Demian, O Hohn, S Schössler, T Jahnke, K Niemax, and H Schmidt-Böking. Characterization of a high-pressure microdischarge using diode laser atomic absorption spectroscopy. *Plasma Sources Sci. Technol.*, 11(4):476–483, 2002.
- [100] R J Skelton, H-C K Chang, P B Farnsworth, K E Markides, and M L Lee. Radio-frequency plasma detector for sulfur selective capillary gas-chromatographic analysis of fossil-fuels. *Anal. Chem.*, 61(20):2292, 1989.
- [101] J A C Broekaert. The development of microplasmas for spectrochemical analysis. *Anal. Bioanal. Chem.*, 374(2):182–187, 2002.
- [102] V Karanassios. Microplasmas for chemical analysis: analytical tools or research toys? *Spectrochim. Acta B*, 59(7):909–928, 2004.
- [103] J A C Broekaert and V Siemens. Some trends in the development of microplasmas for spectrochemical analysis. *Anal. Bioanal. Chem.*, 380(2):185–189, 2004.
- [104] K H Becker, K H Schoenbach, and J G Eden. Microplasmas and applications. *J. Phys. D: Appl. Phys.*, 39(3):R55–R70, 2006.
- [105] J Reece Roth. *Industrial plasma engineering: Volume 1: Principles*. IOP Publishing Ltd., Philadelphia, 1995.
- [106] S Rauf and M J Kushner. Dynamics of a coplanar-electrode plasma display panel cell. : I. basic operation. *J Appl Phys*, 85(7):3460–3469, 1999.
- [107] K Kutasi, P Hartmann, and Z Donkó. Self-consistent modelling of helium discharges: investigation of the role of  $he_2^+$  ions. *J. Phys. D: Appl. Phys.*, 34(23):3368–3377, 2001.
- [108] R Deloche, P Monchicourt, M Cheret, and F Lambert. High-pressure helium afterglow at room temperature. *Phys. Rev. A*, 13(3):1140–1176, 1976.
- [109] J Stevefelt, J M Pouvesle, and A Bouchoule. Reaction kinetics of a high pressure helium fast discharge afterglow. *J. Chem. Phys.*, 76(8):4006–4015, 1982.
- [110] W A Rogers and M A Biondi. Studies of mechanism of electron-ion recombination.2. *Phys. Rev. A: Gen. Phys.*, 134(5A):A1215–A1224, 1964.
- [111] G J M Hagelaar, G M W Kroesen, U van Slooten, and H Schreuders. Modelling of the microdischarges in plasma addressed liquid crystal displays. *J. Appl. Phys.*, 88(5):2252–2262, 2000.

- 
- [112] R Brandenburg, V A Maierov, Y B Golubovskii, H E Wagner, J Behnke, and J F Behnke. Diffuse barrier discharges in nitrogen with small admixtures of oxygen: discharge mechanism and transition to the filamentary regime. *J. Phys. D: Appl. Phys.*, 38(13):2187–2197, 2005.
- [113] A Bogaerts, R Gijbels, and J Vlcek. Collisional-radiative model for an argon glow discharge. *J. Appl. Phys.*, 84(1):121–136, 1998.
- [114] J P Boeuf. presentation at *Master Class: Microplasmas*, Bad Honnef, Germany, 13-15 Oct., 2005.
- [115] J D P Passchier and W J Goedheer. A 2-dimensional fluid model for an argon rf discharge. *J. Appl. Phys.*, 74(6):3744–3751, 1993.
- [116] R K Marcus and J A C Broekaert (eds.). *Glow Discharge Plasmas in Analytical Spectroscopy*. John Wiley and Sons, Ltd.: Chichester, U.K., 2003.
- [117] N Jakubowski, A Bogaerts, and V Hoffmann. *Glow Discharges in Emission and Mass Spectrometry*. Blackwell, Sheffield, U.K., 2003. in *Atomic Spectroscopy in Elemental Analysis* ed. M Cullen.
- [118] F Massines (ed.). Special issue on atmospheric pressure non-thermal plasmas for processing and other applications. *J. Phys. D: Appl. Phys.*, 38(4):505–575, 2005.
- [119] C Tendero, C Tixier, P Tristant, J Desmaison, and Ph Leprince. Atmospheric pressure plasmas: A review. *Spectrochim. Acta Part B*, 61(1):2–30, 2006.
- [120] L R Layman and GM Hieftje. New, computer-controlled microwave discharge emission spectrometer employing microarc sample atomization for trace and micro elemental analysis. *Anal. Chem.*, 47(2):194–202, 1975.
- [121] M Miclea, K Kunze, U Heitmann, S Florek, J Franzke, and K Niemax. Diagnostics and application of the microhollow cathode discharge as an analytical plasma. *J. Phys. D: Appl. Phys.*, 38(11):1709–1715, 2005.
- [122] Z L Zhu, S C Zhang, Y Ly, and X R Zhang. Atomization of hydride with a low-temperature, atmospheric pressure dielectric barrier discharge and its application to arsenic speciation with atomic absorption spectrometry. *Anal. Chem.*, 78(3):865–872, 2006.
- [123] C A Hill and C L P Thomas. A pulsed corona discharge switchable high resolution ion mobility spectrometer-mass spectrometer. *Analyst*, 128(1):55–60, 2003.
- [124] P Mezei, T Cserfalvi, and M Janossy. The gas temperature in the cathode surface - dark space boundary layer of an electrolyte cathode atmospheric glow discharge (ELCAD). *J. Phys. D: Appl. Phys.*, 31(11):L41–L42, 1998.

- [125] P Mezei and T Cserfalvi. The investigation of an abnormal electrolyte cathode atmospheric glow discharge (ELCAD). *J. Phys. D: Appl. Phys.*, 39(12):2534–2539, 2006.
- [126] M A Mottaleb, Y A Woo, and H J Kim. Evaluation of open-air type electrolyte-as-cathode glow discharge-atomic emission spectrometry for determination of trace heavy metals in liquid samples. *Microchem. J.*, 69(3):219–230, 2001.
- [127] M A Mottaleb, J S Yang, and H J Kim. Electrolyte-as-cathode glow discharge (elcad)/glow discharge electrolysis at the gas-solution interface. *Appl. Spectrosc. Rev.*, 37(3):247–273, 2002.
- [128] J L Venzie and R K Marcus. Effects of easily ionizable elements on the liquid sampling-atmospheric pressure glow discharge. *Spectrochim. Acta Part B*, 61(6):715–721, 2006.
- [129] M R Webb, G C Y Chan, F J Andrade, and G Gamez G M Hieftje. Spectroscopic characterization of ion and electron populations in a solution-cathode glow discharge. *J. Anal. Atom. Spectrom.*, 21(5):525–530, 2006.
- [130] M R Webb, F J Andrade, and G M Hieftje. Use of electrolyte cathode glow discharge (elcad) for the analysis of complex mixtures. *J. Anal. Atom. Spectrom.*, 22(7):766–774, 2007.
- [131] M R Webb, F J Andrade, and G M Hieftje. Compact glow discharge for the elemental analysis of aqueous samples. *Anal. Chem.*, 79(20):7899–7905, 2007.
- [132] M R Webb, F J Andrade, and G M Hieftje. High-throughput elemental analysis of small aqueous samples by emission spectrometry with a compact, atmospheric-pressure solution-cathode glow discharge. *Anal. Chem.*, 79(20):7807–7812, 2007.
- [133] W C Davis, F X Jin, M A Dempster, J L Robichaud, and R K Marcus. Development of a new liquid chromatography method for the separation and speciation of organic and inorganic selenium compounds via particle beam-hollow cathode glow discharge-optical emission spectroscopy. *J. Anal. At. Spectrom.*, 17(2):99–103, 2002.
- [134] F X Jin and R K Marcus. Selenium compound analysis by particle beam/hollow cathode optical emission spectroscopy (PB/HC-OES): monitoring of carbon and hydrogen emission from organoselenium compounds. *J. Anal. At. Spectrom.*, 18(6):589–595, 2003.
- [135] F X Jin, K Lenghaus, J Hickman, and R K Marcus. Total protein determinations by particle beam/hollow cathode optical emission spectroscopy. *Anal. Chem.*, 75(18):4801–4810, 2003.
- [136] T M Brewer, J Castro, and R K Marcus. Particle beam sample introduction into glow discharge plasmas for speciation analysis. *Spectrochim. Acta Part B*, 61(2):134–149, 2006.

- 
- [137] T M Brewer and R K Marcus. Determination of "free" iron and iron bound in metalloproteins via liquid chromatography separation and inductively coupled plasma-optical emission spectroscopy (LC-ICP-OES) and particle beam/hollow cathode-optical emission spectroscopy (LC-PB/HC-OES) techniques. *J. Anal. At. Spectrom.*, 22(9):1067–1075, 2007.
- [138] T M Brewer and R K Marcus. Separation and determination of iron-containing proteins via liquid chromatography-particle beam/hollow cathode-optical emission spectroscopy. *Anal. Chem.*, 79(6):2402–2411, 2007.
- [139] W C Davis, J L Venzie, B Willis, R L Coffee, D P Arya, and R K Marcus. Particle beam glow discharge mass spectrometry: spectral characteristics of nucleobases. *Rapid Comm. Mass Spectrom.*, 17(15):1749–1758, 2003.
- [140] M R Webb, F J Andrade, and G M Hieftje. The annular glow discharge: a small-scale plasma for solution analysis. *J. Anal. At. Spectrom.*, 22(7):775–782, 2007.
- [141] W C Wetzel, F J Andrade, J A C Broekaert, and G M Hieftje. Development of a direct current He atmospheric-pressure glow discharge as an ionization source for elemental mass spectrometry via hydride generation. *J. Anal. At. Spectrom.*, 21(8):750–756, 2006.
- [142] F J Andrade, W C Wetzel, G C-Y Chan, M R Webb, G Gamez, S J Ray, and G M Hieftje. A new, versatile, direct-current helium atmospheric-pressure glow discharge. *J. Anal. At. Spectrom.*, 21(11):1175–1184, 2006.
- [143] F J Andrade, J T Shelley, W C Wetzel, M R Webb, G Gamez, S J Ray, and G M Hieftje. Atmospheric pressure chemical ionization source. 1. Ionization of compounds in the gas phase. *Anal. Chem.*, 80(8):2646–2653, 2008.
- [144] F J Andrade, J T Shelley, W C Wetzel, M R Webb, G Gamez, S J Ray, and G M Hieftje. Atmospheric pressure chemical ionization source. 2. Desorption-ionization for the direct analysis of solid compounds. *Anal. Chem.*, 80(8):2654–2663, 2008.
- [145] J T Shelley, S J Ray, and G M Hieftje. Laser ablation coupled to a flowing atmospheric pressure afterglow for ambient mass spectral imaging. *Anal. Chem.*, 80(1):8308–8313, 2008.
- [146] J T Shelley, J S Wiley, G C Y Chan, G D Schilling, S J Ray, and G M Hieftje. Characterization of direct-current atmospheric-pressure discharges useful for ambient desorption/ionization mass spectrometry. *J. Am. Soc. Mass Spectrom.*, 20(5):837–844, 2009.
- [147] G D Schilling, J T Shelley, J A C Broekaert, R P Sperline, M B Denon and C J Barinaga, D W Koppenaal, and G M Hieftje. Use of an ambient ionization flowing atmospheric-pressure afterglow source for elemental analysis through hydride generation. *J. Anal. At. Spectrom.*, 24(1):34–40, 2009.

- [148] T Farouk, B Farouk, D Staack, A Gutsol, and A Fridman. Simulation of dc atmospheric pressure argon micro glow-discharge. *Plasma Sources Sci. Technol.*, 15(4):676–688, 2006.
- [149] Q Wang, D J Economou, and V M Donnelly. Simulation of a direct current microplasma discharge in helium at atmospheric pressure. *J. Appl. Phys.*, 100(2):023301, 2006.
- [150] J Choi, F Iza, J K Lee, and C M Ryu. Electron and ion kinetics in a dc microplasma at atmospheric pressure. *IEEE T. Plasma Sci.*, 35(5):1274–1278, 2007.
- [151] T Martens, A Bogaerts, W Brok, and J van Dijk. Computer simulations of a dielectric barrier discharge used for analytical spectrometry. *Anal. Bioanal. Chem.*, 388(8):1583–1594, 2007.
- [152] T Martens, A Bogaerts, W J M Brok, and J J A M van der Mullen. Modeling study on the influence of the pressure on a dielectric barrier discharge microplasma. *J. Anal. Atom. Spectrom.*, 22:1033–1042, 2007.
- [153] J J Shi and M G Kong. Cathode fall characteristics in a dc atmospheric pressure glow discharge. *J. Appl. Phys.*, 94(9):5504–5513, 2003.
- [154] A Bogaerts and R Gijbels. Modeling of glow discharges: what can we learn from it? *Anal. Chem. A-pages*, 69:A719–A727, 1997.
- [155] A Bogaerts and R Gijbels. Comprehensive description of a grimm-type glow discharge source used for optical emission spectrometry: a mathematical simulation. *Spectrochim. Acta Part B*, 53(3):437–462, 1998.
- [156] A Bogaerts. Plasma diagnostics and numerical simulations: insight into the heart of analytical glow discharges. *J. Anal. At. Spectrom.*, 22(1):13–40, 2007.
- [157] T Martens, A Bogaerts, W J M Brok, and J v Dijk. The dominant role of impurities in the composition of high pressure noble gas plasmas. *Appl. Phys. Lett.*, 92:041504, 2008.
- [158] T J Sommerer and M J Kushner. Numerical investigation of the kinetics and chemistry of rf glow discharge plasmas sustained in He, N<sub>2</sub>, O<sub>2</sub>, He/N<sub>2</sub>/O<sub>2</sub>, He/CF<sub>4</sub>/O<sub>2</sub>, and SiH<sub>4</sub>/NH<sub>3</sub> using a monte carlo-fluid hybrid model. *J. Appl. Phys.*, 71(4):1654–1673, 1992.
- [159] A Bogaerts and R Gijbels. Hybrid modeling network for a helium-argon-copper hollow cathode discharge used for laser applications. *J. Appl. Phys.*, 92:6408–6422, 2002.
- [160] A Kossyi, A Yu Kostinsky, A A Matveyev, and V P Silakov. Kinetic scheme of the non-equilibrium discharge in nitrogen-oxygen mixtures. *Plasma Sources Sci. Technol.*, 1:207–220, 1992.

- 
- [161] D L Albritton. Ion-neutral reaction-rate constants measured in flow reactors through 1977. *At. Data Nucl. Data Tables*, 22(1):1–101, 1978.
- [162] M Mcfarland, D L Albritton, F C Fehsenfeld, E E Ferguson, and A L Schmeltekopf. Flow drift technique for ion mobility and ion-molecule reaction-rate constant measurement. 1. apparatus and mobility measurements. *J. Chem. Phys.*, 59(12):6610–6619, 1976.
- [163] L A Viehland and E A Mason. Transport properties of gaseous ions over a wide energy range.4. *At. Data Nucl. Data Tables*, 60(1):37–95, 1995.
- [164] I S Grigoriev, E Z Meilikhov, and A A Radzig. *Handbook of physical quantities*. CRC, Boca Raton, Fl., 1997.
- [165] W J M Brok, M D Bowden, J van Dijk, J J A M van der Mullen, and G M W Kroesen. Numerical description of discharge characteristics of the plasma needle. *J. Appl. Phys.*, 98:013302, 2005.
- [166] A Bogaerts and R Gijbels. The role of fast argon ions and atoms in the ionization of argon in a direct-current glow-discharge - a mathematical simulation. *J. Appl. Phys.*, 78(11):6427–6431, 1995.
- [167] A Bogaerts, R Gijbels, and W J Goedheer. Two-dimensional model of a direct current glow discharge: Description of the electrons, argon ions, and fast argon atoms. *Anal. Chem.*, 68(14):2296–2303, 1996.
- [168] G Francis and S Flügge. *Handbuch der Physik*, volume 22. Springer-Verlag, Berlin, 1956.
- [169] D B Graves and K F Jensen. A continuum model of dc and rf discharges. *IEEE Trans. Plasma Sci.*, 14(2):78–91, 1986.
- [170] T Farouk, B Farouk, D Staack, A Gutsol, and A Fridman. Modeling of direct current micro-plasma discharges in atmospheric pressure hydrogen. *Plasma Sources Sci. Technol.*, 16(3):619–634, 2007.
- [171] A Bogaerts and R Gijbels. Two-dimensional model of a direct current glow discharge: Description of the argon metastable atoms, spattered atoms, and ions. *Anal. Chem.*, 68(15):2676–2685, 1996.
- [172] J W Shon and M J Kushner. Excitation mechanisms and gain modeling of the high-pressure atomic Ar laser in He/Ar mixtures. *J. Appl. Phys.*, 75(4):1883–1890, 1994.
- [173] T Martens, A Bogaerts, W J M Brok, and J van Dijk. The influence of impurities on the performance of the dielectric barrier discharge. *Appl. Phys. Lett.*, 2010. in press.

- [174] D Petrovic, T Martens, J van Dijk, W J M Brok, and A Bogaerts. Fluid modelling of an atmospheric pressure dielectric barrier discharge in cylindrical geometry. *J. Phys. D: Appl. Phys.*, 42(20):205206, 2009.
- [175] C Anderson, M Hur, P Zhang, L Mangolini, and U Kortshagen. Two-dimensional space-time-resolved emission spectroscopy on atmospheric pressure glows in helium with impurities. *J. Appl. Phys.*, 96(4):1835–1839, 2004.
- [176] Y Wang and D Wang. Influence of impurities on the uniform atmospheric-pressure discharge in helium. *Phys. Plasmas*, 12:023503, 2005.
- [177] P Zhang and U Kortshagen. Two-dimensional numerical study of atmospheric pressure glows in helium with ipurities. *J. Phys. D: Appl. Phys.*, 39:153–163, 2006.
- [178] T Martens, W J M Brok, J van Dijk, and A Bogaerts. On the regime transitions during the formation of an atmospheric pressure dielectric barrier glow discharge. *J. Phys. D: Appl. Phys.*, 42:122002, 2009.
- [179] B Eliasson and U Kogelschatz. Nonequilibrium volume plasma chemical processing. *IEEE Trans. Plasma Sci.*, 19(6):1063–1077, 1991.
- [180] J van Dijk, K Peerenboom, M Jimenez, D Mihailova, and J van der Mullen. The plasma modelling toolkit plasimo. *J. Phys. D: Appl. Phys.*, 42:194012, 2009.
- [181] W J M Brok, J van Dijk, M D Bowden, J J A M van der Mullen, and G M W Kroesen. A model study of propagation of the first ionization wave during breakdown in a straight tube containing argon. *J. Phys. D: Appl. Phys.*, 36(16):1967–1979, 2003.
- [182] B H P Broks, J van Dijk, and J J A M van der Mullen. Parameter study of a pulsed capillary discharge waveguide. *J. Phys. D: Appl. Phys.*, 39:2377, 2006.
- [183] BOLSIG, Boltzmann solver for the siglo-series 1.0. CPA Toulouse & Kinema Software, 1996.
- [184] M G Kong and X T Deng. Electrically Efficient Production of a Diffuse Nonthermal Atmospheric Plasma. *IEEE T. Plasma Sci.*, 31(1):7–18, 2003.
- [185] H Luo, Z Liang, B Lv, X Wang, Z Guan, and L Wang. Observation of the transition from a townsend discharge to a glow discharge in helium at atmospheric pressure. *Appl. Phys. Lett.*, 91:221504, 2007.
- [186] L Dong, Y He, W Liu, R Gao, H Wang, and H Zhao. Hexagon and square patterned air discharges. *Appl. Phys. Lett.*, 90:031504, 2007.
- [187] I Brauer, C Punset, H-G Purwins, and J P Boeuf. Simulations of self-organized filaments in a dielectric barrier glow discharge plasma. *J. Appl. Phys.*, 85(11):7569–7572, 1999.

- 
- [188] X P Lu and M Laroussi. Temporal and spatial emission behaviour of homogeneous dielectric barrier discharge driven by unipolar sub-microsecond square pulses. *J. Phys. D: Appl. Phys.*, 39:1127–1131, 2006.
- [189] Yu S Akishev, A V Dem'yanov, V B Karal'nik, M V Pan'kin, and N I Trushkin. Pulsed regime of the diffusive mode of a barrier discharge in helium. *Plasma Phys. Rep.*, 27(2):164–171, 2001.
- [190] J J Shi, D W Liu, and M G Kong. Plasma stability control using dielectric barriers in radio-frequency atmospheric pressure glow discharges. *Appl. Phys. Lett.*, 89:081502, 2006.
- [191] J J Shi, D W Liu, and M G Kong. Effects of dielectric barriers in radio-frequency atmospheric glow discharges. *IEEE Trans. Plasma Sci.*, 35(2):137–142, 2007.
- [192] S Liu and M Neiger. Excitation of dielectric barrier discharges by unipolar submicrosecond square pulses. *J. Phys. D: Appl. Phys.*, 34:1632–1638, 2001.
- [193] X Lu and M Laroussi. Optimization of ultraviolet emission and chemical species generation from a pulsed dielectric barrier discharge at atmospheric pressure. *J. Appl. Phys.*, 98:023301, 2005.
- [194] J J Shi, X T Deng, R Hall, J D Punnett, and M G Kong. Three modes in a radio frequency atmospheric pressure glow discharge. *J. Appl. Phys.*, 94(10):6303–6310, 2003.
- [195] G E Georghiou, A P Papadakis, R Morrow, and A C Metaxas. Numerical modelling of atmospheric pressure gas discharges leading to plasma production. *J. Phys. D: Appl. Phys.*, 38:R303–R328, 2005.
- [196] Yu B Golubovskii, V A Maiorov, J Behnke, and J F Behnke. On the stability of a homogeneous barrier discharge in nitrogen relative to radial perturbations. *J. Phys. D: Appl. Phys.*, 36:975–981, 2003.